# Effect of Graphene Filler on the Mechanical, Electrical, and Thermal Properties of Polymer Composite

by

Mohamed Ali CHARFI

MANUSCRIPT-BASEDTHESIS PRESENTED TO ÉCOLE DE TECHNOLOGIE SUPÉRIEURE IN PARTIAL FULFILLMENT FOR A MASTER'S DEGREE WITH THESIS IN MECHANICAL ENGINEERING M. A. Sc.

MONTREAL, DECEMBER 7, 2020

ECOLE DE TECHNOLOGIE SUPÉRIEURE
UNIVERSITÉ DU QUÉBEC

**BOARD OF EXAMINERS**

THIS THESIS HAS BEEN EVALUATED

BY THE FOLLOWING BOARD OF EXAMINERS

Mr. Jean François Chatelain, Thesis Supervisor
Departement of Mechanical Engineering at École de technologie supérieure

Mr. Gilbert Lebrun, Thesis Co-supervisor
Department of Mechanical Engineering at Université du québec à trois-rivières

Mr. Raynaud Guilbeault , President of the Board of Examiners
Departement of Mechanical Engineering at École de technologie supérieure

Mrs. Martine Dubé , Member of the jury
Departement of Mechanical Engineering at École de technologie supérieure

Mrs. Claudiane Ouellet-Plamondon , Member of the jury
Departement of Construction Engineering at École de technologie supérieure

THIS THESIS WAS PRENSENTED AND DEFENDED

IN THE PRESENCE OF A BOARD OF EXAMINERS AND PUBLIC

ON NOVEMBER 27, 2020

AT ÉCOLE DE TECHNOLOGIE SUPÉRIEURE

# ACKNOWLEDGMENT

# Effet de la charge de graphène sur les propriétés mécaniques, électriques et thermiques du composite polymère

Mohamed Ali CHARFI

## RÉSUMÉ

Les polymères renforcés de fibres de carbone (CFRP) forment des composants essentiels dans de nombreux types de véhicules tels que les avions, les engins spatiaux, les sous-marins et les véhicules de transport. Ils atteignent des propriétés mécaniques comparables aux métaux ordinaires, mais avec une densité plus faible. Cela permet aux véhicules de devenir plus légers, ce qui réduit la consommation de carburant, la pollution de l'air et les coûts associés. Les chercheurs ont démontré que la défaillance de la pièce composite est souvent due à un défaut à d'interface fibre / matrice. La qualité de collage de la matrice est un facteur critique qui dicte les propriétés structurelles globales. Ainsi, l'amélioration de la matrice d'un composite polymère présente un vif intérêt pour bonifier les propriétés mécaniques des matériaux CFRP.

Les matériaux CFRP sont des composites à base de fibre de carbone. La conductivité électrique et thermique de la fibre de carbone sont extrêmement élevées. Cependant, les matrices polymère sont des matériaux isolants qui réduisent considérablement les conductivités électriques et thermiques de l'ensemble du composite CFRP. La conductivité thermique est un facteur clé dans l'usinabilité des CFRP. Une conductivité plus élevée dissipe la chaleur de la pièce usinée et de l'outil de coupe. Cela réduit la température de coupe et prolonge la durée de vie de l'outil de coupe.

Dans cette étude, nous visons à améliorer les propriétés mécaniques du CFRP et les conductivités thermique et électrique de la matrice époxy par l'incorporation de particules de graphène dans la matrice. Dans la première partie de ce travail, les propriétés électriques des composites avec cinq concentrations de graphène différentes (0, 3, 5, 7 et 10 wt. %) ont été évaluées par spectroscopie diélectrique à large bande (BDS). Les résultats démontrent une amélioration d'un facteur quatre entre $10^{-15}$ a $10^{-14}$ à 10 wt. % de charge de graphène et le seuil de percolation a été atteint avec seulement 7 wt. %. La conductivité thermique a été évaluée qualitativement par la calorimétrie différentielle à balayage (DSC). Les échantillons avec 10 wt. % de graphène ont montré une réduction d'environ 16% de leur capacité thermique spécifique qui peut se traduire par une amélioration de la conductivité thermique.

En termes de propriétés mécaniques, une méthode de fabrication appropriée du CFRP a été développée. Cette approche conduit à une fraction volumique de fibre cohérente avec un niveau de vide minimum et une bonne dispersion de graphène. Avec ce procédé, l'impact du graphène sur les propriétés mécaniques du CFRP peut être évalué avec précision. Sept concentrations de graphène allant de 0 wt. % à 3 wt. % ont été testés. L'échantillons avec 0,25 wt. % ont montré la meilleure résistance à la flexion et au cisaillement inter laminaire avec une amélioration de 5%.

VIII

# Effect of Graphene Filler on the Mechanical, Electrical, and Thermal Properties of Polymer Composite

Mohamed Ali CHARFI

## ABSTRACT

Carbon fiber reinforced polymer materials (CFRP) form vital components in many types of vehicles such as airplanes, spacecraft, submarines, and transport vehicles. They achieve comparable mechanical properties to ordinary metals, but with a lower density. This allows vehicles to become lighter which reduces fuel consumption, air pollution, and related costs. Researchers have demonstrated that the failure of the composite part is often induced by a defect at the fiber/matrix interface. The matrix bond quality is a critical factor that dictates the overall structural properties. Thus, enhancing the matrix of a polymer composite presents an avenue to improve the mechanical properties of CFRP materials.

CFRP materials are carbon fiber-based composites. The electrical and thermal conductivities of carbon fiber are extremely high. However, polymetric matrices are insulative materials that dramatically reduce the electrical and thermal conductivities of the overall CFRP composite. The thermal conductivity is a pivotal factor in the machinability of CFRPs. Higher conductivity dissipates the heat from the workpiece/cutting tool. This reduces the cutting temperature and extends the service life of the cutting tool.

In this study, we aim to improve the CFRP mechanical properties and the thermal/electrical conductivities of the epoxy matrix through the incorporation of graphene particles into the matrix. In the first part of this work, the electrical properties of composites with five different graphene concentrations (0, 3, 5, 7, and 10 wt. %) were evaluated through the broadband dielectric spectroscopy (BDS). The results demonstrate a four-fold enhancement at 10 wt. % of graphene filler and the percolation threshold was achieved with only 7 wt. %. The thermal conductivity was assessed qualitatively through the differential scanning calorimetry (DSC). Samples with 10 wt. % of graphene showed around 16 % reduction in their specific heat capacity which can be translated into an enhancement of the thermal conductivity.

In terms of mechanical properties, a suitable manufacturing method of the CFRP was developed. This approach leads to a consistent fiber volume fraction with a minimum void level and a good graphene dispersion. With this process, the impact of the graphene on the mechanical properties of the CFRP can be accurately assessed. Seven graphene concentrations ranging from 0 wt. % to 3 wt. % were tested. Samples with 0.25 wt. % showed the best flexural strength and interlaminar shear strength with an improvement of 5%.

**Keywords:** CFRP, Graphene, Thermal and Electrical conductivities, Mechanical properties

**TABLE OF CONTENTS**

# LIST OF TABLES

# LIST OF FIGURES

# LIST OF ABREVIATIONS

| | |
|---|---|
| 3RM | Three-roll milling |
| HSM | High shear mixing |
| CFRP | Carbon fiber reinforced polymer |
| VARTM | Vacuum assisted resin transfer molding |
| GnP | Graphene nano-platelet |
| GO | Graphite oxide |
| rGO | Reduced graphite oxide |
| GFL | Graphene few layer |
| SLG | Single layer graphene |
| CNT | Carbon nano tube |
| CVD | Chemical vapor deposition |
| PMMA | Polymethyl methacrylate |
| PVP | Polyvinylpyrrolidone |
| THF | Tetrahydrofuran |
| PCD | Polycrystalline Diamond |
| DSC | Differential Scanning Calorimetry |
| BDS | Broadband dielectric spectroscopy |
| ILSS | Interlaminar shear strength |
| Wt | Weight |
| DC | Direct current |
| AC | Alternative current |

# LIST OF SYMBOLS AND MEASURMENT UNITS

| | |
|---|---|
| $\mu$ | Dipole moment [C.m] |
| Q | Magnitude of the positive or negative charges [C] |
| r | Distance between negative and positive center [m] |
| M | Total of dipole moment [C.m] |
| P | Polarization [C/m²] |
| E | Electric field [V/m] |
| V | Voltage [V] |
| $\tau$ | Relaxation time [S] |
| $\varepsilon$ | Dielectric constant [F/m] |
| $\sigma$ | Electrical conductivity [S/cm] |
| $\varepsilon_0$ | Free space permittivity [F/m] |
| $\varphi c$ | Percolation threshold |
| $\varphi$ | Filler volume fraction |
| $\sigma f$ | Filler conductivity [S/cm] |
| $t$ | Scaling exponent |
| $\varphi_{tunnel}$ | Tunneling resistivity [Ω·m] |
| $\lambda$ | Barrier height of the insulator [eV] |
| Q | Heat flow [W/m²] |
| K | Thermal conductivity [W.m$^{-1}$. K$^{-1}$] |
| $\nabla T$ | Temperature gradient |
| Ke | Electron vibration |
| Kp | Phonon vibration |

| | |
|---|---|
| Wh | Hardener weight [g] |
| Wg | Graphene weight [g] |
| Wep | Epoxy weight [g] |
| Wt | Total weight [g] |
| Tc | Temperature of crystallization [°K] |
| Tm | Temperature of melting [°K] |
| Tg | Glass transition temperature [°K] |
| Hc | Heat of crystallization [mW] |
| Hm | Heat of melting [mW] |
| Cp | Specific heat capacity [J/kg.K] |
| Ef | Flexural chord modulus of elasticity [GPa] |
| $\sigma_F$ | Flexural stress [MPa] |
| $\varepsilon$ | Strain [mm/mm] |
| Mf | Surface density of dry reinforcement [g/m²] |
| N | Number of plies |
| $\varphi$ | Fiber density [g/m3] |
| $h$ | Laminate thickness [m] |

# INTRODUCTION

Composite materials with organic matrices, such as carbon fiber-reinforced polymer (CFRP) and glass fiber reinforced polymer (GFRP), are increasingly being employed in multiple industrial sectors, such as aeronautic, marine, submarine, wind energy, and road vehicles. In general, the fiber-reinforced polymer (FRP) materials are distinguished by their combination of high mechanical properties, chemical stability, and low density which cannot be achieved with ordinary metals. As an example of an industry with developing demand, lightweight vehicles, enabled by FRPs, are becoming increasingly significant due to efforts to optimize fuel consumption and reduce air pollution.

In their most simple form, composite materials are comprised of two components: the fibers and the matrix. The fibers bear the mechanical loads, while the matrix holds the fibers together to form a cohesive shape and protects them from corrosion. However, the interface fiber/matrix is a weak spot in composite materials. Typically, the breakage of the composite part is caused by a defect in the vicinity of the interface. To overcome this issue, researchers have sought to improve the matrix bonding properties to strengthen FRP materials.

The high mechanical strength of composite materials makes them inherently abrasive which results in excessive tool wear during machining and high cutting temperatures. Machining at a temperature higher than the glass transition temperature of the polymeric matrix induces a poor quality of the machined surface and often leads to premature failure. Moreover, polymer matrices are insulative materials that limit the electrical and thermal conductivities of the material. The low thermal conductivity of the CFRPs prevents the dissipation of the heat generated during machining. Therefore, enhancing the heat dissipation would reduce the cutting temperature which should reduce the defects induced by machining and increase the lifetime of the cutting tools.

**Project overview**

The presented study is a part of a larger scientific study. The main goal of the entire project is to enhance the machinability of the carbon fiber-reinforced polymer. As above mentioned, adding graphene particles in the matrix of the CFRP should enhance the thermal conductivity of the composite. Therefore, increasing the heat dissipation and reducing the accumulative cutting temperature which in turn should extend the tool life and might even improve the surface finish.

**Objectives of this study**

- Enhancing the machinability of the CFRP is an important factor. However, adding foreign material into the CFRP might affect its mechanical properties. Hence, it is crucial to start by assessing the properties of the modified CFRP and to find the graphene load that leads to the best mechanical/ thermal properties. In this context, the objectives of this study are:
- Devolop a reliable manufacturing method of the modified CFRP that induces:
    - A Constant fiber volume fraction (Vf)
    - A uniform dispersion of the graphene particles
    - A low porosity level
    - A minimum fluctuation of the fiber orientation
- Assess the mechanical properties of the modified CFRP through a short beam shear test and flexural test
- Investigate the thermal/ electrical properties of the modified epoxy

**Thesis organization**

This thesis contains three separate chapters. The first chapter, titled literature review, presents various manufacturing and mixing approaches and the fundamental mechanisms behind the thermal and electrical conductivity within the composite matrix. In the second chapter, the

samples' preparation is discussed with the results of broadband spectroscopy (BDS) and differential scanning calorimetry (DSC) for the electrical and the thermal conductivity, respectively. The third chapter is a journal article. In this chapter, an innovative manufacturing method is described for the CFRP. This method yields a consistent fiber volume fraction with a minimum void percentage. Additionally, the interlaminar shear strength (ILSS) and the flexural strength of seven different graphene concentrations have been documented.

# CHAPTER 1

# LITERATURE REVIEW

## 1.1 Introduction

Over the past decades, the demand for composite materials has increased remarkably, with an annual growth rate of approximately 8% (2008-2013) (Elmar, Thomas, & Michael, 2014). Figure 1.1 shows an estimation of the CFRP global demand, forecasted to reach 89000 tons by 2020. This high demand can be explained by the outstanding mechanical properties of the CFRP in conjunction with its lightweight. The combination of these characteristics cannot be achieved with ordinary materials, such as steel and its derivatives. A major contributing factor to the rising demand is the aeronautic industry. Boeing and Airbus utilize CFRPs for more than 50% of their modern aircrafts' structure (Breuer, 2016).
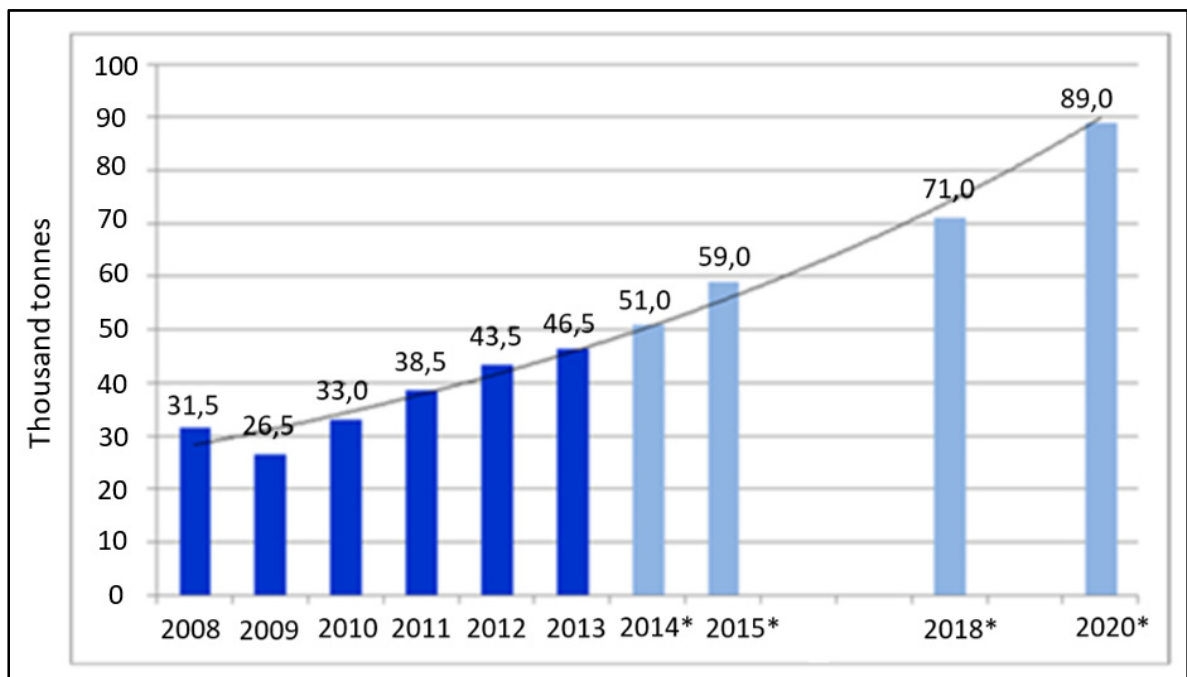
Figure 1.1 Global demand of CFRP
Adapted from Holmes (2014)

## 1.2        Composite Materials

By definition, composite material is a material that is composed of at least two sub-materials. This usually results in better mechanical properties than of those ordinary metals such as metallic alloys. For CFRPs the ratio of strength to weight is five-times higher than those of steels. Similarly, the stiffness to weight ratio can be 8 times higher than of those ordinary metals (Budynas & Nisbett, 2011). Figure 1.2 presents the stiffness versus the density of each material.
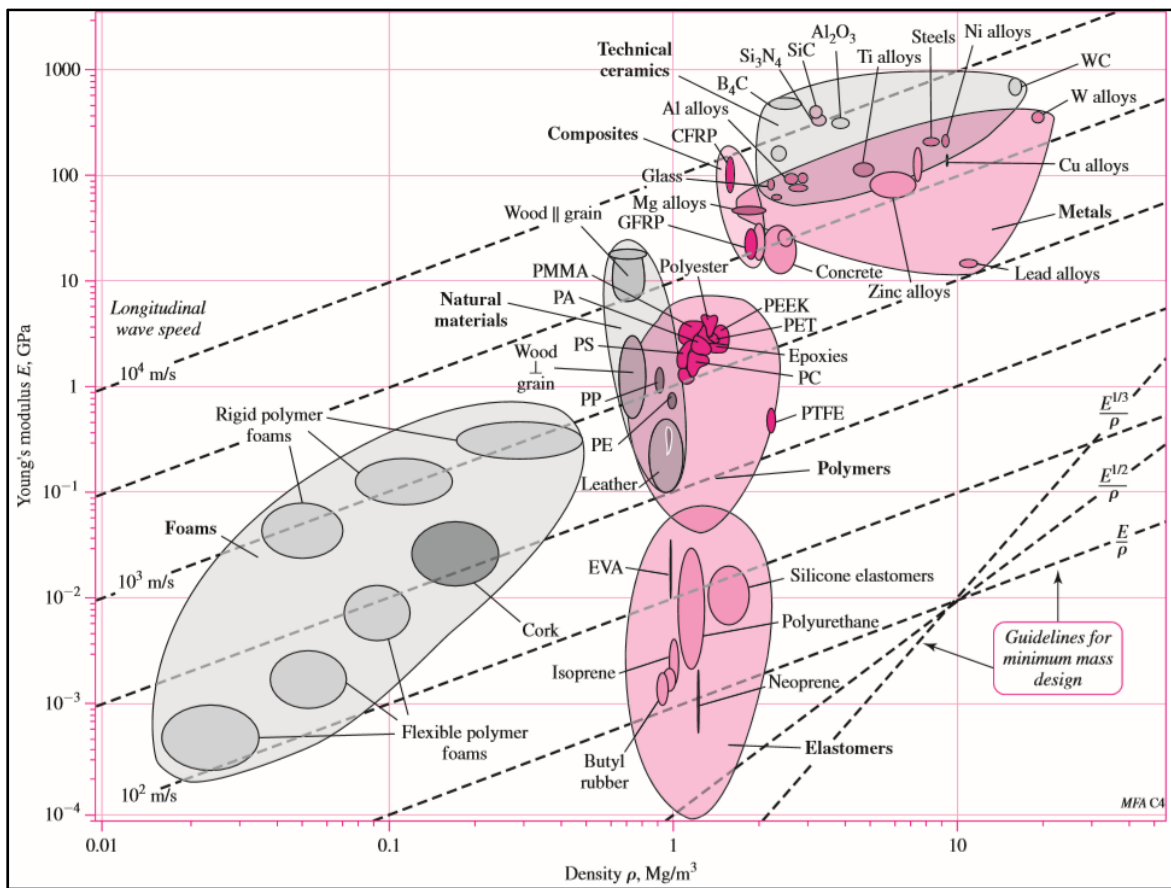


Figure 1.2 Stiffness versus density
Taken from Budynas & Nisbett (2011, p. 64)

Typically, composite materials are formed by two phases: matrix and reinforcement. The matrix purpose is to protect the reinforcement from corrosion, to maintain the ultimate part shape, and to transmit the load (Teti, 2002). The purpose of the reinforcement is to bear the

mechanical load (Budynas & Nisbett, 2011 ; Campbell, 2010a). Reinforcement materials can be classified into two categories: shape and composition. Figure 1.3 shows four groups of composites categorized by the fiber shape criterion.
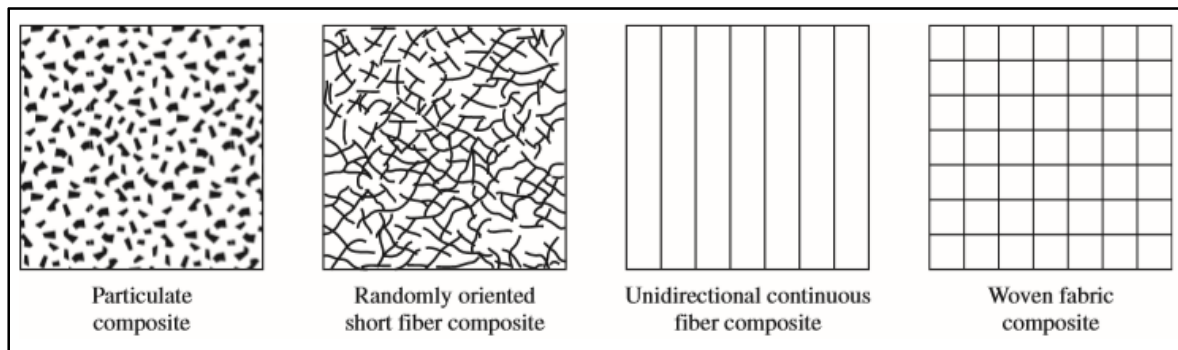


Figure 1.3 Different type of shape/size of fiber
Taken from Budynas & Nisbett (2011, p. 60)

The reinforcement material can be either fiber or particulate. Particulates have approximately the same dimension in all directions. They may come in spherical or platelet shape. The volume fraction of a particulate reinforced composite is usually limited to a maximum of 50%. This is because of the manufacturing difficulties and brittleness. Particulate reinforced composites are typically isotropic, meaning they possess almost the same mechanical properties in different directions. However, they tend to have lower strength and toughness than fiber reinforced composites. On the other hand, fiber have a greater length than its diameter. This ratio is called the aspect ratio which defines the fiber quality. Fibers with a higher aspect ratio possesses better quality but are typically more expensive. Composites containing long continuous fibers generally have greater flexibility and can be easily processed in different forms. Fiber materials can be aramid, glass, or carbon, which may be continuous or discontinuous (Campbell, 2010).

Composites can be also categorized by their matrix type. The matrix is the continuous component of the composite. The primary types of matrix are metal, ceramic, and polymer matrices. Metal and ceramic matrices usually require high temperature and pressure processing. These matrices have greater thermal stability, but substantially higher cost. Polymer matrices can be further subdivided into thermoset polymers and thermoplastic

polymers. The difference between these forms is the curing process. Thermoset polymers often cure by an exothermic reaction between two liquid polymer precursors. Thermoplastic polymers are hardened through solidification from a homogenous liquid phase. This solidification is reversible, allowing thermoplastics to be melted and recast. However, the curing of thermoset polymers is not reversible. Each of these polymer matrices has a different set of suitable processing methods which are presented in Figure 1.4.
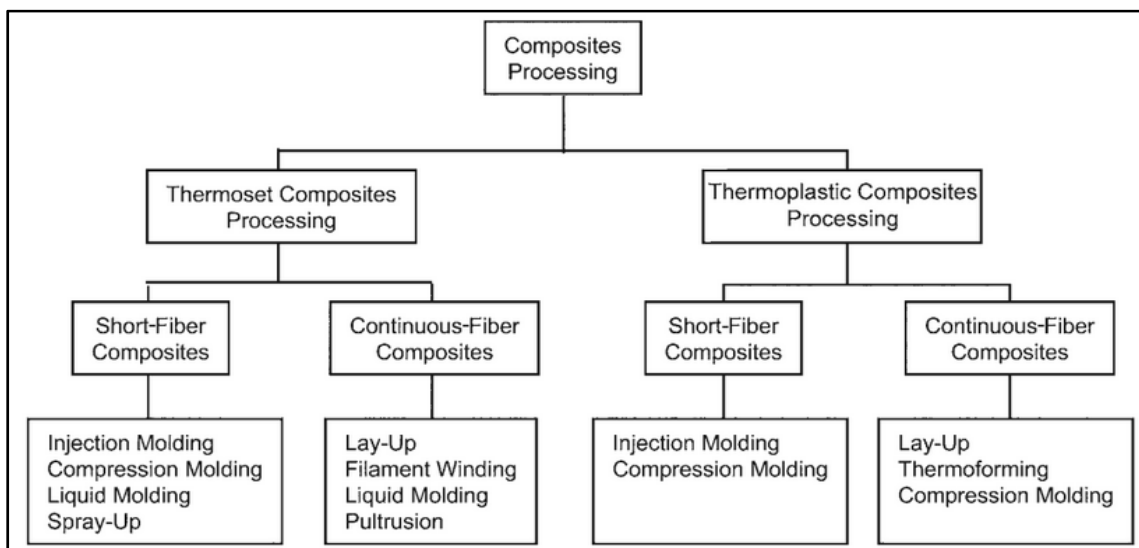
Figure 1.4 Major polymer matrix composite fabrication processes
Drawn from Campbell (2010a, p. 3)

## 1.3 Manufacturing Methods

There are many manufacturing methods for FRP materials. The selection of a suitable method greatly depends on the matrix type, the fiber length, and the field of application. In this section, three fundamental approaches are presented: wet lay-up, autoclave curing, and vacuum-assisted resin transfer molding.

### 1.3.1 Wet lay-up

The wet lay-up process is generally used for the production of small numbers of units. This process is the lowest cost (Campbell, 2012). It is suitable for large, thick objects, such as in

marine manufacturing, as well as small and complex parts. The process is schematically presented in Figure 1.5 and it can be described as follows:

- The first step is to prepare the mold. This consists of two sub-steps. Water cleaning of the mold to guarantee a good surface finish and coating the mold with a release agent to assure a smooth demolding process.
- Placing the first reinforcement ply on top of the mold with respecting the required orientation. Then, pouring onto the dry reinforcement the quantity of resin needed to fully impregnate it.
- This step is repeated until the desired part thickness is reached.
- Between the addition of each dry ply, hand rollers are used to eliminate trapped air bubbles, to remove the excess resin, and to compact the plies.
- Finally, the polymer is cured at room temperature or at higher temperature.

Typically, a vacuum bag is not necessary for this method. However, it has been shown that the vacuum can improve composite quality. In this method, the weight and fiber volume fraction are not easily controlled. The precision is limited by the hand labor used to remove air and compact the reinforcement.
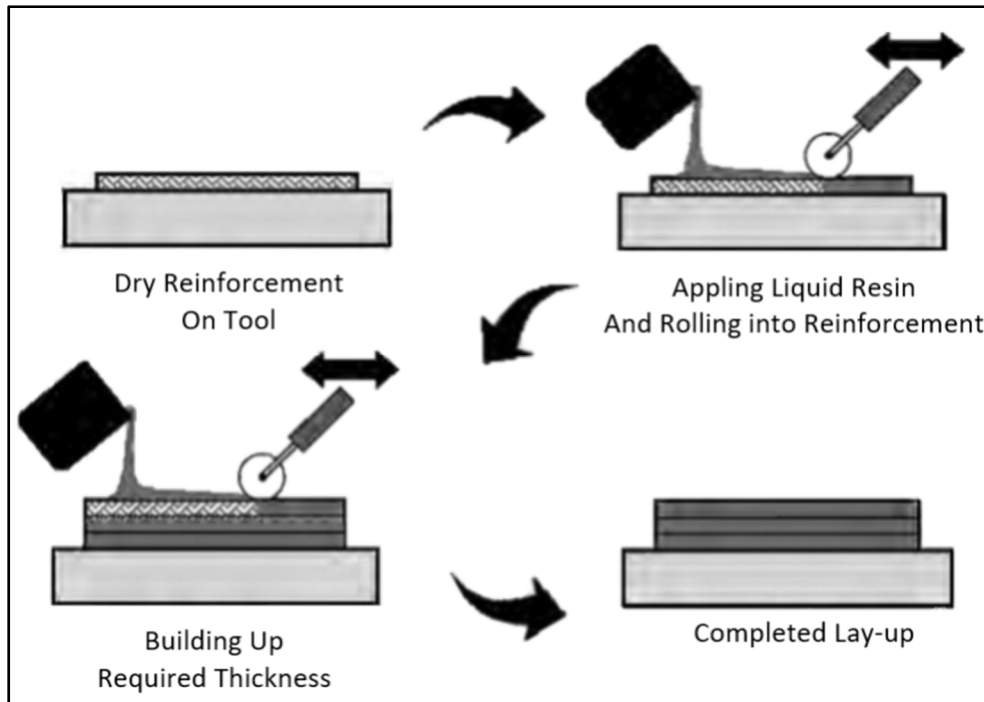
Figure 1.5 Typical wet lay-up operation
Adapted from Campbell  (2010a, p. 120)

## 1.3.2    Autoclave Curing

Autoclave curing assures homogeneous dispersion of both the fiber and matrix and a higher fiber volume fraction, compared to other methods. Composites produced through autoclave processing possess the best mechanical properties (Campbell, 2012). However, the cost is relatively high because it requires a great amount of hand labor and autoclave processing. In this method, layers of reinforcement impregnated with polymer are placed on top of the mold in a way that respects the required fiber orientation and thickness. Next, a vacuum pressure is applied to extract the air and to compact the layers. To cure the laminates, the assembly is placed inside an autoclave under a specific pressure and temperature (Figure 1.6).
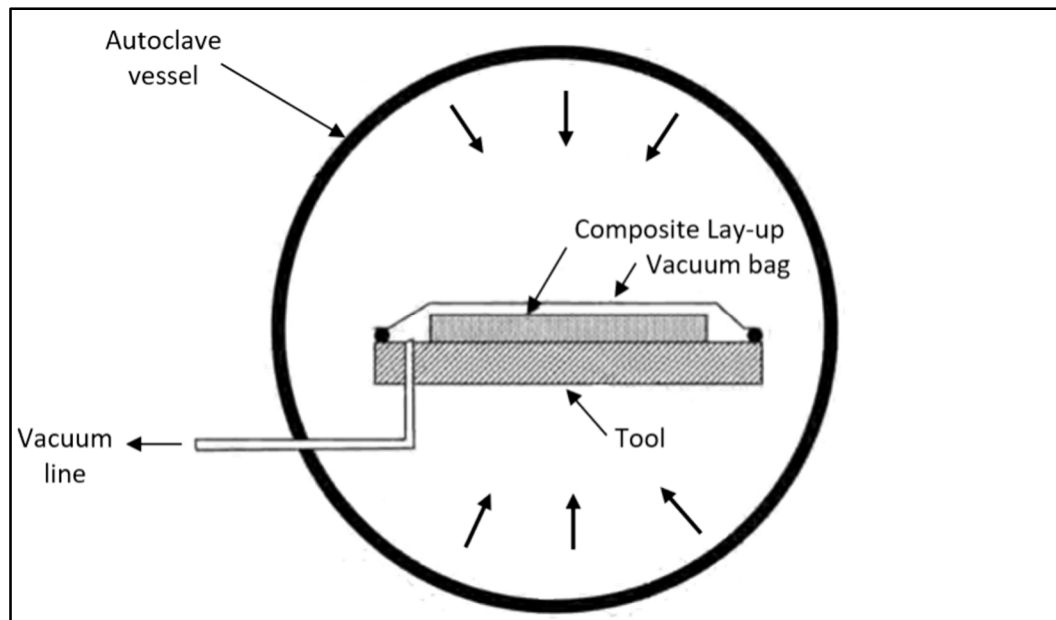
Figure 1.6 Principal of autoclave curing
Adapted from Campbell (2012, p. 433)

### 1.3.3 Resin Infusion Molding (RI)

Resin infusion molding is a method that requires: a one-sided mold, vacuum bag, porous distribution media, and vacuum pipes. As shown in Figure 1.7, the fiber layers are placed on top of the mold. Then, a porous release material is placed on the fiber plies to assure a smooth demolding. Finally, a flow medium is placed underneath the vacuum bag which is connected to two vacuum pipes. While the first pipe presents the inlet of resin, the second presents the outlet which is linked to a catch can (resin trap). Subsequently, applying the vacuum pressure will force the resin to flow from the inlet to the outlet, impregnating the fibers.
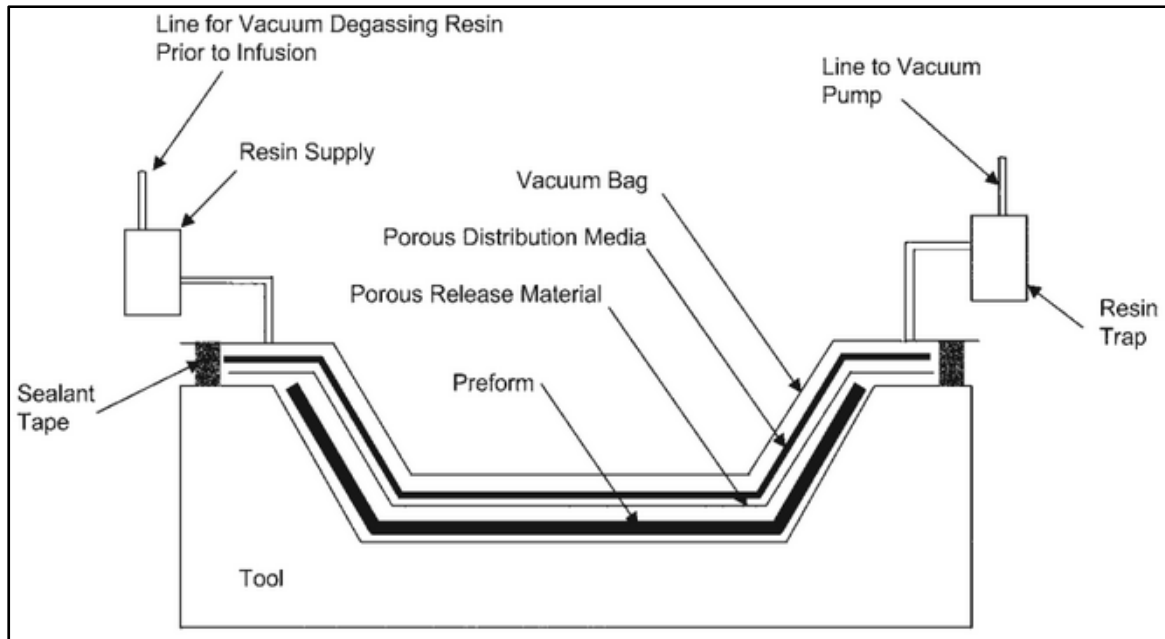
Figure 1.7 Resin infusion molding
Adapted from Campbell (2012, p. 435)

## 1.4      Graphene Filler

Graphene has gained enormous attention over the last decade (Prasai, Tuberquia, Harl, Jennings, & Bolotin, 2012 ; Zhao, Hayner, Kung, & Kung, 2011). The modern study of graphene started in 2004 with the first report of 'scotch tape' graphene exfoliation (Randviir, Brownson, & Banks, 2014), which presented an easy method for synthesizing it. Modeling predicts that graphene possesses the strongest mechanical properties of any known material (Teti, 2002). The young's modulus and the ultimate strength of a single layer equal to approximately 1 TPa and 130 GPa, respectively (Campbell, 2010a). Moreover, graphene excels in its high thermal conductivity of about 5000 W/(m.K) and excellent electrical conductivity of almost 6000 S/cm. The material has been employed in a large number of academic and industrial trials in various fields, such as: corrosion prevention (Prasai et al., 2012), longer-lasting batteries (Zhao et al., 2011), efficient solar cells (Hui Wang, Sun, Tao, Stacchiola, & Hu, 2013), display panels (Radivojevic et al., 2012), circuit boards (Hyun, Park, & Chin, 2013), and detection of medical diseases (Bonanni & Pumera, 2011).

Graphene can be added to metals, polymers, and ceramics to create composite materials with improved properties in the form of higher conductivity, thermal stability and tolerance to pressure (Lohar, 2017). Graphene can be naturally found in the graphite. Graphite is composed of multiple atomic layers of graphene bound together by van der Waals force (Figure 1.8). These stacked layers form a hexagonal honeycomb crystal structure. Each atomic layer consists of $sp^2$ bonded carbon atoms and the thickness of graphene particles can range from monatomic (0.345 nm) to 100 nm (Al Imran, 2016). Other carbon derivatives exist based on the graphene layer structure in shapes such as carbon nanotubes and buckminsterfullerenes (buckyballs).



(a) Honeycomb structure

(b) Graphite

(c) Carbon nanotube

(d) Buckyballs
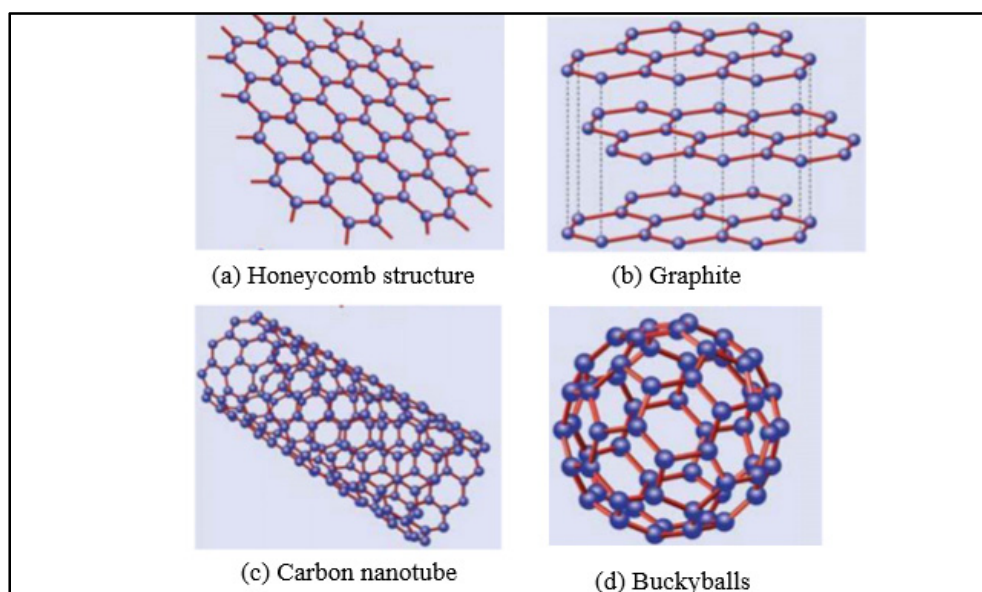
Figure 1.8 Graphene structure
Adapted from Sengupta, Bhattacharya, Bandyopadhyay, & Bhowmick (2011)

The fabrication methods of graphene were thoroughly described by X.-Y. Wang, Narita, & Müllen (2018) and the quality was assessed for each method. Two broad terms have been introduced to describe the manufacturing techniques: top-down and bottom-up. Figure 1.9 illustrates some of the different synthesis methods. Top-down consists of dimensional reduction of the graphite structure from 3D to 2D. Conversely, bottom-up involves increasing the particle dimension from 0D to 1D and from 1D to 2D, etc. The quality of the resulting graphene is measured by evaluating the integrity of graphene's $sp^2$ honeycomb network. This

can be done through microscopy, such as transmission electron microscopy, or crystallographic means, such as electron diffraction and Raman spectroscopy. For instance, the ratio ID/IG of Raman spectroscopy presents a good indicator, with a ratio of less than 0.2 indicating high-quality. X-ray photoelectron spectroscopy reveals that the oxygen content is linked to the overall graphene quality. The ratio of carbon to oxygen should be greater than 20 to ensure a high-quality structure.
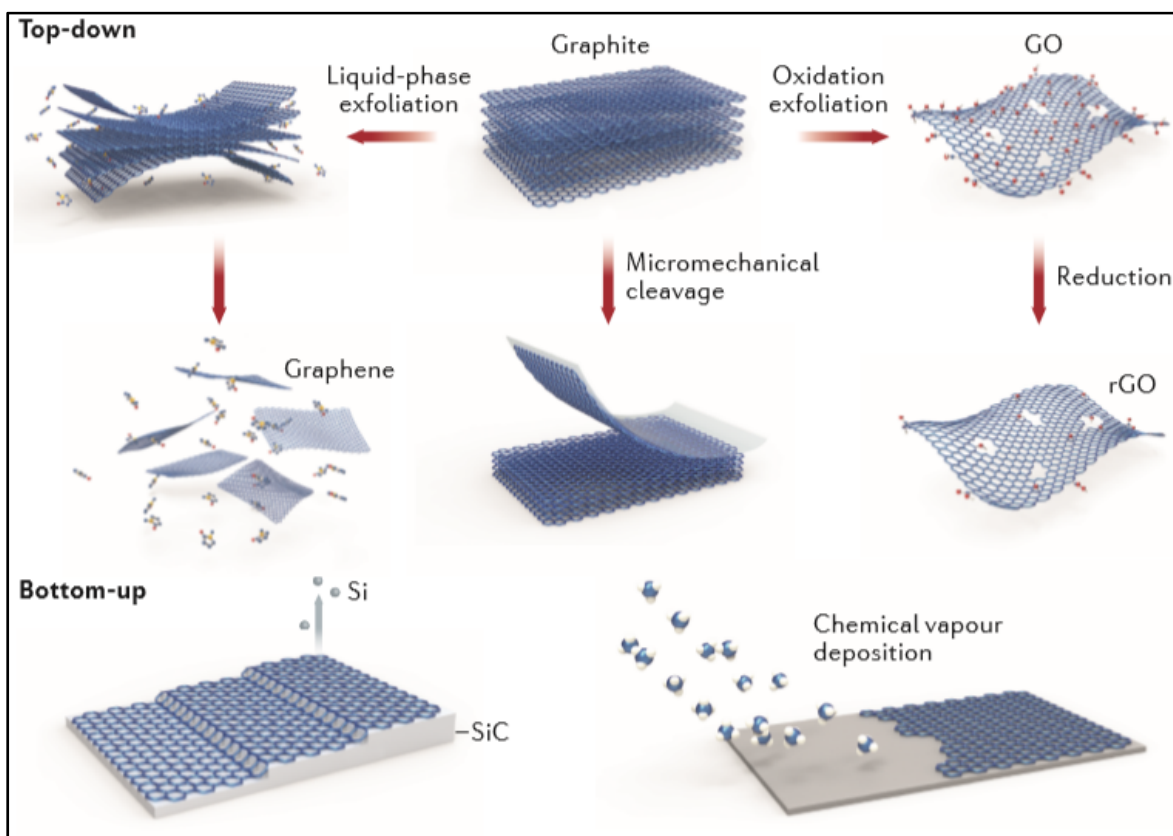


Figure 1.9 Major manufacturing methods of graphene
Taken from X.-Y. Wang et al. (2018, p. 3)

## 1.4.1 Bottom-up Synthesis

Bottom-up graphene synthesis refers to multiple techniques, such as chemical vapor deposition (CVD) (Di et al., 2008 ; X. Li et al., 2009), epitaxial growth on SiC (Sutter, Flege, & Sutter, 2008), arc discharge (N. Li et al., 2010), unzipping of carbon nanotubes (Kosynkin et al.,

2009), chemical conversion (X. Yang et al., 2008), and self- assembly of surfactants (W. Zhang et al., 2009). CVD and epitaxial growth are some of the most promising techniques because they induce large-size graphene layers with few crystallographic defects (S. Hamidinejad, 2019). Chemical vapor deposition (CVD) is comprised of two major steps:

- Growing of graphene on nickel or copper substrate
- Transferring the grown graphene onto a thin plate for storage

The synthesis process of graphene on Ni starts by annealing nickel film in an argon/hydrogen (Ar/H2) atmosphere at approximately 1000°C to reduce the surface and increase the grain size. Then, this film is exposed to a syngas mixture of hydrogen and methane (H2/CH4). The hydrocarbon molecules are decomposed on the surface of the nickel and penetrate the film (Figure 1.10). The carbon impregnated film is then cooled down in argon gas, which forces the carbon atoms to emerge and precipitate into a graphene layer (Yu et al., 2008 ; Y. Zhang, Zhang, & Zhou, 2013).
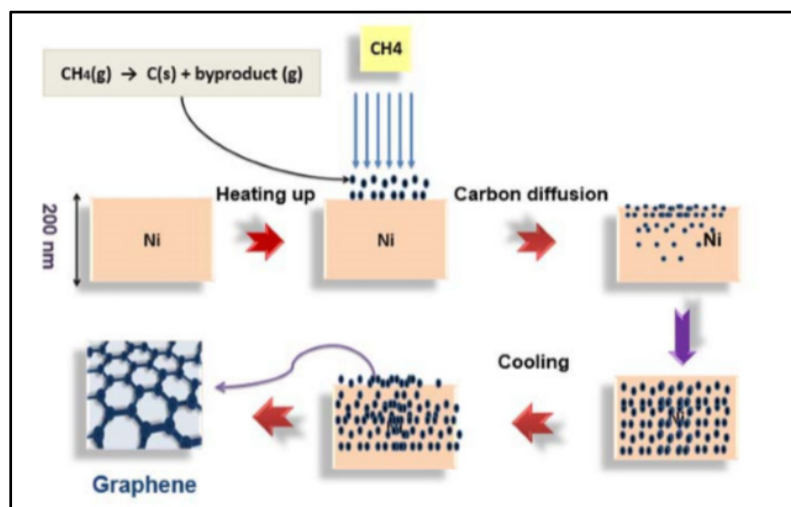


Figure 1.10 Graphene synthesis on nickel wafer
Taken from Al-Shurman & Naseem (2014, p. 2)

On a copper film, graphene is grown in the presence of a hydrogen and methane atmosphere at a high temperature of approximately 1000°C (Figure 1.11). The copper induces the catalytic decomposition of methane, which results in a single layer of carbon atoms that are well bonded

to the copper surface. Graphene synthesis on the copper has some advantages, such as better control of graphene characteristics and an easy transfer to a support for storage.
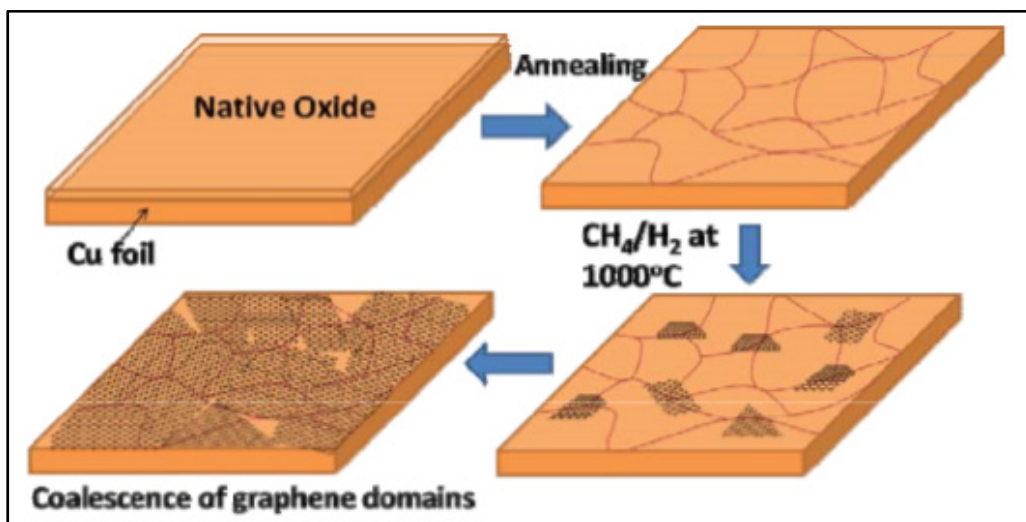


Figure 1.11 Graphene synthesis on copper wafer
Adapted from Mattevi, Kim, & Chhowalla (2011)

The graphene layer is transferred to a support by spin-coating the graphene with an organic polymer, typically PMMA. The metal substrate can then be safely removed by an acid wash. Finally, the PMMA/graphene film is washed by deionized water to remove any metal residue and placed on another support, usually made of Si/SiO2.
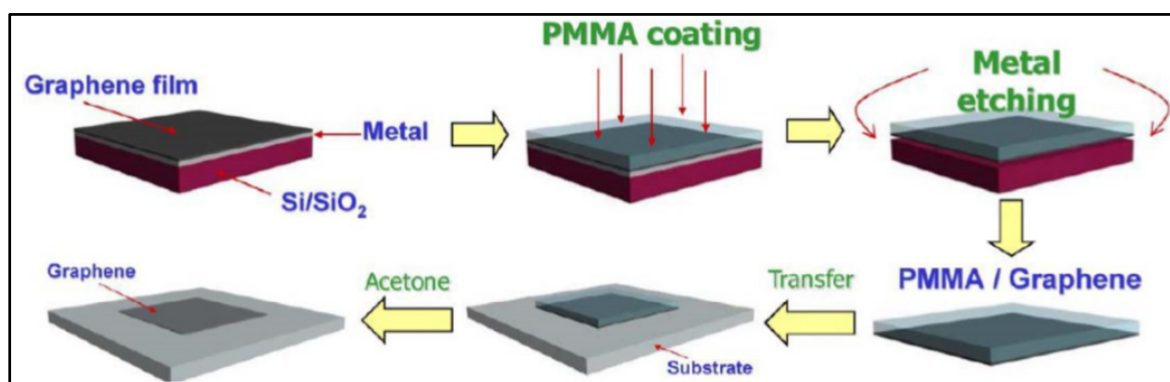


Figure 1.12 Transfer of the graphene layers
Adapted from Y. Zhang et al. (2013)

The chemical vapor deposition method guarantees graphene layers which are continuous and large in area. This makes it suitable for nanoelectronics and photovoltaic applications. Academic authors, such as (X. Li et al., 2009), have succeeded in synthesizing high-quality single-layer graphene on copper films. Nonetheless, this method is not suitable for graphene as a filler in polymers because of its small-scale production.

## 1.4.2    Top-down Exfoliation

The top-down processing method is more appealing than the bottom up. It starts from the graphite which is abundant raw materials. Extracting the graphene from the graphite is cheaper than synthesizing the graphene on copper or nickel wafer. In 2015-2016, the worldwide graphite production was around 2.5 million tons (Jara, Betemariam, Woldetinsae, & Kim, 2019). Figure 1.13 shows different extracting methods of graphene or graphene's derivatives from graphite.
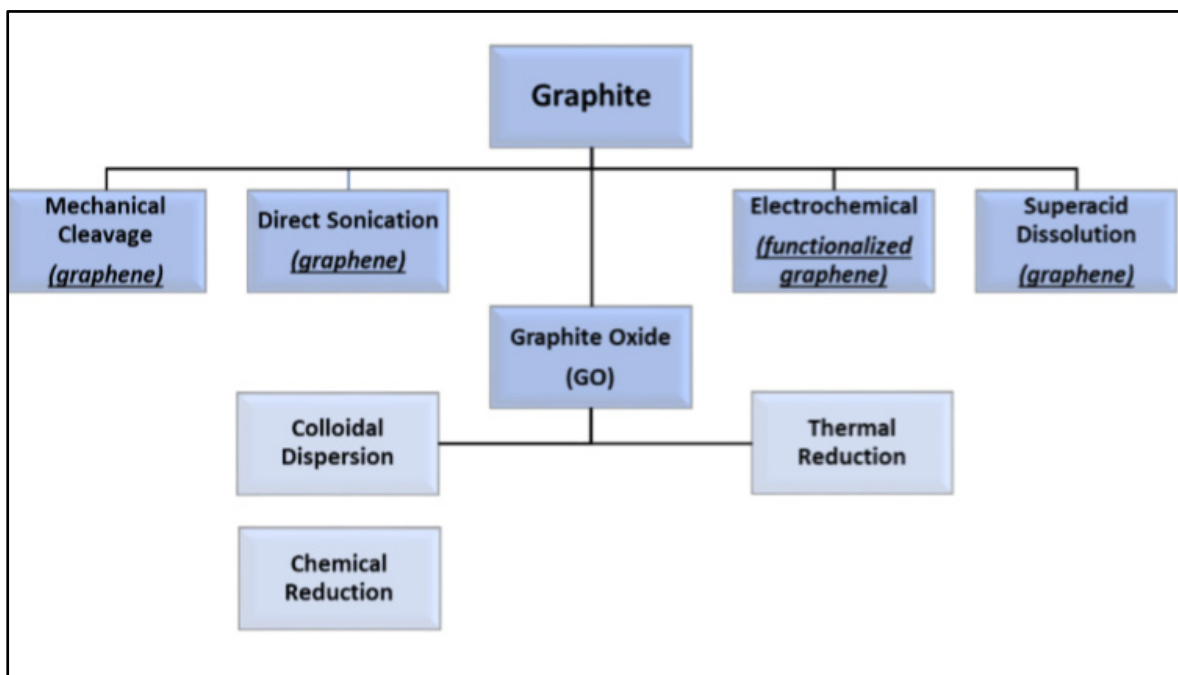
Figure 1.13 Graphene exfoliation top down methods
Taken from S. Hamidinejad (2019, p.15)

## 1.4.2.1 Graphene Direct exfoliation

Figure 1.14 depicts the micromechanical exfoliation approach which is also known as simple scotch tape peeling. Through this method, we can synthesize a few-layer graphene (FLG) (Novoselov, 2004). The graphene is peeled off from the graphite surface via an adhesive tape. Multiple graphene layers are now stuck on the tape. Then the graphene layers should be transferred onto a substrate which can be done by pressing the tape against the substrate surface. The micromechanical exfoliation approach yields to high quality and large size graphene sheets with almost no defects (Krane, 2011). It is also a direct and plain method that induces a few layers of graphene wafer with up to 10 μm of thickness (Al Imran, 2016). However, due to the small production scale, the scope of this method is restricted to only fundamental studies and it cannot be used for nano-composites applications (Novoselov, 2004).
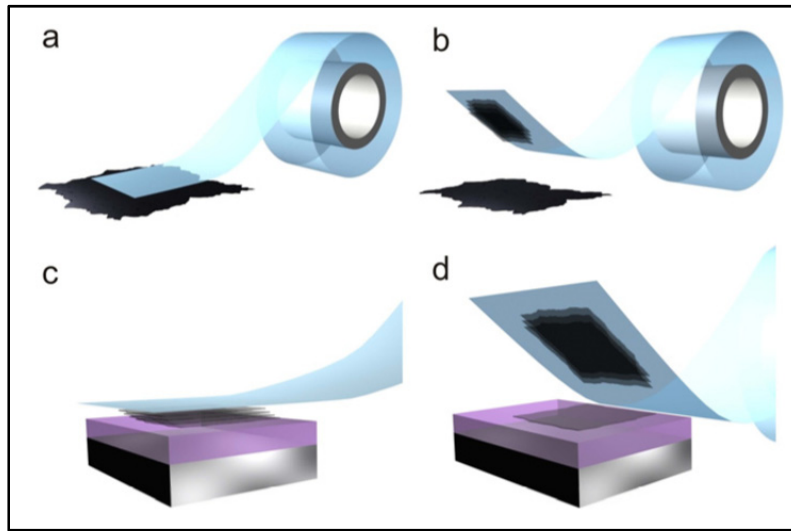


Figure 1.14 Micromechanical graphene exfoliation
Adapted from  Novoselov & Castro Neto (2012)

Direct sonication, also known as liquid-phase exfoliation, is a promising method for large scale graphene production. This method is comprised of three major steps: dispersion of graphite in an organic solvent, exfoliation, and filtration (Figure 1.15). Typically, the graphite is dispersed by means of bath sonication in either methyl-pyrrolidone (Hernandez et al., 2008) or polyvinyl-

pyrrolidone (Bourlinos, Georgakilas, Zboril, Steriotis, & Stubos, 2009). These solvents possess almost identical interfacial energy with graphene as it exists between the layers of graphite. (Lotya, King, Khan, De, & Coleman, 2010). This minimizes the energy barrier for the graphene to disassociate and allows it to be exfoliated (Su et al., 2011). Subsequently, the mixture is centrifuged to sort the graphene by particle size. Multi-layer and single-layer graphene produced via liquid-phase exfoliation are higher quality than is achieved in the micromechanical method. However, the method leads to smaller graphene particles.
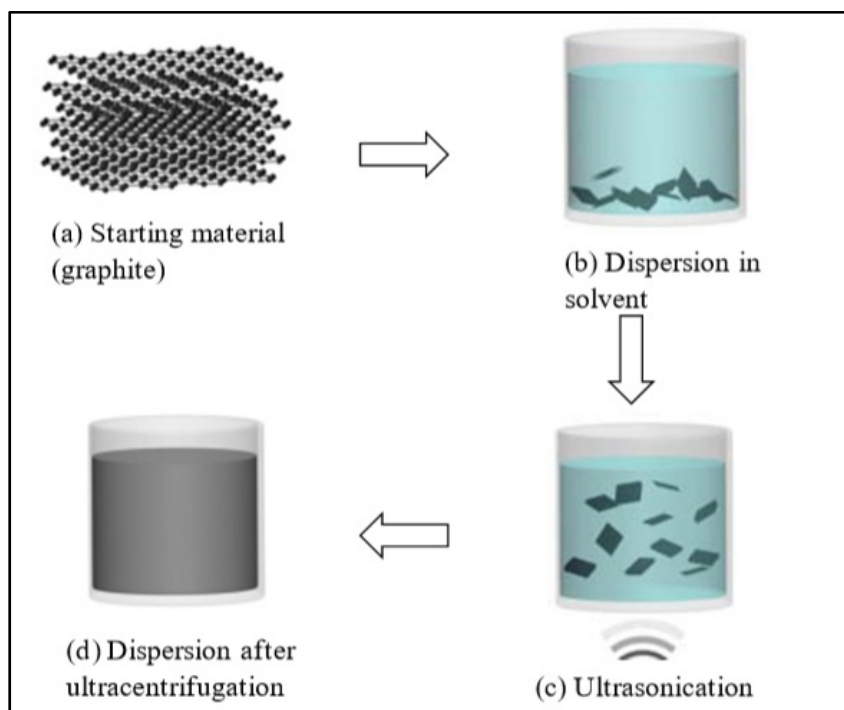


Figure 1.15 Graphene liquide phase exfoliation
Adapted from Bonaccorso & Sun (2014)

Similar direct approaches are presented in Figure 1.13, like super acid dissolution (Behabtu et al., 2010) and electrochemical functionalization which is often assisted with ionic liquids (N. Liu et al., 2008). These methods introduce some obstacles to production, such as safe handling of the hazardous solutions for the acid baths (Behabtu et al., 2010). The disposal process of hazardous substances is both expensive and dangerous. This limits the practicality of using an acid solvent for large scale graphene production.

### 1.4.2.2    Graphene Oxide GO

As shown in Figure 1.16, the graphite surface often contains functional groups, such as epoxide, carboxyl, and hydroxyl, with an average atomic ratio of 2/1/0.8 for C/O/H (S. Hamidinejad, 2019). A large quantity of graphene can be produced through the exfoliation and reduction of graphite (Kim, Abdala, & Macosko, 2010a). Typically, the graphite oxide is dispersed in an organic solvent, such as tetrahydrofuran (THF), or water. However, organic dispersion produces a thermal instability and significantly reduces the electrical conductivity (Kim et al., 2010a ; Stankovich, Piner, et al., 2006). A subsequent reduction can restore graphene's electrical properties. To accomplish this, there are two major routes: chemical reduction and thermal reduction.
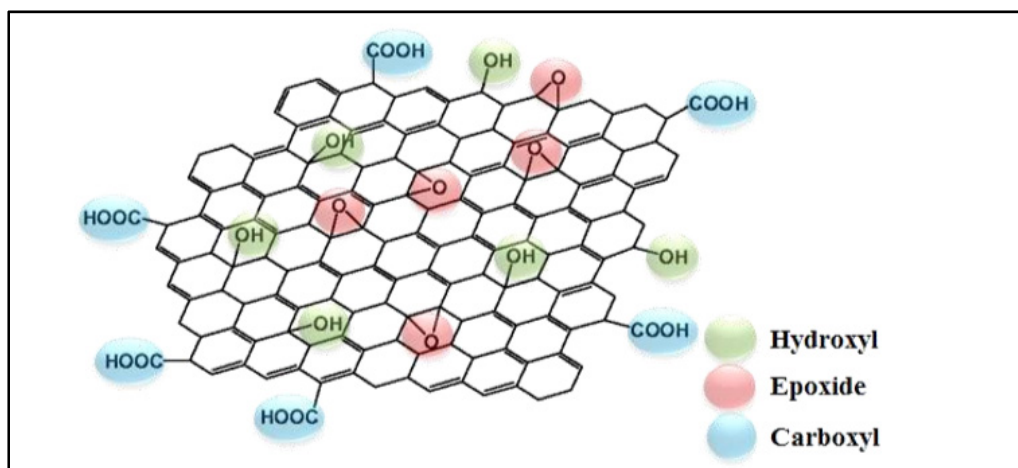


Figure 1.16 Hydroxyl, Epoxide, and Carboxyl groups
Taken from S. Hamidinejad  (2019)

- **GO chemical reduction**

The GO is mixed in water or an organic solvent, such as alcohol (S. Hamidinejad, 2019), until the color change is observed to yellow-brown (Al Imran, 2016). Then, the mixture must be strongly sonicated to render the solution as homogeneous as possible. Subsequently, a reducing agent is added: hydrazine (Lomeda, Doyle, Kosynkin, Hwang, & Tour, 2008 ; Hailiang Wang, Robinson, Li, & Dai, 2009) or dimethyl-hydrazine (Stankovich, Dikin, et al., 2006a). The

mixture is placed in an oil bath assisted with a water condenser. The temperature was maintained at 100°C for 24 hours (Al Imran, 2016). The reduced graphene oxide gradually accumulates at the bottom of the mixture and can be extracted by filtration (Stankovich et al., 2007). Chemical reduction is an effective method to restore the graphene electrical conductivity. Nonetheless, a considerable quantity of oxygen remains in the material, maintaining a ratio C/O of around 10/1 (Stankovich, Piner, et al., 2006). There are additional safety and cost considerations to using this method, as the solvent and reducing agent are relatively expensive and dangerous, hindering the prospects of large-scale production (Al Imran, 2016 ; S. Hamidinejad, 2019). Some alternative methods have been found using high pressure and temperature as a substitute for the expensive chemical solutions. Graphene oxide reduction can be fully achieved through dehydration of the hydroxyl in a super-heated water bath (120~200°C) and under high pressure (Nethravathi & Rajamathi, 2008 ; Yong Zhou, Bao, Tang, Zhong, & Loh, 2009).

- **GO thermal exfoliation and reduction**

Thermal reduction is more effective and less time consuming than chemical reduction. In this approach, the exfoliation and reduction are completed in one processing step. Dried graphite oxide is placed in a quartz tube furnace under inert gas (Al Imran, 2016 ; McAllister et al., 2007). The material is then exposed to a sharp increase in temperature of at least 2000°C/min until it reaches 1050°C (Al Imran, 2016). This rapidly oxidizes the functional groups on the surface of graphite oxide (S. Hamidinejad, 2019) which drives exfoliation as the produced carbon dioxide creates internal material pressure which overcomes the van der Waals bonding forces (S. Hamidinejad, 2019 ; Schniepp et al., 2006). This approach usually results in 30% of weight reduction which is explained by the combustion of the organic functional groups (Schniepp et al., 2006). Furthermore, the carbon dioxide expansion induces a volumetric expansion of approximately 100-300 times and generates reduced graphene oxide particles with a highly wrinkled surface structure (Schniepp et al., 2006).

## 1.5      Graphene Dispersion

Multiple methods have been developed to disperse effectively the graphene particles within the epoxy matrices. Three of these approaches are dominant in scientific literature as well as in industrial installations: mechanical dispersion, three-roll milling (3RM), and ultrasound sonication. In this section, the theoretical aspects of each method will be illustrated to highlight their advantages and disadvantages.

### 1.5.1      Mechanical Dispersion

The equipment used in mechanical dispersion is presented in Figure 1.17. This machine is equipped with a stator that contains drain holes and a rotating blade that is mounted on the mixer shaft. The increasing rotational speed induces a strong vortex of vacuum forces that pull the mixture of polymer and graphene into the center of the rotating blades and then push it back to the outside of the stator, creating intense shear mixing. The dispersion and exfoliation occurs as the mixture passes through the gap between the edge of the blades and the stator.  As the shear mixing progresses, the particle size decreases and the mixture becomes more homogeneous with microscale or nanoscale graphene (Zou, 2016).  Graphite nanoplatelets are comprised of a small number of graphene layers stacked together. The weak Van der Waals forces which hold the layers together can be readily broken by shear forces, jet cavitations, collisions, and shock waves produced during mechanical dispersion (Choi, Lahiri, Seelaboyina, & Kang, 2010 ; Knieke et al., 2010). As reported in (L. Liu, Shen, Yi, Zhang, & Ma, 2014), high rotational speed generates sufficient shear forces to peel graphene layers off of the graphite particles. Jet cavitation occurs when the flow velocity changes abruptly (Shen, Li, Yi, Zhang, & Ma, 2011) which exfoliates the graphene particles even further. Collisions occur on the edge of the drain holes (Utomo, Baker, & Pacek, 2009) and as random collision events between particles in the suspension. The impact of the degree of exfoliation on the electrical and mechanical properties was documented by Raza, Westwood, & Stirling (2012) who incorporated graphene particles in epon 828 epoxy by high shear mixing at 2500 rpm for 20 minutes and achieved a high electrical conductivity of $3x10^{-2}$ S/m with 20 wt. % of

graphene. King, Klimek, Miskioglu, & Odegard (2013) utilized the same rotational speed (2500 rpm) but for a longer duration of 40 minutes. In that work, the electrical conductivity peaked at 5 wt. % of graphene with a maximum of $3\times10^{-5}$ S/m and the percolation threshold occurred with only 2 wt. %.
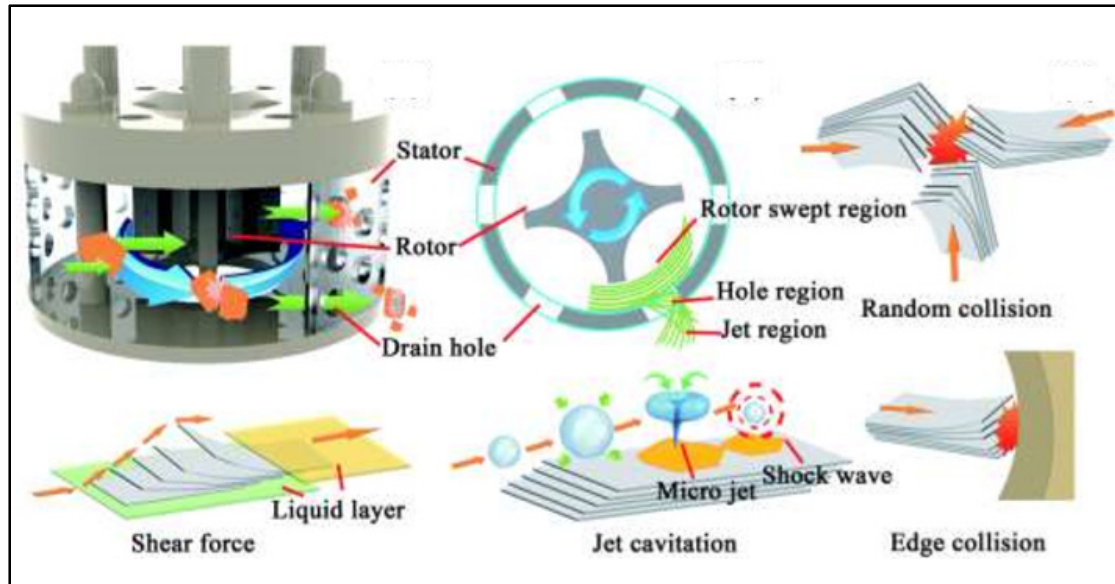


Figure 1.17 High shear mixing mechanisms
Taken from L. Liu et al. (2014)

## 1.5.2    Three-Roll Milling (3RM)

The three-roll mill machine is primarily comprised of three cylindrical rolls: the feed, the center, and the apron. Figure 1.18 shows a simplified example of the machine. The feed and apron rolls rotate in the same direction, while the center roll rotates in the opposite direction. Typically, each roll rotates at a different speed, such that $\omega_{center}$ is three times greater than $\omega_{feed}$ while $\omega_{apron}$ is three times greater than $\omega_{center}$. The mixture is poured into a narrow gap between the feed roll and the center roll. The opposite rotational direction and the difference in velocity generates high shear forces that exfoliate and homogenize the mixture (Thostenson & Chou, 2006). The mixture moves through the rolls until it reaches the scraper blade which peels off the mixture from the apron roll and deposits it into a collecting vessel. This cycle is typically repeated several times until the required homogeneous quality is achieved (Zou, 2016). This

approach allows control of the composite properties by varying the gap between the rolls. However, the minimum gap distance is generally around ~1-5 μm which limits the degree of exfoliation to the microscale and prevents it from splitting the agglomerated particles (Gojny, Wichmann, Köpke, Fiedler, & Schulte, 2004). Moreover, this approach is suitable only for viscous materials and can thus only be used for specific types of polymers.

Gojny et al. (2004) used the 3RM to disperse the carbon nanotube (CNT) in an epoxy matrix, reporting a remarkable improvement of the electrical conductivity. The percolation threshold was achieved with only 0.2 wt. % of CNT, where the electrical conductivity sharply increased from $5x10^{-6}$ to $2x10^{-3}$ with 0.2 wt. % and 0.3 wt. % respectively. A similar pattern was presented in (Thostenson & Chou, 2006), where the dispersion of CNT in Epon 862 by the same approach (3RM) lead to a percolation threshold of only 0.1 wt. %. The electrical conductivity was enhanced by 12 orders from $1.56x10^{-15}$ to $1x10^{-3}$ S/m. According to Al Imran (2016), most of the presented studies that sought to incorporate the graphene in the epoxy matrix through a scalable approach like 3RM could not achieve the percolation threshold with low graphene content (0.1-1.0 wt. %). Raza et al. (2012) found a discernable improvement with high graphene concentration (8-25 wt. %) and no enhancement at low filler load. The dispersion of graphene platelets requires two vital conditions that must be satisfied: thorough delaminating and rigorous dispersion of the graphene particles (Zou, 2016).
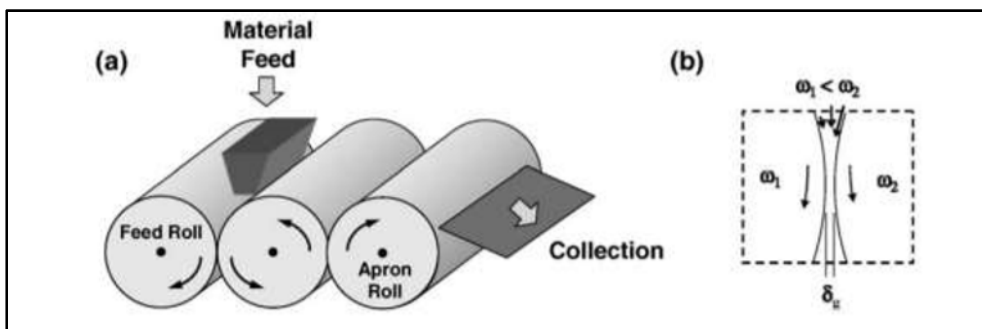


Figure 1.18 Three-Roll Milling schematic mechanism
Adapted from Thostenson & Chou (2006)

### 1.5.3    Ultrasound Sonication

Ultrasound sonication is an approach that has been widely used to disperse fillers in matrices. Figure 1.19 schematically shows the sonication exfoliation mechanism. In this technique, an intense vibration higher than 20 kHz (Al Imran, 2016) is typically used. This high-speed wave vibration results in liquid cavitation and liquid jet which disperse and exfoliate the filler.
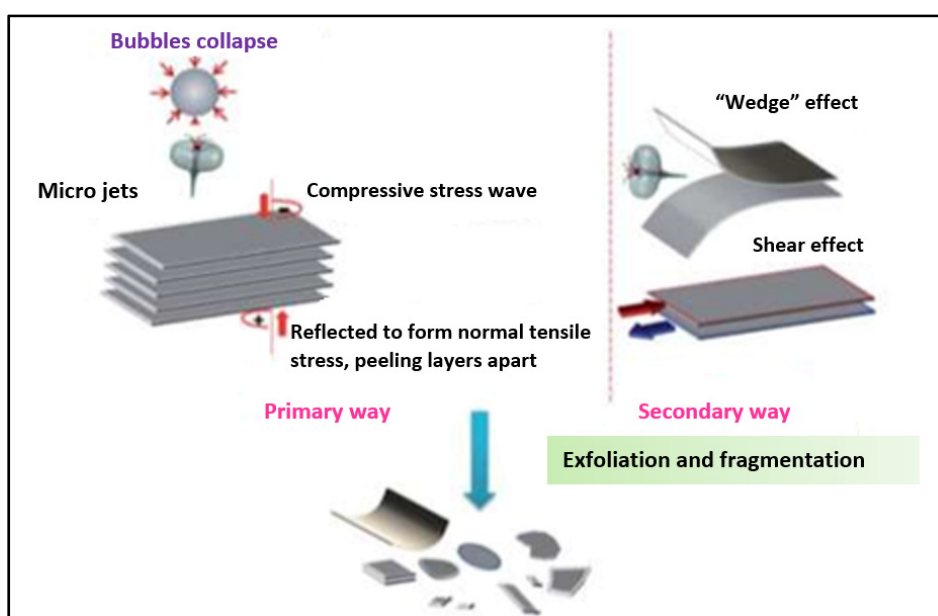


Figure 1.19 Ultrasound sonication mechanisms
Taken from Yi & Shen (2015)

The filler exfoliation process is primarily governed by two mechanisms: micro-jet and wedge (Yi & Shen, 2015). Liquid cavitation creates a large number of bubbles that collide with the filler particles and collapse to form local shock waves and micro-jets. These effects create compressive and tensile stresses which are applied perpendicularly on the filler surface while in-plane forces (wedge effect) are generated, causing exfoliation and fragmentation of the filler particles. Though ultrasound sonication provides an intensive and effective delamination, it has some limitations and detrimental effects. For instance, this approach is most suited for low-viscosity mixtures which also require the addition of a solvent. The intense vibration causes rapid heat generation, which requires an active cooling system to mitigate the temperature, and

can drive the evaporation of the solvent. Graphene particles in these mixtures tend to re-agglomerate in the absence of the solvent and the presence of excess solvent harmfully affects the mechanical properties of the final composite. (Al Imran, 2016). Wajid et al. (2013) attempted to circumvent this issue by adding a third substance to the mixture, polyvinyl-pyrrolidone (PVP). However, the PVP tends to affect detrimentally the mechanical properties of the composite polymers. In addition, ultrasonication can deteriorate the properties of the filler. Bracamonte, Lacconi, Urreta, & Foa Torres (2014) investigated the sonication time and the induced flaws in graphene particles; underlining that longer sonication time leaves basal plane defects and short time creates edge defects. Other authors have successfully employed ultrasound sonication, such as Monti et al. (2013) who dispersed the graphene in epoxy, improving the electrical conductivity from $1.0 \times 10^{-15}$ to $9.98 \times 10^{-7}$ S/m with only 1 wt. % of filler. Similarly, Wajid et al. (2013) achieved a percolation with less than 0.3 wt. % with four folds of electrical conductivity enhancement. However, most of the studies in the literature that used sonication without a solvent did not show any significant amelioration as those who used the solvent. The use of solvents improves the electrical properties but may reduce the mechanical properties of the composite polymers.

## 1.6    Porosity and Void

Voids and porosity present one of the most common problems in composite materials. However, these two phenomena can be difficult to distinguish and arise from different processing effects. Porosity generally refers to small, often interconnected defects that are pervasive through the structure. In contrast, the term void is generally used for larger, discrete pores (Campbell, 2010a) These undesirable defects can arise from multiple problems in the processing such as inadequate vacuum pressure, unstable curing pressure, and temperature. It is practically impossible to eliminate all flaws, but best practices generally restrict porosity and voids to be 1% of the total volume. This can be an important and detrimental factor on the composite's mechanical properties. For instance, interlaminar shear strength decreases by about 7% per 1% of porosity (Mayr, Plank, Sekelja, & Hendorfer, 2011). Figure 1.20 displays the behavior of ILSS with respect to porosity.
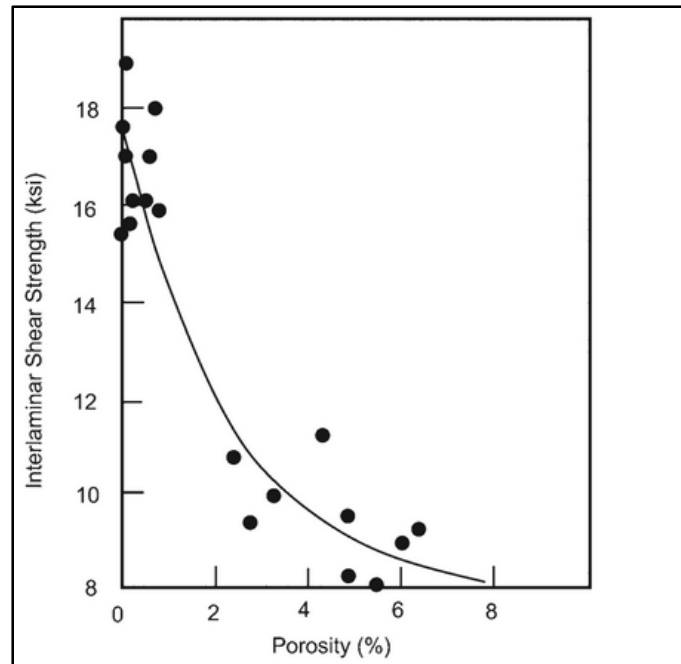
Figure 1.20 ILSS vs porosity
Taken from Campbell (2010a, p. 395)

There are two different characterization methods used to evaluate defects in composites. The first are non-destructive methods, such as X-ray or infrared thermography, and ultrasonic attenuation. The second category are destructive methods, such as micrograph image processing, chemical digestion, and matrix burn off. The nondestructive methods are well suited for preventive maintenance and tracking a component's life span. Destructive methods can provide a more comprehensive characterization in laboratory investigations. Specifically, micrograph image processing is unsophisticated in equipment requirements and can be used to establish a relation between ultrasonic attenuation and porosity content (Daniel, Wooh, & Komsky, 1992) and to obtain a statistical information about the pores' dimensions and orientation (Hsu & Uhl, 1987). Micrograph image processing consists of three major steps. The first step is to polish the sample to obtain smooth surface. Then, microscope images must be acquired over the whole sample area with a magnification of 50X (Kite, Hsu, Barnard, Thompson, & Chimenti, 2008). Finally, an open source software named Image J can be used to segment this image into three sections (background, composite, and void). This step is assisted with a machine learning algorithm, where the operator introduces the criteria for the

different sections to the software. By doing so, the software will be able to determine each section percentages of the entire collection of images.

## 1.7      Polymer Electrical Properties

This part of the literature review discusses the basic principles of the polymer electrical properties such as the dipole moment, the difference between the dielectric materials and insulative materials, polarization phenomenon and its causes, and thermal and electrical conductivity of polymer matrix loaded with conductive filler.

### 1.7.1     Electric Dipole Moment

The electric dipole moment is typically denoted by μ and it is defined as a vector from the negative charge toward the positive charge. The magnitude of this vector is given by equation (1.1).

$$\mu = qr \tag{1.1}$$

where q is the absolute value of the positive or negative charges and r is the distance between positive and negative centers. For a given material that has "n" positive and negative charges, the total value of the electric dipole moment will be presented by:

$$M = \sum_i^n \mu_i \tag{1.2}$$

Take a sample of dielectric material, with a volume "V". The polarization "P" of this sample can be mathematically described through the ratio of the total amount of the electric dipole moment "M" over its volume "V". The polarization is measured in Coulomb per square meter (C/m²) and it is almost the same as the charge surface density σ (Psarras, 2018).

## 1.7.2    Dielectric Materials versus Insulating Materials

In literature, we frequently confuse the terms "dielectric materials" and "insulating materials". Indeed, the semantic "dielectric" covers a wider range of materials. Dielectric materials contain an electrostatic field as well as they can be polarized under the effect of an electric field. On the other hand, insulators are a sub-group of the dielectric materials that prevent the flow of charge in electrical components (Psarras, 2018). In this direction, there are two types of dielectric materials namely: polar and nonpolar materials.

- Polar dielectric: In the absence of an applied field, the molecules possess a permanent dipole moment because the center of the positive and negative charges are not coincident. This category includes materials that have a nonsymmetrical molecular structure (Figure 1.21) (Serenari, 2019). A typical example of a polar molecule is the HCl with a dipole moment of $\mu = 3.43 \times 10^{-30}$ Cm (Psarras, 2018).
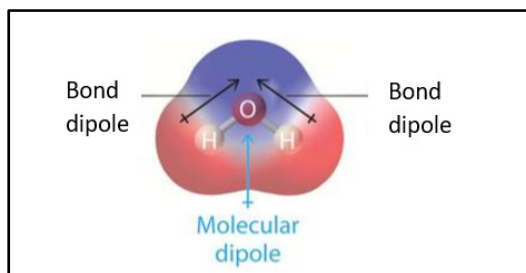


Figure 1.21 Polar molecule H2O
Adapted from Serenari (2019)

- Nonpolar dielectric: this type of material does not have a permanent dipole moment and instead experience polarization due to a lack of symmetry in the distribution of their negative and positive charges. CO2 and CH4 molecules present good examples of nonpolar dielectric (Figure 1.22).
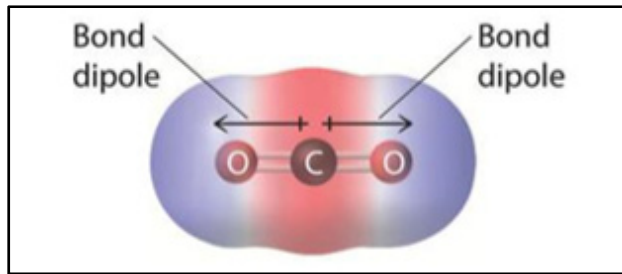
Figure 1.22 Nonpolar molecule CO2
Adapted from Serenari (2019)

### 1.7.3 Dielectric Properties of Polymer Composites

A polarization of dielectric material can be explained by the concept of two parallel plate capacitors. Upon the application of direct current DC with voltage V, an electric field is generated between plates with a value equal to:

$$E = \frac{V}{d} \tag{1.3}$$

where V is the voltage and d is the distance separating the plates. The electrons within the dielectric material will change their orientation as soon as the electric field is applied. Figure 1.23 depicts the transmission of dielectric material from the "unpolarized" to "polarized" state.
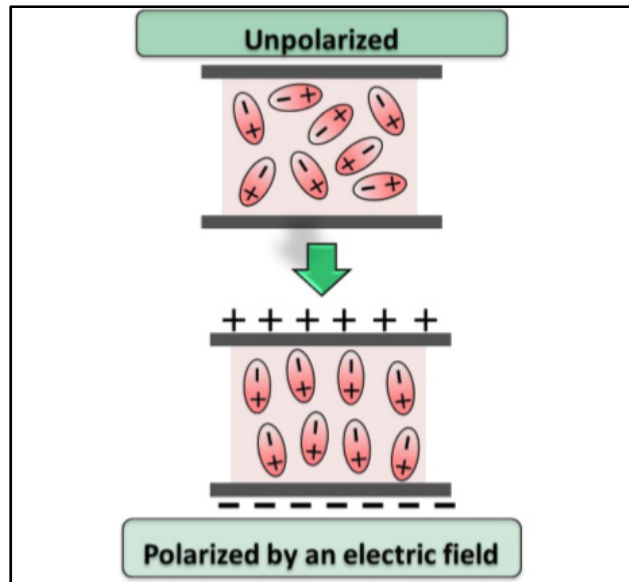
Figure 1.23 Polarization of dielectric material
Taken from S. Hamidinejad (2019)

There are four principle mechanisms of polarization:

- Electronic polarization: the electrons near the nucleus change their positions. This type of polarization takes place in almost all the dielectric materials, it appears at a high frequency $10^{15}$ Hz (Mebarki, 2017).

- Ionic polarization: this is the principal mechanism of polarization in glass, ceramic and inorganic crystals (S. Hamidinejad, 2019). It consists of the displacement between positive and negative ions that occurs under an applied electric field. This particularly happens within the range of infrared frequency at around $10^{13}$ Hz (Mebarki, 2017).

- Dipolar polarization: This type of polarization is linked to the orientation of the molecules under the effect of the electric field and emerges at higher frequency (higher than $10^{13}$ Hz). The direction of these molecules largely depends on the intrinsic bonding interaction between these molecules.

- Interfacial polarization: also known as the Maxwell-Wagner-Sillar effect, this type of polarization dominates in the composite polymer, especially when there is a significant variance between the electrical properties of the filler/polymer (Psarras,

2018). Under the effect of an electric field with a frequency under the range of mega hertz, an intensive amount of charge gathers at the interface filler/polymer. This was explained by the concept of relaxation time which is given in equation (1.4). The large gap between the filler conductivity and the polymer permittivity considerably increases the relaxation time (equation (1.4)) which facilitates the interfacial polarization (S. Hamidinejad, 2019).

$$\tau = \frac{\varepsilon}{\sigma} \qquad (1.4)$$

where $\varepsilon$ is the dielectric constant and $\sigma$ is the conductivity. One of the fundamental concepts of the parallel capacitor is that when we put a vacuum in between the plates, the accumulated charges will be equal to:

$$Q = \varepsilon_0.E \qquad (1.5)$$

where $\varepsilon_0$ is the free space permittivity. More charges can be stored by the capacitor if dielectric material is used between the parallel plates. This additional charge is given by Eq. (1.6)

$$P = Q.(\varepsilon_r - 1) \qquad (1.6)$$

where $\varepsilon_r$ is the permittivity of the dielectric. Usually, the permittivity is expressed as a complex function with respect to the frequency ($\omega$) (K. Yang, Huang, Huang, Xie, & Jiang, 2013).

$$\varepsilon(\omega) = \varepsilon'(\omega) - i\varepsilon''(\omega) \qquad (1.7)$$

where $\varepsilon'(\omega)$ is the real part and $\varepsilon''(\omega)$ is the imaginary part. The real part of the dielectric permittivity is directly linked to the type of polarization. Higher polarization results in an increase in the real part and vice-versa (K. Yang et al., 2013). Figure 1.24 highlights that interfacial polarization induces the highest real part of the primitivity while electronic polarization induces the lowest magnitude of the real part. The imaginary part of the dielectric

constant represents an idea about the dielectric loss which is often denoted by tan (δ), and it is presented by the ratio of the imaginary part over the real part.
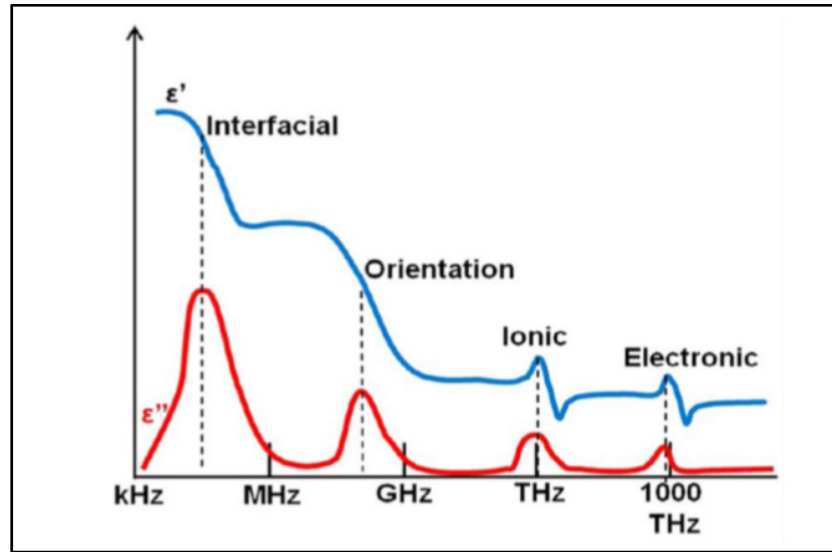


Figure 1.24 Real part, Imaginary part versus the frequency
Adapted from Fredin, Li, Lanagan, Ratner, & Marks (2013)

### 1.7.4    Electrical Conductivity in Polymer Composites

A conductive electrical grid within the polymer can be construed and predicted through several means such as statistical models, geometric models, and thermodynamic models (Abbasi, Carreau, & Derdouri, 2010 ; Lux, 1993). However, at higher filler percentages, the percolation theory is the best to describe this physical phenomenon (Weber & Kamal, 1997). Equation (1.8) embodies this theory:

$$\sigma = \sigma_{f.}(\varphi - \varphi_c)^t \tag{1.8}$$

Where $\varphi_c$ is the percolation threshold, $\varphi$ is the filler volume fraction, $\sigma_f$ is the filler conductivity, $\sigma$ is the composite conductivity, and $t$ is the scaling exponent. The distance between conductive filler particles plays a vital role in the electron transportation. A small interparticle spacing of less than 0.5 nm enables electron conduction within the insulator

polymer. Figure 1.25 shows that the electrical conduction varies dramatically with the distance of the particle. For distance above a critical value, the effect of the conductive particles will be negligible in the overall composite. On the other hand, when the particles are in close enough proximity, a conductive cluster can be created, this cluster presents the least resistive path within the insulator resin. Polymer composites with large networks of conductive graphene can form a conductive grid across the material.
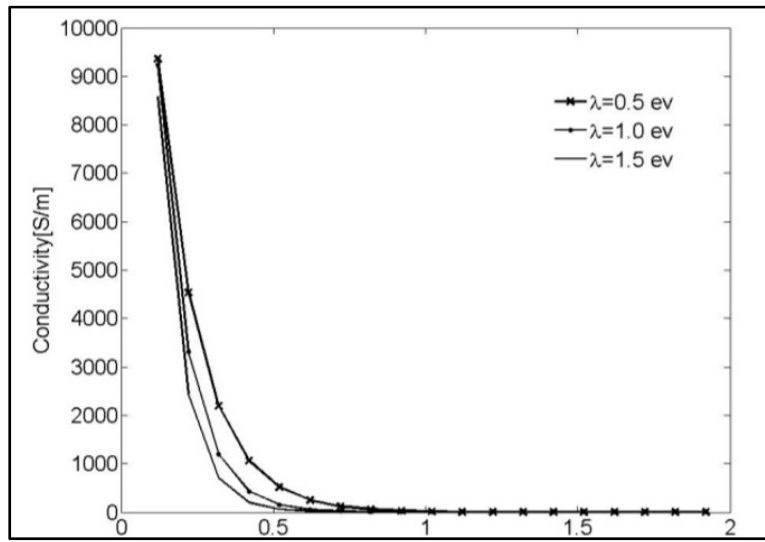


Figure 1.25 Tunneling distance [nm]
Adapted from Oskouyi, Sundararaj, & Mertiny (2014)

The first conductive mode is called tunneling and hopping which is usually occurs at low filler percentage. (C. Li, Thostenson, & Chou, 2007 ; Roldughin & Vysotskii, 2000). Simmons (1963) assumed that the filler has a cylindrical disk shape, under this hypothesis he has given a mathematical equation of the tunneling resistivity.

$$\varphi_{tunnel} = \frac{h}{e^2\sqrt{2m\lambda}} exp\left(\frac{4\pi d}{h}\sqrt{2m\lambda}\right) \tag{1.9}$$

Where h is the Plank constant, m is the mass of the electron, d is the tunneling distance (distance between two fillers), and $\lambda$ is the energy barrier height of the insulator. According to

the filler load, the electrical conductivity curve can be divided into three main segments which are given in Figure 1.26.
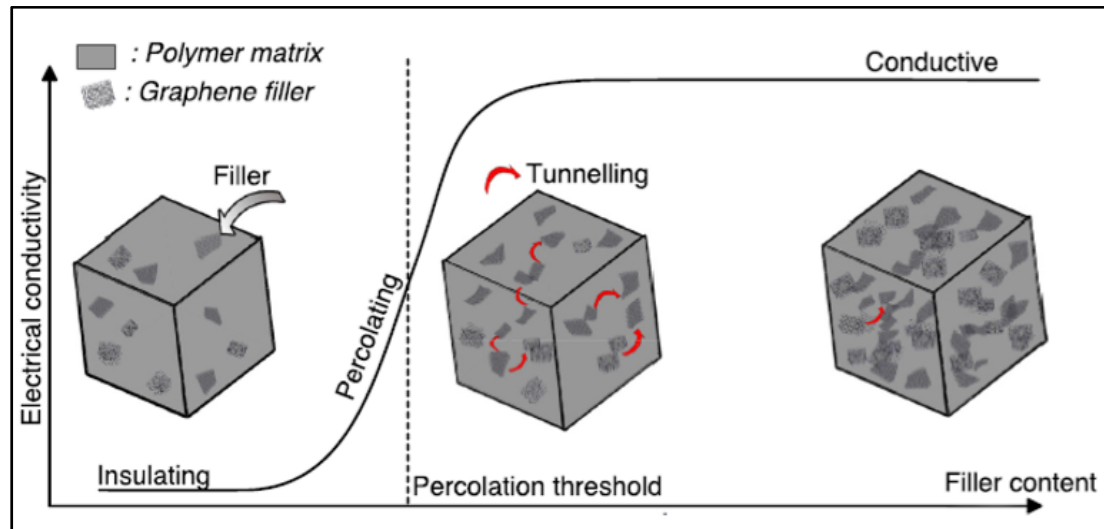


Figure 1.26 Different conductivity zones
Taken from Serenari (2019)

At low filler content: the gap between particles is too wide and the insulative nature of the polymer matrix inhibits the electron transportation. This zone is referred to as an insulating zone and the electrical conductivity is almost equal to the pristine polymer matrix ($10^{-13} \sim 10^{-11}$ S/cm) (M. Hamidinejad, Zhao, Chu, et al., 2018 ; Zuo et al., 2016). As the filler content increases, the gap between the particles decreases, and the electrical conductivity increases rapidly by many orders of magnitude. Consequently, the behavior of the material changes from insulating to conductive. The percolation threshold exists in this regime where the electrical conductivity is controlled by hopping and tunneling phenomenon. Beyond the percolation threshold, the electrical conductivity of the composite material maintains relatively stable with an order of typically $10^{-4}$ S/cm (S. Hamidinejad, 2019). The electron transport is now governed by mechanical contact between the particles which establishes a steady conductive network throughout the whole composite.

## 1.8       Thermal Properties (basic of heat conduction)

For low-temperature variation, the thermal conductivity can be defined by equation (1.10) (Balandin, 2011 ; Zou, 2016).

$$q = -K. \nabla T \qquad (1.10)$$

Where q is the heat flux, K is the thermal conductivity, and $\nabla T$ is the temperature gradient. This theory is valid only for small temperature variations because thermal conductivity is proportional to the temperature. The thermal energy transport is governed by acoustic vibration of the phonons and/or the electrons, this can be described by Eq (1.11) (Balandin, 2011).

$$K = Kp + Ke \qquad (1.11)$$

Where $Ke$ is the electron vibration and $Kp$ is the phonon vibration. In conventional metallic materials, the electron conduction is the main factor of thermal energy transportation which can be explained by the immense amount of free charge carriers. For example, the thermal conductivity of copper, at room temperature, is equal to K=400 Wm$^{-1}$K$^{-1}$ (S. Hamidinejad, 2019). In less conductive materials, the contribution of thermal conduction happens via electron and phonon vibration. In dielectrics, phonon vibration is the prevailing factor (Heid, 2015). With regards to the graphene and graphene-based polymer composites, the thermal conductivities are typically similar to those of metallic materials. Nonetheless, the phonon conduction remains the primary factor in thermal energy transport (Balandin, 2011 ; Pierson, 1993). This can be attributed to the strong Sp$^2$ bonding of the carbon atoms which guarantees strong energy transport through lattice vibration in the graphene particles (Balandin, 2011). In perfect crystals, phonon transport resistivity is almost equal to zero. However, in real crystals, the atomic vibrations are disrupted by crystallographic imperfections which induce phonon scattering (Cui et al., 2011 ; Huang, Iizuka, Jiang, Ohki, & Tanaka, 2012 ; Takezawa, Akatsuka, & Farren, 2003). In amorphous materials (epoxy resins), the thermal conduction is often governed by phonon scattering, especially in the vicinity of interfaces between the filler

particles and epoxy (Takezawa et al., 2003). Phonon scattering hinders the thermal conduction. This concept is illustrated in Figure 1.27 which shows the difference between phonon conduction and phonon scattering conduction.
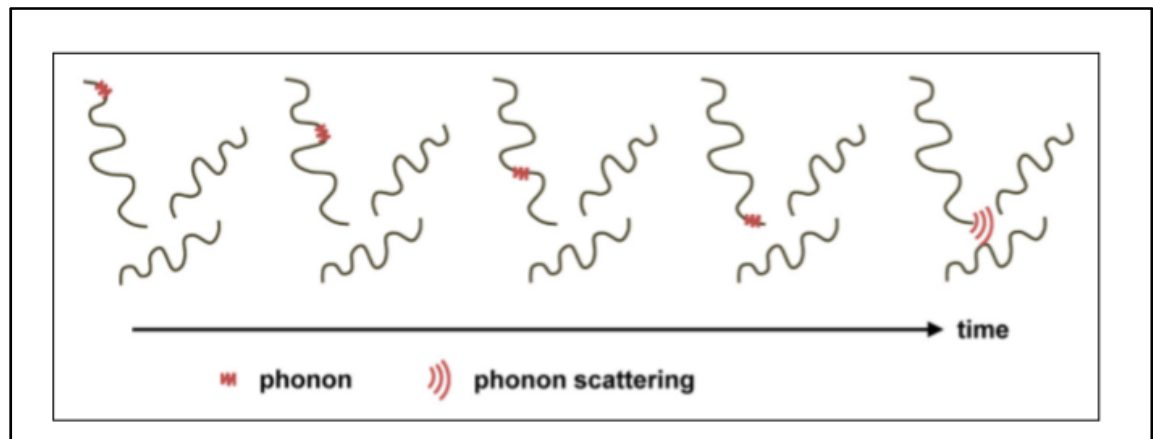


Figure 1.27 Thermal energy transfer via phonons within amorphous dielectrics
Taken from Heid (2015)

**CHAPTER 2**


**EFFECT OF GRAPHENE ADDITIVE ON THE ELECTRICAL AND THERMAL PROPERTIES OF THE POLYMER**

## 2.1     Introduction

Graphene material is a potential candidate as a filler to improve polymer properties. It has been reported that graphene has excellent thermal and electrical conductivity of around 5000 $Wm^{-1}K^{-1}$ and 6000 S/cm, respectively (Balandin et al., 2008 ; Kim et al., 2010a ; Seol et al., 2010). Graphene nanoplatelets (GnP) and few-layer graphene have attracted the attention of many researchers and industrial corporations who have sought to invent new graphene-based polymer composites, predominantly, to enhance the thermal dissipation of electronic components. This is because of the widespread demand for smart, lightweight, and thin electronic devices. The heat dissipation of electronic components becomes the principal obstacle in the advancement of this field. High performance and long lifespan of smart devices can be only guaranteed with electronic components that possess high heat dissipation quality (B. Tang, Hu, Gao, & Hai, 2015 ; Yongcun Zhou, Liu, & Wang, 2017).

In this chapter, the objective is to apply the principles of graphene filler as a conductivity enhancing filler to target a different application. This study aims to enhance the machinability of the CFRP materials by improving its thermal and electrical conductivity. Hence, improving the heat dissipation should reduce the machining temperature and extend the tool life. Graphene materials are a good filler for polymer matrices, with nano-clay and carbon nanotubes being the most relevant competitors. Both graphene and nano-clay are platelet type materials, characterized by a layered structure with high aspect ratios (>1000) (Chen, Wu, Weng, & Yan, 2001 ; Giannelis, 1996). Composite polymer based on platelet fillers demonstrated outstanding mechanical properties (Hossain et al., 2014 ; Paul & Robeson, 2008). However, graphene outperforms nano-clay by its excellent thermal and electrical properties (Yasmin & Daniel, 2004). In the meantime, carbon nanotube material possesses similar thermal and electrical properties as those of the graphene. Yet, it is not deemed as a

potential filler because they are relatively expensive, they often induce high matrix viscosity, and they have immense anisotropic functionality (Sandler et al., 2004). Consequently, the graphene nanoplatelet remains the ideal filler for the polymer matrix.

## 2.2 Methodology

In this section, we will present the sample preparation of the broadband spectroscopy (BDS) and the differential scanning calorimetry (DSC) as well as the fundamental principles of these approaches.

### 2.2.1 Sample Preparation

Differential scanning calorimetry (DSC) and broadband dielectric spectroscopy (BDS) samples were prepared using the same mixing process. Black graphene 0X was provided by Nano-Xplore Inc. These particles were precisely weighted and incorporated into the epoxy resin Marine 820. The weight fraction of graphene in the samples is presented in Table 2.1. These values were chosen based on the results of the literature. Several studies (King et al., 2013 ; Raza et al., 2012) have found a percolation threshold at high filler percentages ranging from 5 wt.% to 10 wt. %. In other words, it is difficult to find a discernable improvement at low filler content.

Table 2.1 BDS samples weight fractions

| Sample number | Sample weight fraction (wt. %) |
|---|---|
| 1 | 0 |
| 2 | 3 |
| 3 | 5 |
| 4 | 7 |
| 5 | 10 |

The graphene weight ratio was measured with respect to the total weight of the mixture which includes the epoxy weight, the graphene weight, and the hardener weight. All the proportions were calculated according to equations (2.1)- (2.4)

$$W_h = 0.18 \times W_{ep} \tag{2.1}$$

$$W_g = wt.\% \times W_t \tag{2.2}$$

$$W_t = W_{ep} + W_h + W_g \tag{2.3}$$

$$W_g = \frac{wt.\% \times 1.18 W_{ep}}{(1 - wt.\%)} \tag{2.4}$$

where $W_h$ is the hardener weight (g), $W_g$ is the graphene weight percentage, $W_{ep}$ is the epoxy weight (g), and $W_t$ is the total weight (g).

A high shear mixer (Silverson L5M-A Silverson Machines, Inc., East Longmeadow, MA, USA) was employed to mechanically mix, shear, and homogenize the graphene particles into the epoxy. The mixing process was organized into seven segments of 2 minutes each. The first segments begin with a low mixing speed at 2000 RPM. Then, with each consecutive segment, the mixing speed is increased to 3500 RPM, 6000 RPM, 8000 RPM, and 10000 RPM. To make sure that the mixture temperature will not exceed the glass transition temperature of the epoxy, an ice bath was utilized to limit the mixing temperature to a maximum of 40°C. For the last two segments, the iced bath was removed to let the temperature rise, reducing the mixture viscosity which facilitates the degassing process. Degassing was completed twice, immediately following the high shear mixing and after the addition of the hardener. The first degassing step is crucial because of the high quantity of air bubbles induced during high shear mixing. For this step, the mixture was placed for 1 hour under a maximum vacuum pressure of 29 inHg. For the second degassing step, the mixture was evacuated for 10 minutes. The hardener was added gently to avoid introducing any air bubbles. Figure 2.1 illustrates the major steps in the mixture preparation process.
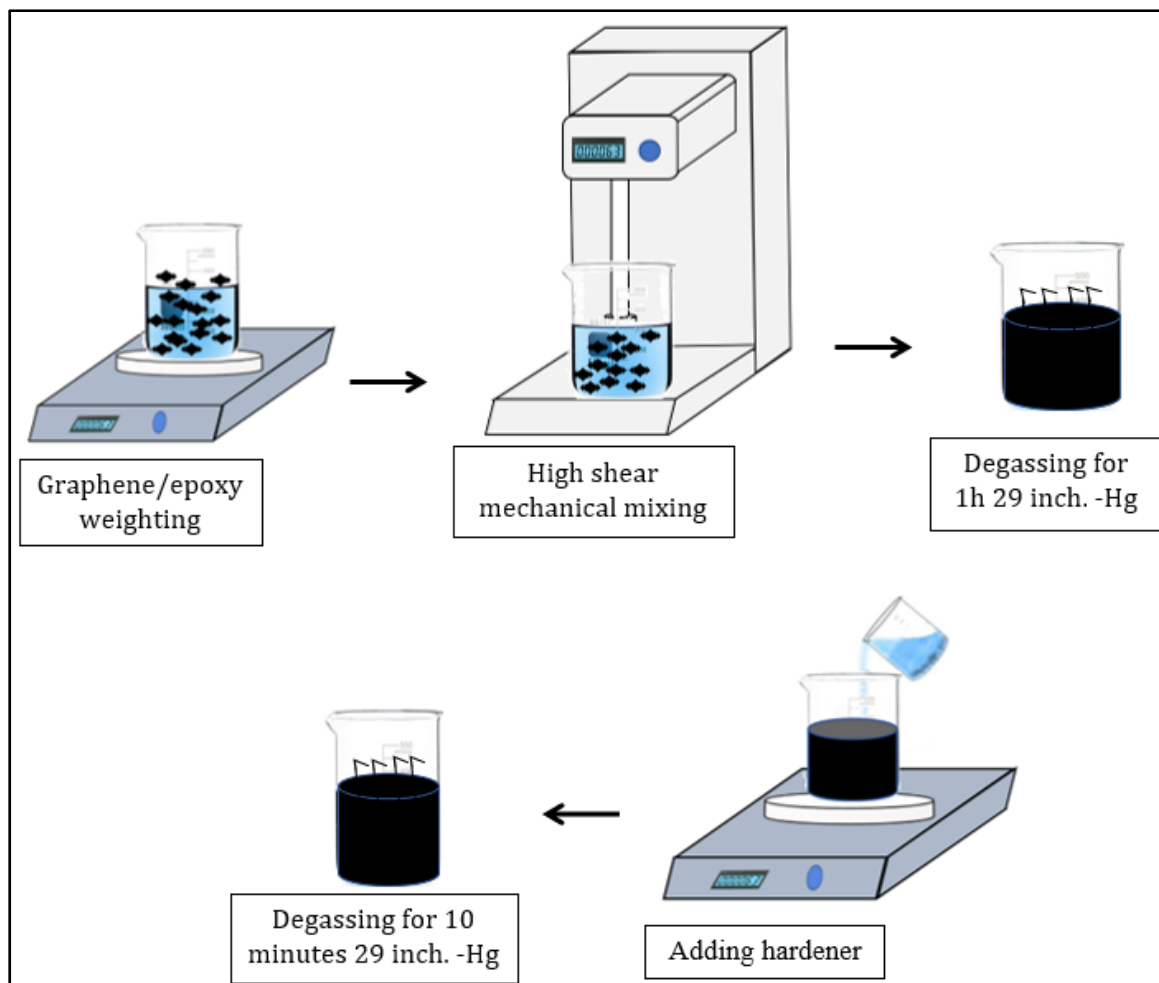
Figure 2.1 Graphene/Epoxy/Hardener mixing process

## 2.2.2 Sample Preparation of the Broadband Spectroscopy (BDS)

The BDS samples were prepared by the mixture casting into a silicone molding, shown in Figure 2.2. The mold was treated with a release agent to assure a smooth demolding. The samples were thin cylinders with an approximate diameter of 40 mm and thickness between 3 to 6 mm. The curing of the sample was done at room temperature for 24 hours. Before the measurement, the samples were polished to reduce the thickness to a maximum of 3 mm and to guarantee smooth surfaces.

Figure 2.2 Silicone molding of BDS samples

## 2.2.3    Sample Preparation for the Differential Scanning Calorimetry (DSC)

The DSC samples were prepared according to the ASTM E1269 standard. The preparation steps can be described as the following:

- The samples were sliced with a razor blade into thin layers.
- Samples weight must be between 5 mg to 15 mg.
- It is critical to ensure that there is no contamination of the samples because it can largely affect the experiment if the samples are mixed with foreign unwanted material.
- A flat, wide sample surface is highly desired to maximize the contact between the subjected material and the resistor-heater. The thickness of the layer must be less than the thickness of the sample's container to ensure proper sealing.
- The sliced layers of the tested material are placed into an aluminum pan (the sample container) and covered with an aluminum lid.
- The sealing process is done by a manual crimper press (Figure 2.3).

44
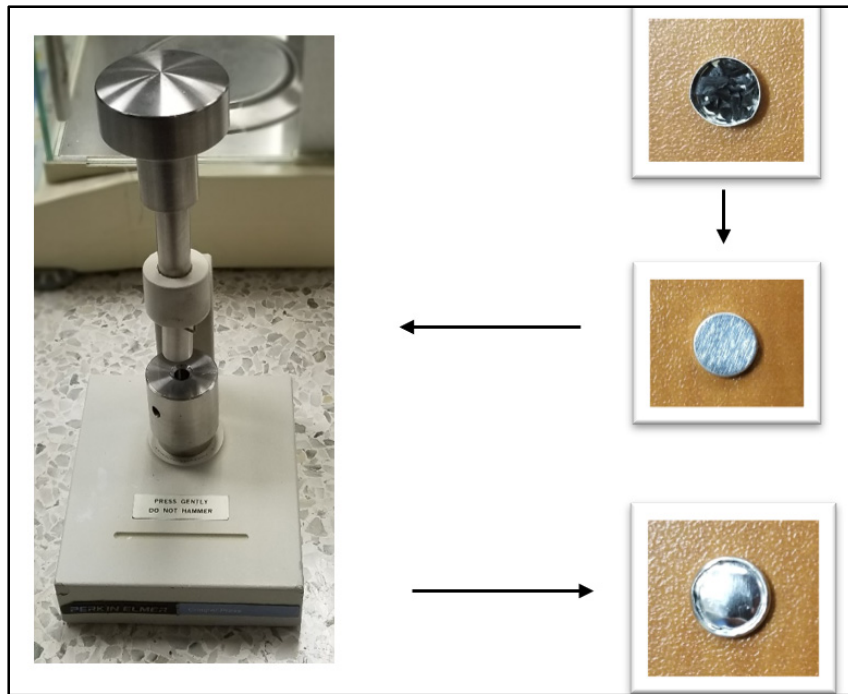


Figure 2.3 DSC sealing process

## 2.2.4 Configuration and Measurement Principle of the Broadband Spectroscopy (BDS)

Broadband dielectric spectroscopy (BDS) is a characterization method to measure several electrical properties such as the impedance, complex dielectric functions, and cross-plane conductivity. The targeted frequency range mainly coincides with the interfacial polarization band of frequency: from $10^{-2}$ Hz to $10^{+5}$ Hz. An alpha-A Frequency Response Analyzer (Novocontrol Technologies) acted as a signal generator and analyzer for this measurement. Figure 2.4 schematically presents the measurement principle.
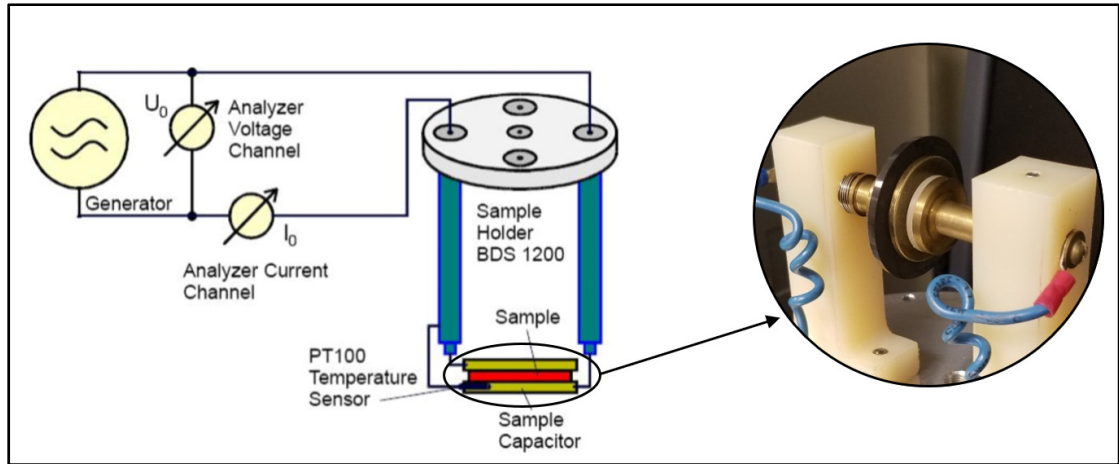
Figure 2.4 Principle of dielectric measurement with a factual specimen image
Adapted from Vasilyeva, Lounev, & Gusev (2013)

The tested specimen was well placed in between two external copper electrodes (Figure 2.4). The diameter of these electrodes must be slightly less than the diameter of the specimen. These electrodes are usually provided by the company with standard thicknesses, diameters, and materials grades. The thickness of the sample is precisely measured and introduced into the WinDETA software. For the electrical properties measurement, the machine follows these sequences of mathematical equations:

$$C = \varepsilon^* \times \varepsilon_0 \times \frac{\pi D^2}{4d} \tag{2.5}$$

where $C$ is the sample complex capacity, $\varepsilon^*$ the dielectric constant, $\varepsilon_0$ the free space permittivity, D the diameter of the electrodes, and d the sample thickness. The specimen is subjected to voltage $U_0$ with a variable frequency $\omega/2\pi$ which results in a measured current $I_0$. The phase shift between the voltage and the current is denoted as $\varphi$. Complex notation is used to better describe the voltage and the current with respect to their phases:

$$U(t) = U_0 . sin(wt) = Real(U^* e^{iwt}) \tag{2.6}$$

$$I(t) = I_0 . sin(wt + \varphi) = Real(I^* e^{iwt}) \tag{2.7}$$

Where

$$U^* = U0$$

$$I^* = I' + iI''$$

$$I_0 = \sqrt{I'^2 + I''^2}$$

$$tan(\varphi) = \frac{I''}{I'}$$

The dielectric function which is also known as the complex permittivity can be expressed as:

$$\varepsilon^*(w) = \varepsilon' - i\varepsilon'' = \frac{-i}{wZ^*(w)} \frac{1}{C_0} \qquad (2.8)$$

where $\varepsilon'$ and $\varepsilon''$ are the real and imaginary parts of the complex permittivity, $C_0$ is the capacity without sample, and $Z^*$ is the impedance which can be expressed by the ratio of $U^*$ over $I^*$. The complex conductivity can be derived from the complex permittivity as a real part and an imaginary part:

$$\sigma'(w) = w.\varepsilon_0\, \varepsilon''(w) \qquad (2.9)$$

$$\sigma''(w) = w.\varepsilon_0\, \varepsilon'(w) \qquad (2.10)$$

where $\varepsilon_0$ is the vacuum permittivity and $w$ is the angular frequency.

## 2.2.5    DSC Configuration Set-up and Basic Principles

There are two principle techniques of the differential scanning calorimetry:
- The power compensation.
- The heat flux.

The available instrument in ETS (École de technologies supérieure), is based on the heat flux approach. This approach uses two sealed aluminum pans: one contains the sample, and another contains a reference material (Figure 2.5). The heat is applied to both pans to maintain equal temperature. The difference of the thermal energy absorbed by each pan to maintain the temperature is measured as a function of temperature. The temperature is increased linearly as a function of time and the reference material should have a very well-defined specific heat capacity over the targeted temperature range. In contrast, the powder compensation approach measures the difference in the electrical power instead of the thermal energy.
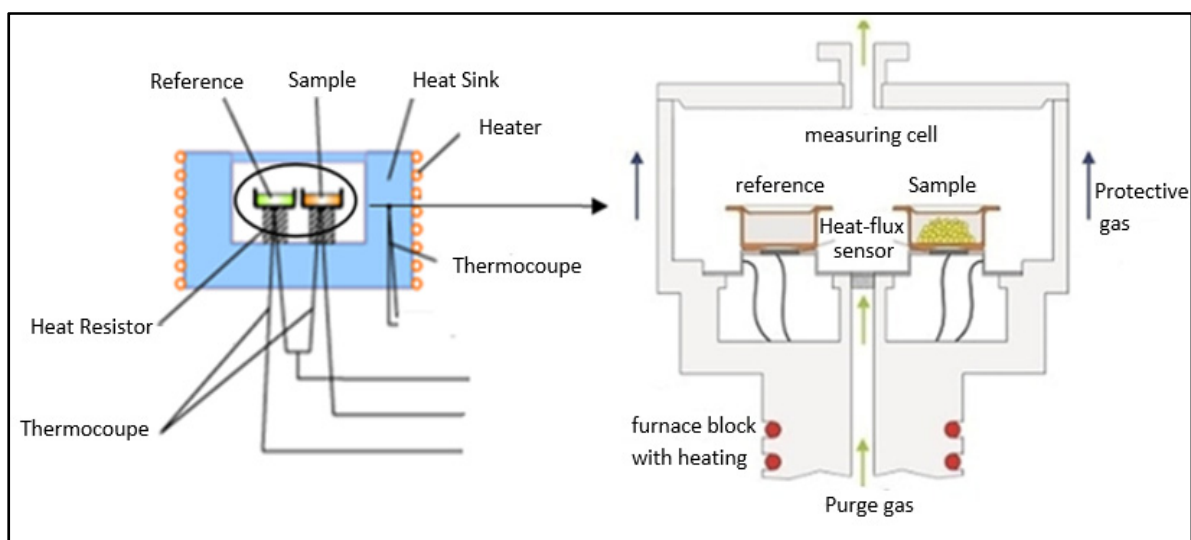


Figure 2.5 DSC heat Flux
Adapted from Bibi et al. (2015)

By differential scanning calorimetry, several properties of the material can be investigated:

- The glass transition temperature '$T_g$'.
- The temperature and heat ratios of crystallization and melting, typically denoted $T_c/T_m$ and $H_c/H_f$, respectively.
- Specific heat capacity '$C_p$' over a range of temperatures.
- Information on chemical reactions such as thermal curing, heat history, and purity analysis.

## 2.2.6     Specific Heat

According to the ASTM standard (2018), the specific heat capacity of an unknown sample can be measured by comparison to a well-defined reference material, such as the sapphire. However, it is imperative to calibrate the equipment beforehand using indium (In), during which an empty pan is used in the reference cell and indium is placed in the sample cell. The equipment can be calibrated by comparison to a built-in database containing the thermal information of the indium. The calibration can be confirmed by testing sapphire alongside an empty sealed pan. Finally, the sapphire is replaced with the unknown sample material to conduct the final measurement. The previous steps result in three curves similar to the ones depicted in Figure 2.6. The specific heat capacity can be calculated through equation (2.11)

$$Cp(s) = Cp(st) \times \frac{Ds \times Wst}{Dst \times Ws} \tag{2.11}$$

where Cp(s) is the specific heat capacity of the specimen $(J.g^{-1}K^{-1})$, Cp(st) is the specific heat capacity of the sapphire standard $(J.g^{-1}K^{-1})$, Ds is the vertical distance between the curves of the empty pan and the curve of the unknown material at a specific temperature (mW), Dst is the vertical distance between the curves of the empty pan and the curve of the sapphire at a specific temperature (mW), Ws is the mass of specimen (mg), and Wst is the mass of sapphire standard (mg).
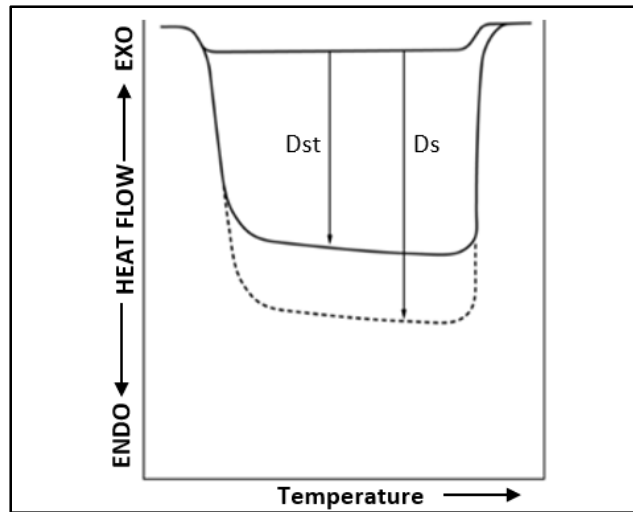
Figure 2.6 Heat flow
Adapted from ASTM standards E1269-11 (2018)

## 2.3 Results and Discussion

This section presents the BDS and DSC results separately. For each, the test configuration and results are explained. The outcomes are analyzed and compared to previous studies in the literature.

### 2.3.1 Broadband Spectroscopy (BDS)

The tests were conducted at a voltage of 3V over the range of $10^{-2}$ Hz to $10^5$ Hz. This range of frequency was precisely selected to test the interfacial polarization which is the principal type of polarization that is induced at the polymer-graphene interface. Figure 2.7 shows the curves of $\sigma'$ versus the frequency. At higher frequencies ($\geq 10^5$ Hz), all the samples possess approximately the same value of $\sigma'$ with a magnitude between $10^{-8}$ S/cm and $10^{-7}$ S/cm. Over the full frequency range, the samples with 0 wt. % and 3 wt. % exhibited almost identical electrical conductivity which increased with the frequency. At lower frequencies around $10^{-1}$ Hz to $10^{-2}$ Hz, the electrical conductivity of samples with 5 wt. % of graphene mildly increases up to $10^{-13}$ S/cm. On the other hand, the electrical conductivity of samples with 7 wt. % and 10 wt. % improved significantly, in comparison to neat epoxy, from $10^{-15}$ S/cm up to around $10^{-11}$

S/cm. Additionally, at these load percentages, there is the formation of a consistent plateau which implies that an electrical network is well established in the polymer (Panteny, Stevens, & Bowen, 2005).

Similar behavior was reported in the literature, where it has been reported that almost all the heterogeneous materials, including ferroelectric ceramic, polymer, and polymer composite (Furukawa, Yasuda, & Takahashi, 2004 ; James, Priya, Uchino, & Srinivas, 2001) frequently demonstrate similar frequency-dependent conductivity (Panteny et al., 2005). This trend is composed of two sections (Figure 2.9). At a lower frequency level, the electrical conductivity is independent from the frequency which is presented by a consistent plateau. At this range of frequency, the conductivity is direct current, and it is referred to as σDC. Beyond a certain frequency threshold, the type of the electrical conductivity shifts from direct current to alternative current σAC, rapidly increasing with the increase of the frequency following a certain power-law. Indeed, the electrical conductivity over the full range of frequency is given by the equation (2.12).

$$\sigma = \sigma_{DC} + \sigma_{AC} \tag{2.12}$$

Where

$$\sigma_{DC} = \sigma(0)$$
$$\sigma_{AC} = A.W^n$$

A is a constant, W is the angular frequency and n is constant between 0.6<n<1.
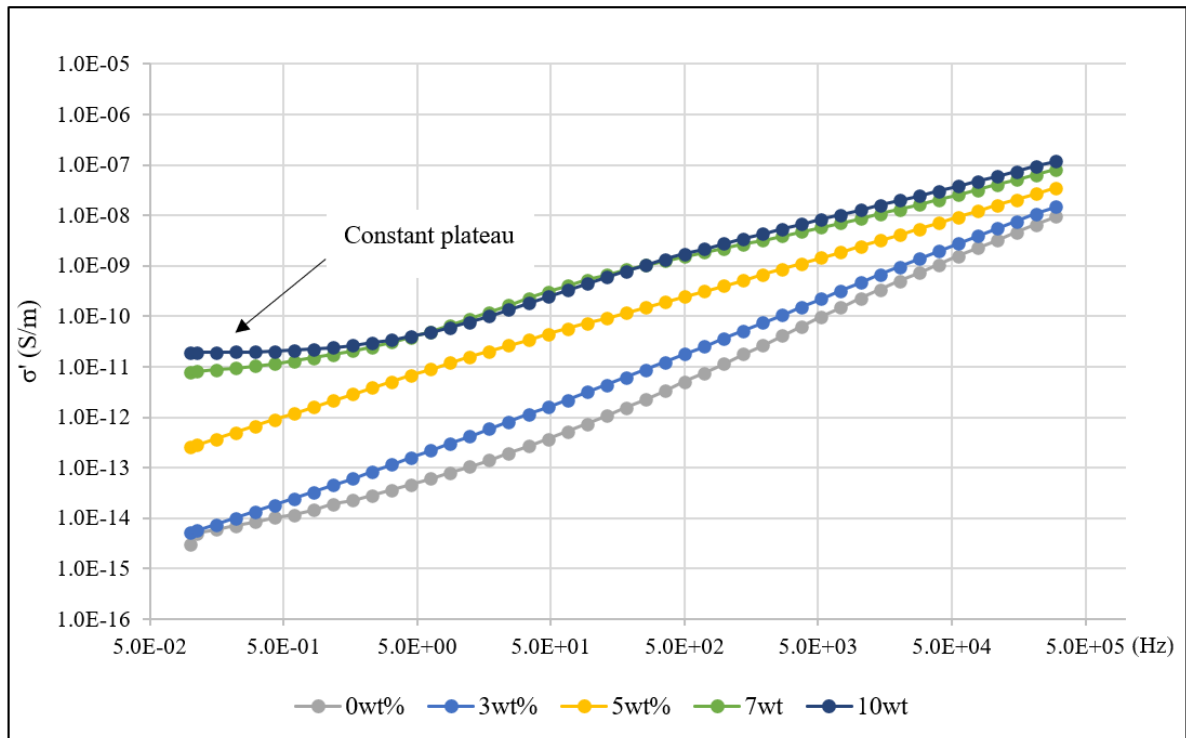
Figure 2.7 Conductivity versus frequency

This tendency is referred to as Jonscher's "Universal Dielectric Response" (UDR). Panteny et al. (2005) reported that the UDR is not compatible with conventional behavior and it can be explained by the "random resistor-capacitor" (R-C) network theory. In their study, the electrical properties of a polymer composite were simulated using an array of resistors and capacitors placed between nodes. This circuit simulates a microstructure that contains dielectric (capacitor) and conductive (resistor) materials, which for the purposes of this study correspond to the polymer matrix and the graphene, respectively. The frequency dependence threshold is a critical parameter in insulating polymer composite (Jin, Xia, & Gerhardt, 2016 ; K. Yang et al., 2013). It indicates whether the graphene particles are sufficiently distributed to create a conductive path throughout the polymer matrix (M. Hamidinejad, Zhao, Zandieh, et al., 2018).
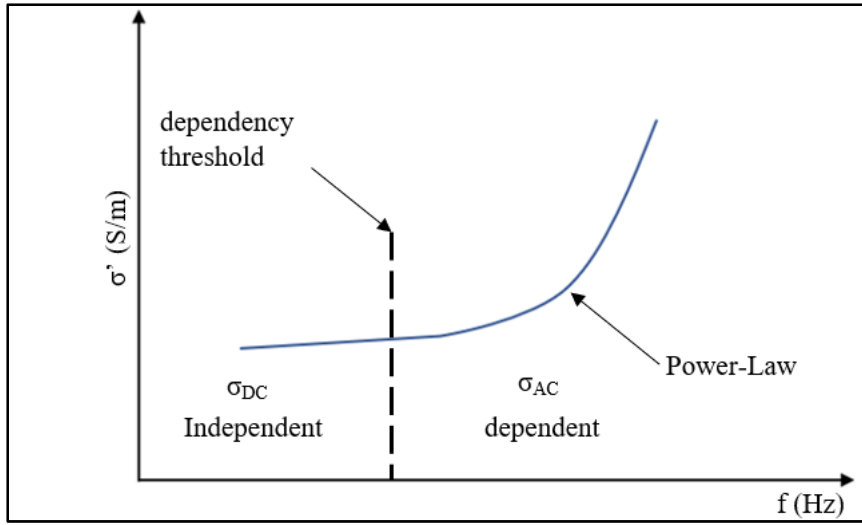
Figure 2.8 Universal Dielectric Response
Drawn based on Panteny et al. (2005)

Figure 2.9 presents the DC electrical conductivity versus the load fillers. These values are taken at the lowest frequency ($10^{-1}$~$10^{-2}$) (A. Ameli, Jung, & Park, 2013 ; A. Ameli, Nofar, Park, Pötschke, & Rizvi, 2014 ; Aboutaleb Ameli, Nofar, Wang, & Park, 2014 ; M. Hamidinejad, Zhao, Zandieh, et al., 2018). The electrical conductivity increased by approximately four orders of magnitude, from 3.1 $10^{-15}$ S/cm to 1.9 $10^{-11}$S/cm. The percolation threshold occurred at around 7 wt. %. The induced electrical conductivity ($\sigma_{DC}$) is relatively low compared to what has been reported in earlier studies. However, the differences can be explained by the changes of several key factors, such as the mixing method, the type of used polymer, and the sample preparation. As an example, in this study marine epoxy 820, which is thermoset polymer, was used, while other studies have used thermoplastic polymers such as high-density polyethylene (HDPE), polyurethane (TPU), and linear low-density polyethylene (LLDPE) (M. Hamidinejad, Zhao, Zandieh, et al., 2018 ; Lentzakis et al., 2017).

Moreover, comparisons between studies can be obscured by some sources of error. Despite using digital calipers for the measurement of the samples' dimensions, uncertainty in the thickness measurement or inconsistency in thickness across the sample surface can have a dominating impact on the results. In addition, the contact quality between the copper electrodes

and the sample has a potent impact on the results. The flatness of samples is imperfect, resulting in limited contact between the electrodes and the sample. Since the polymer composite materials are highly insulating, the low-quality contact is often the root cause of lower measured values and additional losses. This can be averted by coating the sample's surfaces with a thin golden layer. This improves the contact-quality and reduces the measurement errors (Serenari, 2019).
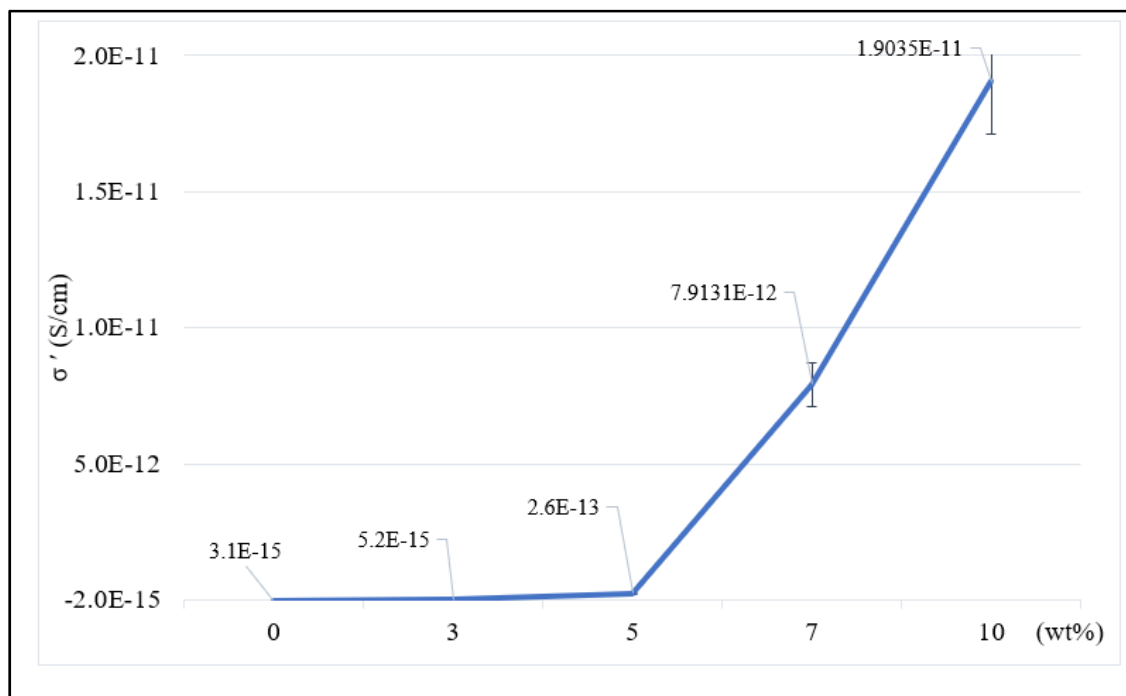


Figure 2.9 DC conductivity versus graphene weight percentage

## 2.3.2    Differential Scanning Calorimetry (DSC)

After calibration, a specific heating program with three different segments is used for the measurement. First, the temperature was held at 20 °C for 5 minutes, then it gradually increases at a constant rate of 10 °C/min until it reaches 200 °C. Finally, the temperature was held at 200 °C for 5 minutes. The data acquisition was made each 10 °C. The range of temperature investigated in this study was purposely selected because it coincides with the machining temperature of the CFRP (El-Hofy et al., 2011). This appropriately simulates the thermal

behavior of the epoxy matrix during the machining of the CFRP. Figure 2.10 depicts the behavior of the samples over the full range of temperature. Samples with different graphene filler levels roughly showed the same trend: a sharp increase until the glass transition temperatures, around 55 °C, followed by a mild decrease to a low of about 1.5 J/g°C and finally a slight increase to a maximum of 3 J/g°C. It is important to mention that a post curing was not performed before the DSC tests. However, several weeks last before the manufacturing of the plaques and those tests. Despite this curing time at room temperature, this may explain the low values of the glass transition temperature (Tg) of the modified epoxies. For instance, Wu (1992) investigated the impact of post curing temperature on the Tg of the epoxy. Showing that the Tg linearly increases with the increase of the post curing temperature up until it is fully cured. However, increasing the postcuring temperature beyond that point slightly reduces the Tg.
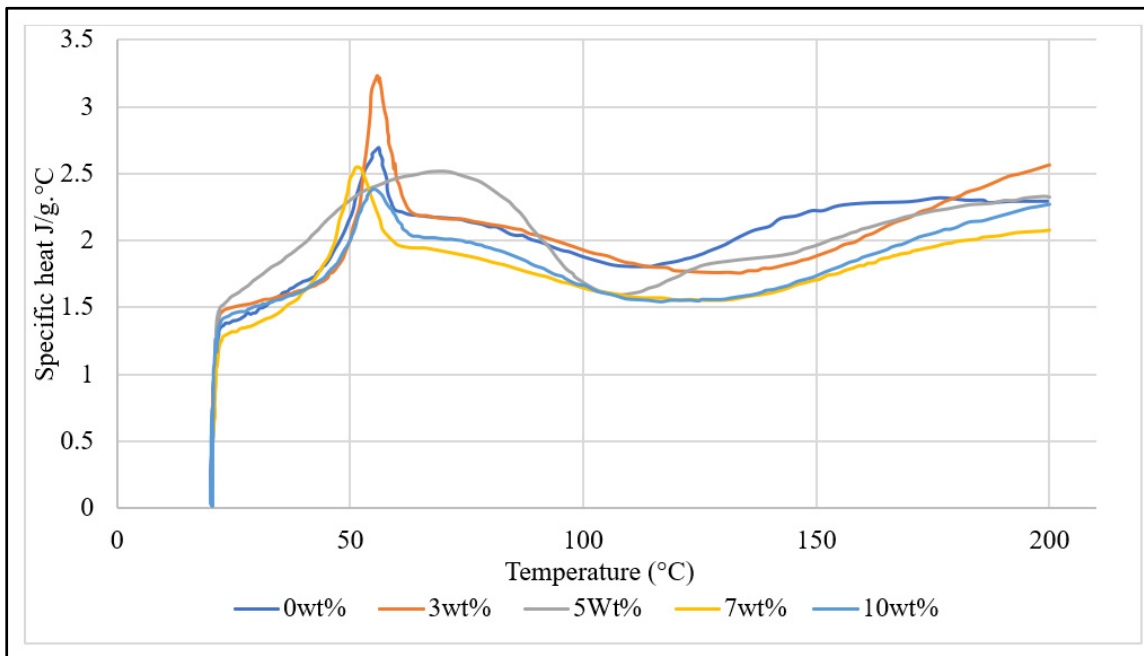
Figure 2.10 Specific heat versus temperature

Figure 2.11 shows a comparison of the specific heat values at the glass transition temperature (~ 55 °C). The graphene reduces the specific heat by approximately 16%. This variation can be observed between the specific heat of the pristine epoxy which equals to 2.64 J/g°C and

composite epoxy with 10 wt. % which possesses only 2.27 J/g°C. This is in agreement to an extent, with the anticipated results discussed in section «2.5 Specific Heat». High graphene loading reduces the specific heat and can be anticipated to increase the thermal conductivity. However, the samples with 3 wt. % of graphene present an exception to the trend. Despite the experiment being repeated in triplicate, the specific heat values were consistently higher than the values of the pristine epoxy. More experiments are required to understand this unexpected trend.
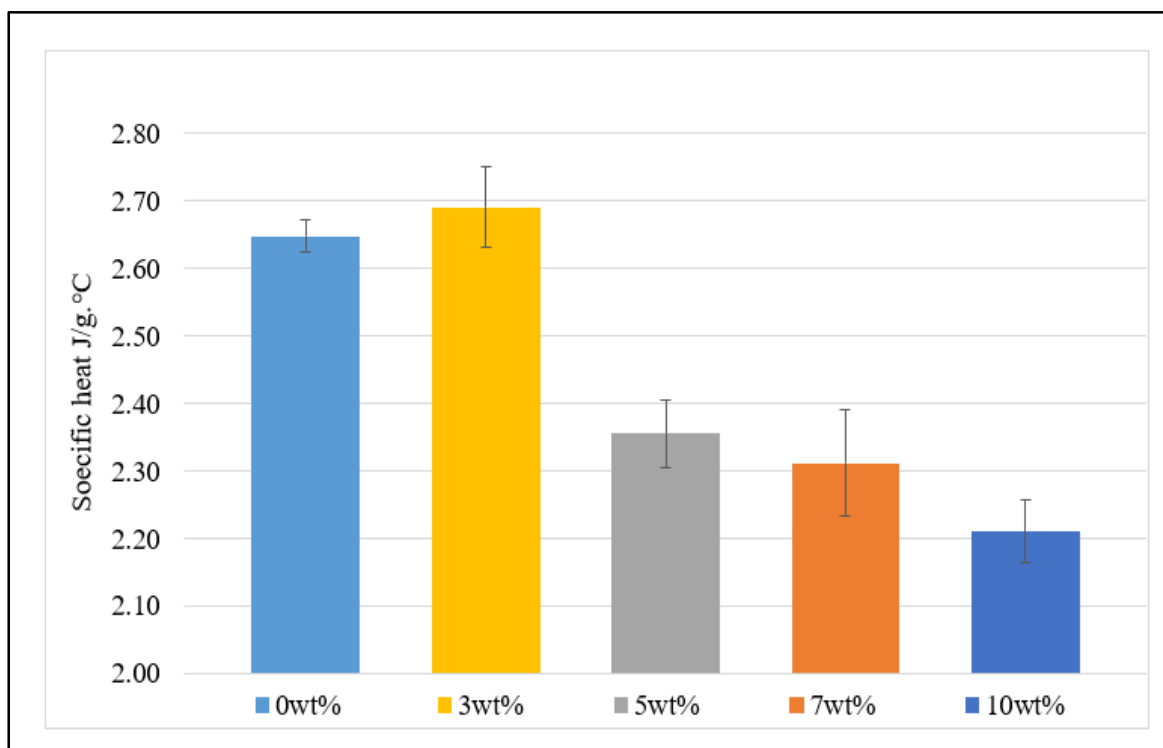


Figure 2.11 Specific heat versus load filler at ~55°C

Previous studies have used the specific heat capacity measurement to indirectly study thermal conductivity. Thermal conductivity and specific heat capacity are affected by the same material factors. In the context of polymer composites, these factors include filler properties such as particle shape, particle alignment, waviness magnitude, filler content, dispersion quality, and contact resistance at the matrix-filler interface (Chu, Li, & Dong, 2013 ; Teng et al., 2011 ; S.-Y. Yang et al., 2010). Xiang & Drzal (2011) compared the thermal conductivity of two thin

films made of graphene particles of different particle diameters: ~15 μm and ~1 μm. The larger diameter particles resulted in improved thermal conductivity by 60.8%. F. Wang, Drzal, Qin, & Huang (2015) reported a 115% enhancement of the thermal conductivity. This tremendous enhancement was explained by the low surface area of the graphene's particles which facilitates the exfoliation process, resulting in a uniform dispersion. In a polymer composite, these factors contribute to higher thermal dissipation. The principal factor of thermal conductivity in graphene-based polymer is the phonon diffusion and larger filler platelets improve the filler network for phonon diffusion (F. Wang et al., 2015). The differences between the results of this study and prior works also suggest that high shear mixing is not sufficient to exfoliate and disperse the graphene. Wang et al. (2015) exfoliated the graphene within the epoxy through a special sequence. The graphene was dispersed in acetone by ultrasonic sonication. Then, the epoxy was added under magnetic stirrer agitation and the mixture was passed through a three-roll mill to assure homogeneous and uniform dispersion. This processing method is not desirable for large-scale production because it involves a flammable solvent. More studies are needed to develop methods that combine feasibility for large volume production and mixture quality.

## 2.4    Conclusion

In this study, the impact of the graphene filler on the electrical and thermal properties of the graphene-based polymer was documented. Broadband spectroscopy (BDS) was employed to examine the electrical conductivity. The differential scanning calorimetry (DSC) was used to quantitively evaluate the specific heat capacity. This enabled a qualitative conclusion about the effect of graphene on the thermal conductivity. Epoxy composite samples were prepared with graphene percentages of 0, 3, 5, 7, and 10 wt. %. The percolation threshold was achieved at 7 wt. % of graphene. An enhancement of four orders of magnitude was recorded with 10 wt. % up to ~1.9 $10^{-11}$ S/cm. At low frequency, samples with 10 wt. % demonstrated a consistent plateau in conductivity which indicates a well-established electrical pathway. By DSC, the specific heat capacity was analyzed around the glass transition temperature of the epoxy (~ 55°C). The minimum recorded value was with 10 wt. % of graphene filler which counts as a

14% reduction in comparison to the neat epoxy. This suggests that samples with higher graphene filler possess higher thermal conductivity than of those without graphene. Further trials must be carried on to better understand the thermal behavior of the graphene-based polymer.

# CHAPTER 3

# EFFECT OF GRAPHENE ADDITIVE ON FLEXURAL AND INTERLAMINAR SHEAR STRENGTH PROPERTIES OF CARBON FIBER REINFORCED POLYMER COMPOSITE

Mohamed Ali Charfi [1], Ronan Mathieu [1], Jean-François Chatelain [1], Claudiane Ouellet-Plamondon[1], and Gilbert Lebrun [2]

[1] École de Technologie Supérieure, Montréal, Québec, H3C1K3, Canada.

[2] Université du Québec à Trois-Rivières (UQTR), Trois-Rivières, Canada.

## 3.1    Abstract

Composite materials are widely used in various manufacturing fields from aeronautic and aerospace industries to the automotive industry. This is due to their outstanding mechanical properties with respect to their light weight. However, some studies showed that the major flaws of these materials are located at the fiber/matrix interface. Therefore, enhancing matrix adhesion properties could significantly improve the overall material characteristics. This study aims to analyze the effect of graphene particles on the adhesion properties of carbon fiber-reinforced polymer (CFRP) through interlaminar shear strength (ILSS) and flexural testing. Seven modified epoxy resins were prepared with different graphene contents. The CFRP laminates were next manufactured using a method that guarantees a repeatable and consistent fiber volume fraction with a low porosity level. Short beam shear and flexural tests were performed to compare the effect of graphene on the mechanical properties of the different laminates. It was found that 0.25 wt. % of graphene filler enhanced the flexural strength by 5%, whilst the higher concentrations (2 and 3 wt. %) decreased the flexural strength by about 7%. Regarding the ILSS, samples with low concentrations (0.25 and 0.5 wt. %) demonstrated a decent increase. Meanwhile, 3 wt. % slightly decreases the ILSS.

**Keywords:** CFRP; composite; graphene; contact molding; mechanical properties

## 3.2      Introduction

Carbon fiber-reinforced polymer composites (CFRP) are increasingly being used in a wide range of domestic and industrial applications, such as aerospace, automobile, wind energy, sport, and goods industries to name a few (Othman, Ismail, Basri, Sharudin, & Hemdi, 2018 ; J. Z. Zhang, 2013). Owing to their advantageous properties like corrosion resistance, temperature resistance, lightweight, and high mechanical properties, more than 50% of new aircraft (Airbus A350 and Boeing 787) are composed of CFRP (Bouvet, 2017 ; Breuer, 2016). Their strength/weight and stiffness/weight ratios can be five to eight times greater than ordinary metals (Budynas & Nisbett, 2011). However, matrix/fiber interface is considered as the weakest link of composite materials (J. Shesan, C. Stephen, G. Chioma, Neerish, & E. Rotimi, 2019), with typical flaws such as voids and uncovered fibers. This would eventually initiate the failure of composite parts (X. Liu & Chen, 2016).

As a solution for interfacial weaknesses, researchers have sought to incorporate fillers in the matrix. These fillers have great potential to ameliorate the mechanical, chemical, and physical properties of the polymer. Therefore, enhancing the matrix bonding properties should improve the overall composite quality (Pathak, Borah, Gupta, Yokozeki, & Dhakate, 2016 ; Qin, Vautard, Drzal, & Yu, 2015). Graphene is one of the most promising filler in polymers. Since its first discovery in 2004 (2004) (Novoselov, 2004), this material has gained enormous attention (Kim, Abdala, & Macosko, 2010b ; Stankovich, Dikin, et al., 2006b). It possesses exceptional characteristics like high thermal and electrical conductivity (Balandin et al., 2008 ; Lee, Wei, Kysar, & Hone, 2008), lightweight, as well as  astonishing mechanical properties (Stoller, Park, Zhu, An, & Ruoff, 2008 ; W. Yang et al., 2018). Graphene is usually obtained through the exfoliation of graphite. However, its manufacturing is cost prohibitive and presents safety risks in large scale production  (Nazarpour & Waite, 2016). Graphene materials are good fillers for polymer matrices, with nano-clay and carbon nanotubes being the most relevant competitors. Both graphene and nano-clay are platelet-type materials, characterized by a layered structure with high aspect ratios (>1000) (Chen et al., 2001 ; Giannelis, 1996). Composite polymers based on platelet fillers demonstrated outstanding mechanical properties.

However, graphene outperforms nano-clay by its excellent thermal and electrical properties. In contrast, carbon nanotubes possess similar thermal and electrical properties to graphene. However, they are not considered as suitable fillers because of their relatively expensive, high mixture viscosity causing the entangling of nanotubes, and immense anisotropic properties (Sandler et al., 2004). Another comparative study (Rafiee et al., 2009) was performed between graphene nano-platelets (GnPs), single-walled carbon nanotubes (SWCNT), and multi-walled carbon nanotubes (MWCNT). The Young's modulus of the graphene nanocomposite is 31% higher than that of the pristine epoxy as opposed to only 3% enhancement for the SWCNT. Moreover, the tensile strength of the graphene nanocomposite is 26% higher than that based on MWCNT (Rafiee et al., 2009). This renders graphene nanoplatelets the ideal filler for our experiments. Homogeneous dispersion, graphene exfoliation, and load percentage play a vital role in the composite quality. For instance, while flexural stress and short beam shear stress tend to peak at lower graphene percentage, electrical and thermal conductivity significantly increase at higher filler percentages. Moreover, dispersion and exfoliation processes have an undeniable impact on the composite quality (Al Imran, 2016).

Han et al.(2017) studied the impact of graphene oxide (GO) concentration on the interlaminar shear strength (ILSS) of CFRP laminates. From 0 wt. % to 0.1 wt. %, the ILSS increases but beyond 0.2 wt. %, the ILSS was inversely proportional to the GO content. Indeed, a maximum improvement of more than 8% was recorded at 0.1 wt. % compared to the same composite without graphene. The same tendency was observed by (Kamar et al., 2015), which used glass fabric composites with GnPs particles. The optimum graphene concentration was 0.25 wt. % which induced 29% and 25% of improvement in flexural strength and mode I fracture toughness, respectively. Increasing the concentration to more than 0.5 wt. % considerably reduces the fracture toughness and decreases the interlaminar adhesion which in turn leads to delamination and micro buckling.

L.-C. Tang et al. (2013) investigated the influence of graphene dispersion in epoxy. They prepared two graphene/epoxy mixtures with 0.2 wt. % by means of the ball-mill-mixing technique. The graphene particles were better dispersed in one mixture than the other. As a

result, highly dispersed graphene induces higher strength and fracture toughness. The fracture improvement was 52% for the highly dispersed mixture as opposed to only 24% for the poorly dispersed mixture. A similar study conducted by Raza et al. (2012) concludes that graphene dispersed by mechanical mixing produces better thermal and electrical conductivity than those prepared by dual asymmetric centrifuge speed mixer. This trend is attributed to the intensive shearing of mechanical mixing. Chandrasekaran, Seidel, & Schulte (2013) compared the electrical properties of two different processing methods: High shear mixing plus three-roll-milling method (3RM) against high shear mixing plus sonication method, emphasizing that samples prepared by 3RM have a higher electrical conductivity than those prepared by sonication.

The fiber volume fraction variation (Vf) and porosity contents are crucial factors to drive a clear conclusion of this study. The composite properties are dominated by the fiber properties and not by the matrix (i.e., young modulus, flexural strength, etc.) (Mclaughlin, 2013). Thereby, any trivial variation of the fiber volume fraction would conceal the impact of graphene. Similarly, the void ratio negatively affects the properties. For example, interlaminar shear strength decreases by about 7% per 1% of void content (Mayr et al., 2011). Therefore, all samples must have the same Vf with a minimum of variation as well as low and consistent porosity.

 To the best of the authors' knowledge, most of the manufactured laminates presented by previous studies possess either a relatively large $V_f$ variation or a non-uniform filler dispersion which might affect the repeatability of their results. For example, in (Chowdhury, Hosur, & Jeelani, 2006 ; El-Ghaoui, Chatelain, Ouellet-Plamondon, & Mathieu, 2019 ; Kamar et al., 2015), the authors incorporated different types of particles into the laminate by means of vacuum resin transfer molding (VARTM). Even though this technique might lead to a consistent fiber volume fraction, it may lead to non-uniform dispersion of the filler particles because of a "filtering" mechanism of the filler by the fibers all along the resin transfer. (Mclaughlin, 2013) used hand-layup and vacuum bagging with weight control of the fibers and

the epoxy. Nevertheless, the fiber volume fraction was not found repeatable from one laminate to another.

For these reasons, the first objective of this study is to propose an innovative and reliable manufacturing method, at a reasonable cost for experiment purposes, that leads to clear conclusions about the effect of graphene on the mechanical properties. It is important to note that this study is a part of a larger scientific study, with the main goal of improving the machinability of CFRP. This material is inherently rough and abrasive which makes its machinability more difficult than other materials. Tool wear and poor surface finish frequently occur in this matter (El-Ghaoui et al., 2019). So, enhancing the machinability of CFRP is a necessity. However, we still have to improve or, at least maintain, the mechanical properties of the modified material as compared to the unfilled resin composite. We also investigate the optimum filler percentage that induces the best short beam shear (SBS) and flexural strengths. The results found of this study are the starting point to find the best filler percentage that improves the machinability of CFRP.

## 3.3 Materials and Methods

In this section, we present the samples preparation in four principle paragraphs: the graphene/epoxy mixing process, the CFRP laminate manufacturing method, composite quality verification, and the mechanical tests. Concerning the quality verification, this was carried out by analyzing the fiber volume fraction and the porosity content. The mechanical properties were evaluated through SBS and flexural tests. Both SBS and flexural coupons possess a rectangular shape. However, SBS is smaller than the flexural coupon, with a length and a width of only 18 and 8 mm, respectively.

### 3.3.1 Graphene-Epoxy Mixing Process

Graphene particles (0XB) were provided by by Nano-Xplore Inc. (Saint-Laurent, QC, Canada). These particles were mixed and exfoliated within a Marine 820 epoxy resin from Axson

Technologies (Madison Heights, MI, USA). The filler percentages varied from 0 wt. % to 3 wt. % as presented in Table 3.1.

Table 3.1 Graphene's percentages

| Test number | Graphene (wt. %) |
|---|---|
| 1 | 0 |
| 2 | 0,25 |
| 3 | 0,5 |
| 4 | 0,75 |
| 5 | 1 |
| 6 | 2 |
| 7 | 3 |

Filler percentages were calculated with respect to the total weight of the mixture which includes: hardener weight, epoxy weight, and filler weight percentage. According to the epoxy supplier, the ratio hardener over epoxy should be equal to 0,18. The different weight percentages of the mixtures were calculated according to the equations (2.1)-(2.4). Based on previous studies, (Chandrasekaran et al., 2013 ; Raza et al., 2012) we used three-roll milling (3RM) and high-shear mixing to incorporate and homogenize graphene particles in the epoxy. Next, a Silverson L5M-A (Silverson Machines, Inc., East Longmeadow, MA, USA) high-shear mixer was used to mechanically blend the filled epoxy. The intensive shear force deeply exfoliates the graphene particles which considerably reduces the flakes' thickness. As shown in Table 3.2, the mechanical mixing was divided into seven segments, during which the temperature was almost maintained with the help of an ice bath. However, the ice bath was removed in the last step to allow the temperature to rise to a maximum of 50 °C. The elevated temperature decreased the mixture viscosity, facilitating air bubble extraction (El-Ghaoui et al., 2019).

Table 3.2 Shear mixing sequence

| | |
|---|---|
| 2 minutes | 1000RPM |
| 2minutes | 3500RPM |
| 2 minutes | 6000RPM |
| 2minutes | 8000 RPM |
| 2x3 minutes | 1000RPM |

Final degassing was done in a vacuum oven for one hour, and the loaded epoxy was finally mixed with the hardener according to the supplier's instructions.

## 3.3.2    Laminate Manufacturing

The following constraints are imposed on the manufacturing method in this study: homogeneous distribution of graphene, consistent laminate thickness, minimum void, and minimum fluctuation of the fiber orientation. Even though there are multiple processing methods, most of them are either expensive or difficult to operate and unadjustable to meet the above-mentioned requirements, especially the one requiring a homogeneous distribution of filler particles. In this context, contact molding was the only alternative to liquid injection molding processes for this scientific application. Since the operator impregnates the fiber layer by layer with the filled epoxy, the graphene particles are evenly dispersed on the surface of each layer as well as across the laminate thickness. Nonetheless, the basic contact molding process usually produces important void contents, stochastic fiber angle fluctuation, and uncontrollable thickness variations. The void ratio can be reduced by applying a vacuum during the cure of the plate to remove most of the trapped air from the laminate (Mehdikhani, Gorbatikh, Verpoest, & Lomov, 2019). In terms of angle fluctuations of the fiber, three wooden sticks with several grooves were fixed on top of the mold (Figure 3.1). These sticks form a frame that prevents the fibers layers from slipping during the hand-layup and the curing processes. These grooves allow the excess of epoxy to be expelled without displacing the wooden sticks.

Figure 3.1 Guide frame wooden stick

A uniform laminate thickness was obtained using four spacers having the same thickness. These spacers were placed on the mold, distant from the wooden frame by approximately 10 mm each side. Using this technique improved the hand lay-up process and made it adequate for this study. Figure 3.2 presents a 3D sketch of the developed method.
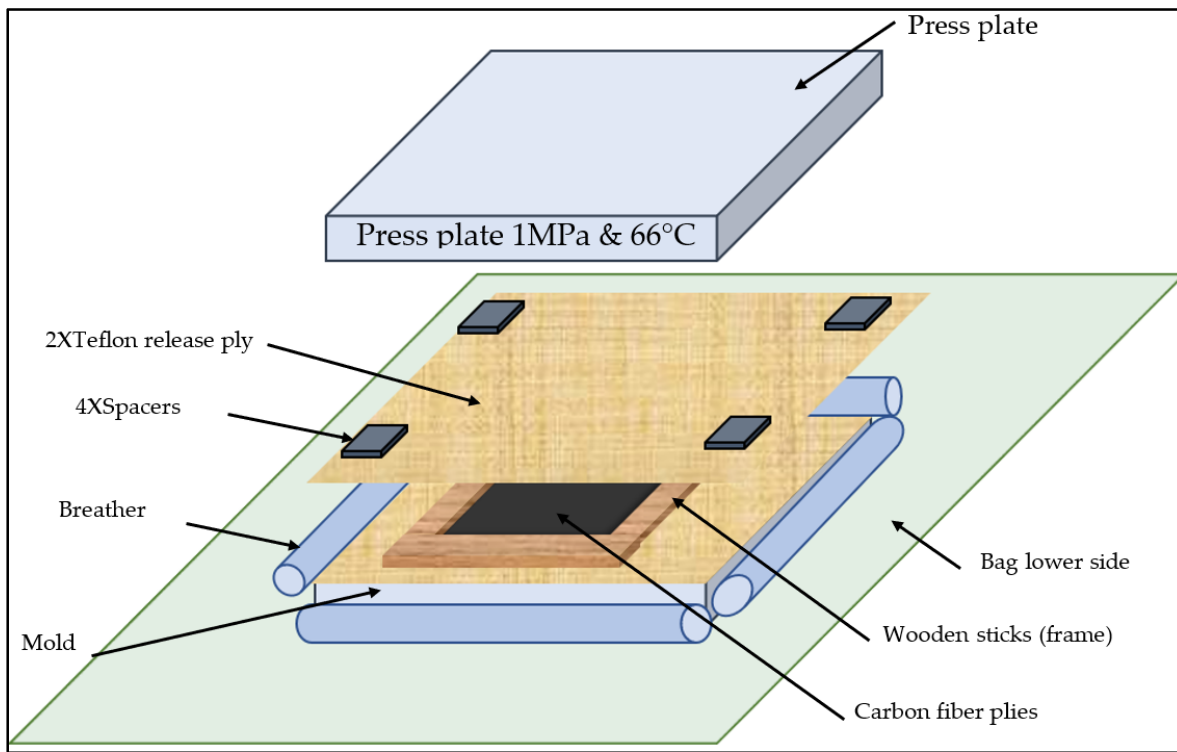


Figure 3.2 Exploded view of the lay-up assembly

Fourteen plies of TC-09-U unidirectional high modulus carbon fiber from Texonic Inc. (SaintJean-sur-Richelieu, QC, Canada) were used to form $[0]_{14}$ laminates with a thickness of around 4 mm. The single layer reinforcement surface density is 320 g/m2 . In terms of curing parameters, the vacuum pressure was set at a maximum of 29 inch of mercury, the hydraulic

press was equipped with heater plates which allow to cure the laminate according to the supplier recommendation, at 66 °C for 3 hours and under a pressure of 1 MPa to have a consistent thickness. Figure 3.3 shows a typical photograph of the developed method. As for the demolding part, we used Teflon sheet instead of release agent and peel ply. Indeed, the release agent was not effective under such curing conditions. In addition, peel ply randomly absorbs a certain quantity of epoxy which affects the fiber volume fraction. Conversely, the Teflon sheet is quite efficient during the demolding and its intrinsic sealant nature guarantees a smooth surface on both sides of the plaque.
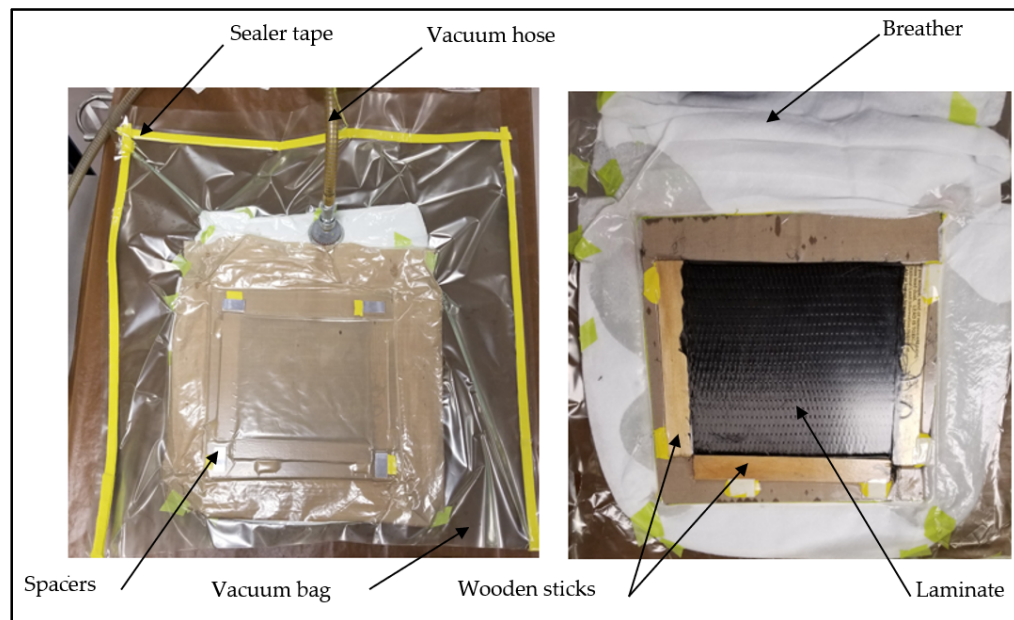


Figure 3.3 Contact molding assisted with vacuum bag and hot press

A post-curing was required to uniformize curing through the thickness of the laminates. Therefore, all the plates were put inside a Despatch oven (Ontario Ovens Inc., Brampton, ON, Canada) which was programed to gradually increase the temperature with a segment ramp of 10 °C per hour until it reaches a maximum of 66 °C. The temperature was held constant for 24 h. Eventually, it gradually decreases with a negative slope of 10 °C per hour until reaching room temperature. Verification of the laminate quality was performed through measurement of the fiber volume fraction ($V_f$) and void ratio. To avoid oxidation of carbon fibers using a

high temperature of pyrolysis when measuring $V_f$ (Dean, McDonough, Dunkers, Flynn, & Hunston, 2004 ; National Research Council (U.S.), 1995) it was instead calculated by measuring the laminate thickness and implementing it into equation (3.1).

$$Vf = \frac{Mf \times N}{\varphi \times h} \qquad (3.1)$$

Here, Mf is the surface density of dry reinforcement (g/m²); N is the number of plies; φ is the fiber density (g/m³), and h is the laminate thickness (m). Unlike resin burn off technique, this method does not reveal the emptiness ratio. Therefore, a porosity test was required. The micrographic image processing is deemed to be a good approach to evaluate the porosity level in the laminates. Kite et al. (2008) emphasized that the outcomes of this method correlates well with matrix digestion. Thus, 6 samples of each plaque were cut and prepared to be polished by a motopol 2000 automatic polisher. Next, an optical microscope was used to take a sufficient number of pictures of the whole sample's area with a magnification of 50X (Figure 3.4). Finally, an open-source software named ImageJ was used to segment this image into three zones, the background, the composite, and voids. This step is done through machine learning, where the operator manually introduces all of these different sections to the software. Doing so, the software can determine the percentages of zones of the entire image.
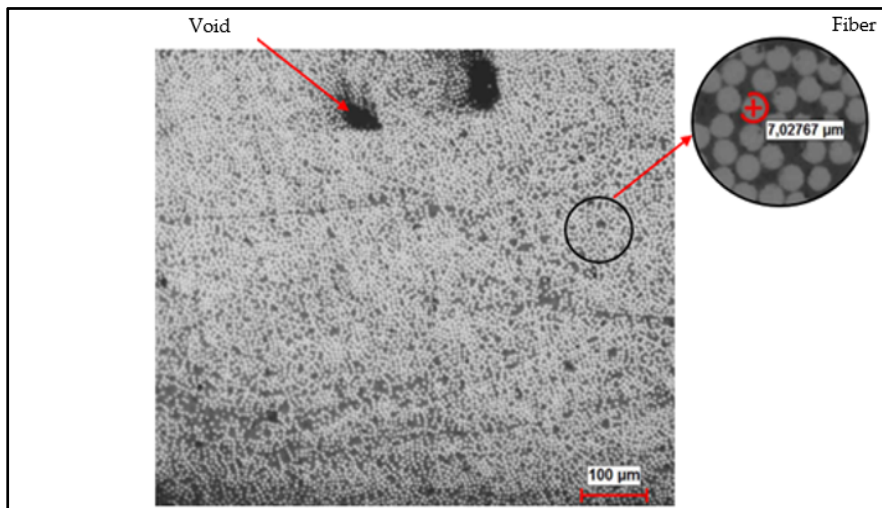


Figure 3.4 Microscopic picture X50

### 3.3.3    Mechanical Test

The purpose of the short beam shear test is to investigate the matrix adhesion quality. This test is similar to the flexural test. However, the length of the short beam's coupon is short compared to the flexural coupon. Thus, the vertical force induces a shear stress in the plane of specimens. The ASTM D2344 standard requires precise geometrical and dimensional tolerances of the coupon. In order to respect these constraints, a high-precision cutting machine (Struers Secotom 50, Struers, Mississauga, ON, Canada) with a diamond saw was used. To guarantee representative results, ten coupons from each laminate with 0° fiber orientation were tested. The interlaminar shear strength (ILSS) tests were performed on a universal testing machine (MTS alliance RF/200, MTS systems corporation, Eden prairies, MN, USA) which was equipped with a 10 kN load cell. The crosshead speed was set at 1 mm/min and the interlaminar shear strength was calculated according to this equation.

$$ILSS = 0.75 \times \frac{Fmax}{A} \tag{3.2}$$

where ILSS is the interlaminar shear strength (N/mm²); Fmax the maximum force (N) and A the surface area of coupon (mm²)

Ten flexural samples were prepared according to ASTM D7264. Same as the short beam shear sample, the fiber orientation was kept at 0° and the crosshead speed of 1 mm/min was maintained until the first drop load occurred which indicates the breakage point. Based on the standard recommendations, the strain points of 0.001 and 0.003 were used to calculate the chord modulus of elasticity. Moreover, the ultimate flexural strength and chord modulus of elasticity were determined by implementing the maximum applied forces in equations (3.3) and (3.4):

$$\sigma_F = \frac{3 \times Fmax \times L}{2 \times b \times h^2} \tag{3.3}$$

$$E_F = \frac{\Delta\sigma}{\Delta\varepsilon} \qquad\qquad (3.4)$$

where Fmax is the maximum force (N); L is the specimen length (mm); h is the specimen thickness (mm); b is the specimen width (mm) and ε is the strain (mm/mm).

## 3.4 Results and Discussion

### 3.4.1 Fiber Volume Fraction

The developed manufacturing method induces repeatable results. Consistent fiber volume fraction is a must to distinguish between the effect of thickness variations and the effect of graphene particles. A digital micrometer was used to take four measurements of each laminate, and these values were then averaged and used in equation (5) to calculate the fiber volume fraction. The $V_f$ mean value, between laminates, equals 64% ± 0.41%. This trivial variation can be ascribed to variation in the Teflon sheet thickness, the spacers thickness, and the mold surface flatness. Nonetheless, this variation is still acceptable, and its impact can be averted through a statistical normalization around the average value of $V_f$. In the porosity analysis, the software ImageJ results in a "classifier" file, and this file is a template that contains data through which we can classify similar microscopic pictures. Subsequently, these pictures are converted into a binary image with black and white colors (Figure 3.5). White pixels with color under a certain threshold will be counted as voids; others with color above the threshold will be counted as composites. The software will then calculate the void percentage, which is the white area divided by the total area.
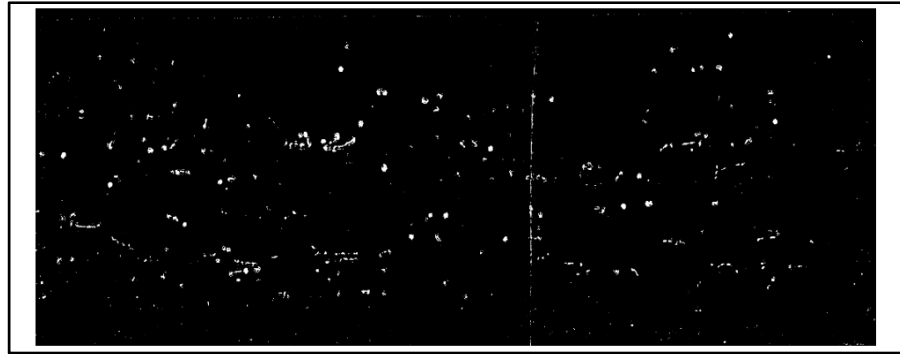
Figure 3.5 Binary microscopic image

Figure 3.6 presents the void percentage of the composites versus the percentage of filler. As can be seen, the results are almost constant with a slight variation. The average value of porosity is equal to 0.61% with the smallest value of 0.4% and a maximum of 0.86%. The results are relatively good compared to the common standards. For instance, in aerospace applications, aircraft parts with a porosity level between 2.5% and 5% are usually accepted (Kastner, Plank, Salaberger, & Sekelja, 2010). Nevertheless, Costa et al. (Costa, Almeida, & Rezende, 2001) emphasized in their review that the interlaminar shear strength can be significantly affected if the porosity content goes beyond 0.9%. In addition, Hakim et al. (Hakim, Donaldson, Meyendorf, & Browning, 2017) highlighted that higher porosity levels make the composite part sensitive to water penetration and environmental factors which detrimentally impact the static and fatigue strength. The minimum void percentage that we found can be attributed to the high vacuum pressure applied during the curing process. Hakim et al.(Hakim et al., 2017) evaluated the impact of vacuum pressure on the porosity level. They examined three levels of vacuum pressure: poor (0 mmHg), medium (330 mmHg), and high (686 mmHg) and concluded that poor vacuum pressure induces 3.43% of porosity versus only 1.43% with high vacuum pressure. Furthermore, larger pores were more discernable with low vacuum pressure than with high vacuum pressure. According to the bar chart (Figure 3.6), the void percentage decreases as the filler percentages increase. For instance, laminates with 0 wt. % have 0.86% of void, whereas laminates with 3 wt. % have only 0.4% of void. Typically, increasing the load percentage would increase the matrix viscosity which hinders the extraction of the air bubbles and thus increases the porosity level. Consequently, the depicted pattern in

the bar chart does not corroborate with the mentioned hypothesis. Indeed, this trend can be assigned to the detection accuracy of the software Image J. After a sheer number of iterations, the software gained the aptitude to identify various parts of the micrographic image with higher precision. Therefore, the depicted values of the void with 3 wt. % are calculated with relatively more accuracy than the ones of 0 wt. %. Nonetheless, all the presented values are less than 1% which is considered as the threshold for a good composite quality.



Figure 3.6 Fiber volume fraction and void of the composite

## 3.4.2    Mechanical Test

A statistical study was required to detect and eliminate the outliers from the list of coupon results. These filtered results were then normalized using equation (3.9) to a $V_f = 64\%$ (Technomic Publishing Company, 1999).
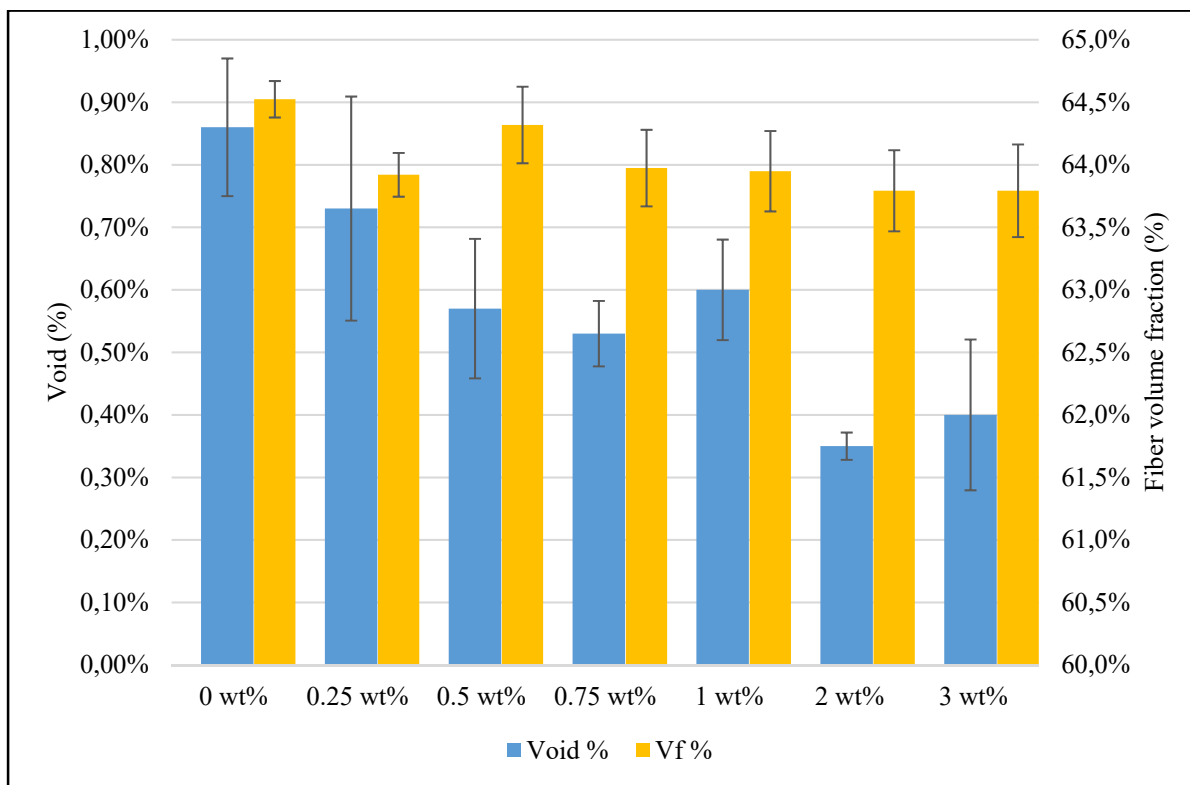
$$\text{Normalized value} = (test\ value\ x\ 0.64)/(sample's\ Vf) \qquad (3.9)$$

A Pearson correlation test was performed on the normalized values versus the fiber volume fraction ($V_f$) variation. This test was done under a significance level of 5%. The null hypothesis states that there is no significant correlation between the mechanical properties outcomes versus the $V_f$ variation. Most of the results did not reveal any significant correlation, therefore we can conclude that these results solely present the impact of the filler percentages. All flexural tests behaved linearly until the first drop of the load. This point was used to calculate the flexural strength for each sample. Figure 7 shows that the ultimate flexural strength of specimens with 0.25 wt. % improved by 5% compared to the pristine composite. It is important to mention that the fiber volume fraction of coupons with 0.25 wt. % is only 63.9% as opposed to 64.5% for plain coupons, which indicates that the 5% enhancement of flexural strength is purely assigned to the effect of the filler. On the other hand, the other laminates with a filler concentration higher than 0.25 wt. % demonstrated a slight decrease. The worst cases were with 2 and 3 wt. % with a drop of approximately 7% of the strength. A similar pattern was found by Kamar et al. (Kamar et al., 2015), where they specified 1 wt. % as a threshold of the graphene percentage. Beyond this point, the filler particles start to agglomerate into relatively big bundles which weaken the interlaminar adhesion, thus leading to delamination and micro-buckling defects.

The stiffness of samples was calculated through equation (8). Figure 3.7 presents the recorded results. No improvement was found by increasing the filler percentage. In contrast, the stiffness of the loaded specimens mildly decreased to a minimum of 125.7 GPa for the coupons with 0.5 wt. % as compared to a maximum of 131.4 GPa for the neat coupons. Both the stiffness and the ultimate shear strength of samples with 0.5 wt. % and higher filler contents are observed to decrease. This cannot be explained by the fiber volume fraction variation but rather by the effect of the graphene content, as can be seen by comparing the stiffness of samples with 0.25 wt. % and samples with 0.5 wt. % of graphene content. The latter has a slightly higher fiber volume fraction and yet exhibits lower stiffness. In the case of the 0.25 wt. % concentration, the ultimate strength of this specimen showed a certain enhancement, but the

stiffness is reduced. This does not meet the anticipated outcomes. For example, Hung et al. (Hung, Lau, Qiao, Fox, & Hameed, 2019) investigated the impact of graphene oxide on the mechanical properties of CFRP, reporting an enhancement of around 18% and 5% in the flexural strength and the stiffness, respectively. Nonetheless, in the case of 0.25 wt. %, the Pearson correlation test demonstrated a vivid relation between the stiffness and the $V_f$ variations (Figure 3.8). This was corroborated with previous studies (Mclaughlin, 2013 ; Qin et al., 2015), highlighting that flexural and tensile specimens with 0° fiber orientation are not sensitive to the matrix adhesion quality but rather to the fiber volume fraction and the fiber mechanical properties. Therefore, this trend can be assigned to the impact of $V_f$ variation from one sample to another and not to the graphene percentage.
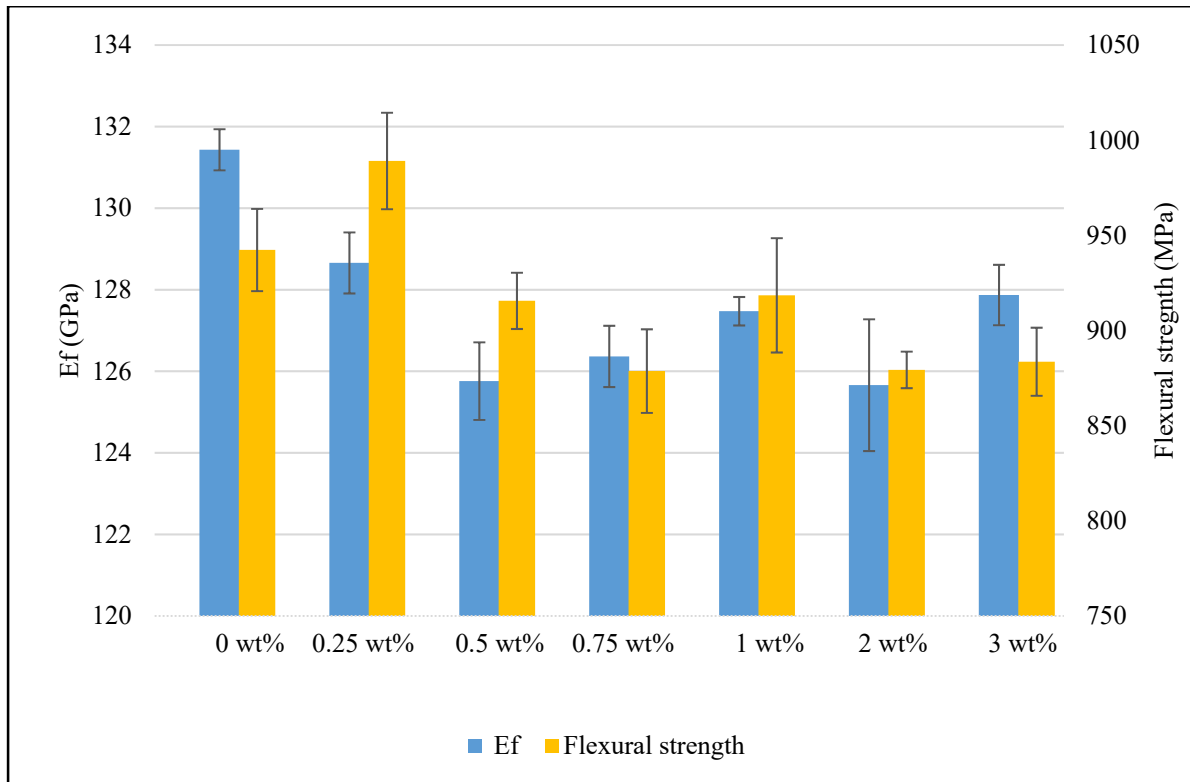


Figure 3.7 Stiffness and flexural strength of the composite
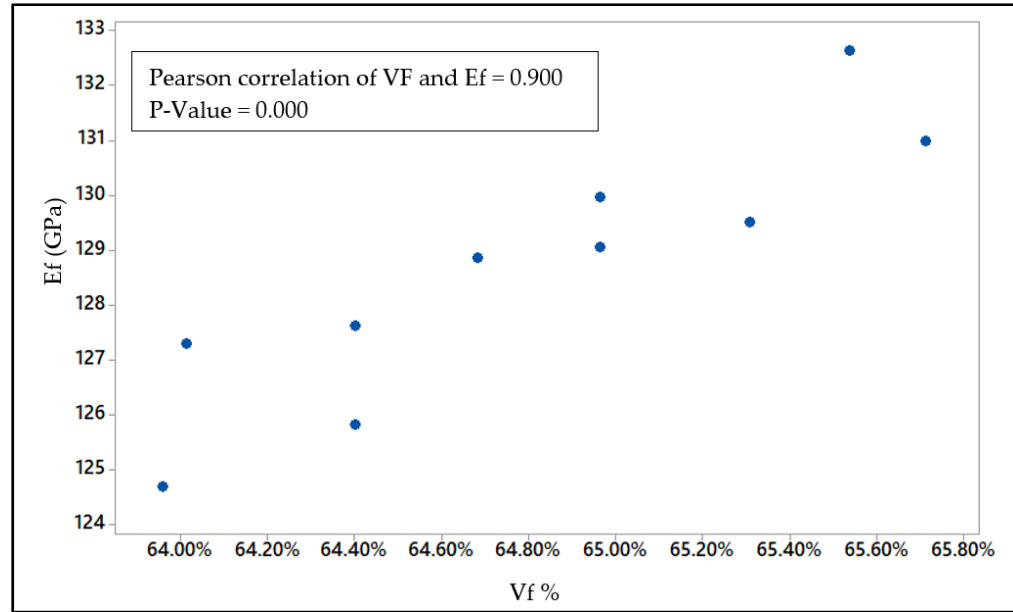
Figure 3.8 Scatter plot stiffness versus $V_f$ variations

Figure 3.9 displays the mean values of the interlaminar shear strength (ILSS) of each filler percentage. Samples with 0.25 wt. % and 0.5 wt. % showed a decent increase ranging from 56 MPa to approximately 59 MPa. The fiber content of the 0.25 wt. % coupons is less than the fiber content of plain coupons. Nonetheless, the recorded improvement counts as 5% in comparison to neat composite. Meanwhile, 0.75 wt. % of graphene concentration merely increased the ILSS by about 2%. However, the ILSS of all the specimens decreased with a minimum of 52 MPa in the case of 3 wt. %. The behavior of ILSS largely depends on the graphene content, in case of low (0 wt. % to 0.5 wt. %), the ILSS behaves linearly with a positive slope. Beyond 0.75 wt. %, this linear relation appears to be inversely proportional. A similar trend was revealed by (Han et al., 2017), though their tested graphene range was smaller, going from 0.1wt. % to 0.4wt. %.

For further clarification, we have presented the relative details and figures of the previous diagrams in Table 3.3.
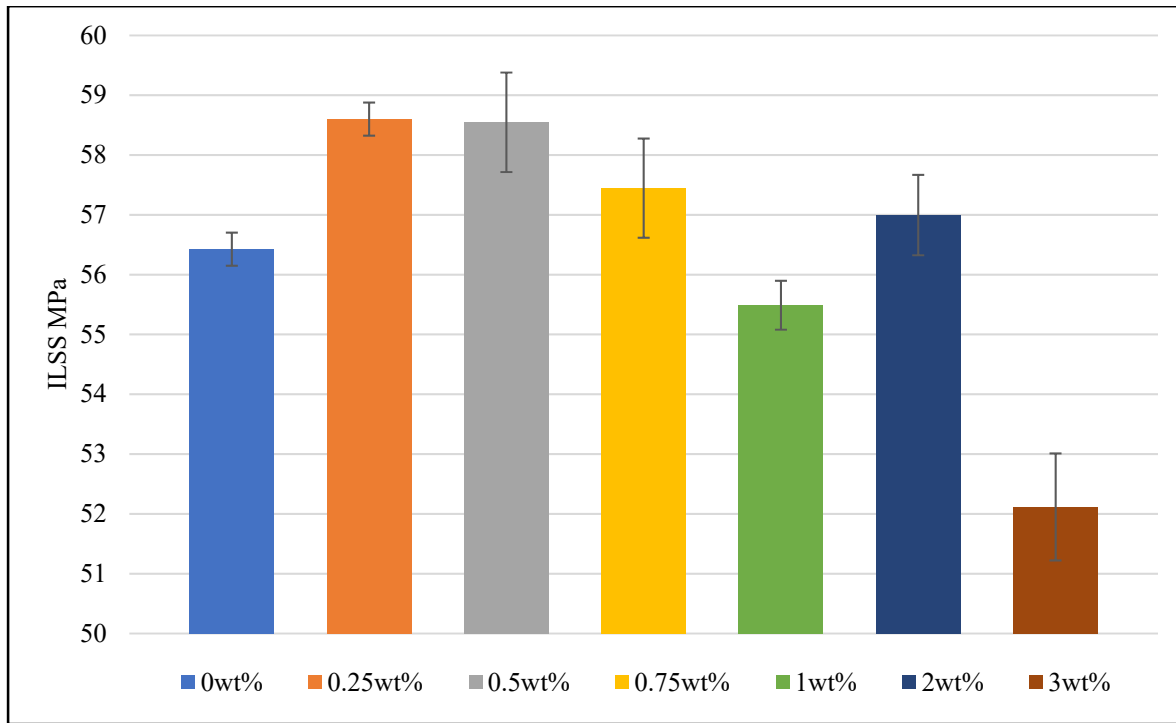
Figure 3.9 Interlaminar Shear Strength of the composites

Table 3.3 Figures recapitulation

| GnPs wt. % | Vf % | Void% | Flexural strength (MPa) | Stiffness (GPa) | ILSS (MPa) |
|---|---|---|---|---|---|
| 0 | 64.5 | 0.86 | 942.3 | 131.4 | 56.4 |
| 0.25 | 63.9 | 0.73 | 989.1 | 128.6 | 58.6 |
| 0.50 | 64.3 | 0.57 | 915.6 | 125.7 | 58.5 |
| 0.75 | 63.7 | 0.53 | 878.7 | 126.3 | 57.4 |
| 1.00 | 63.9 | 0.60 | 918.5 | 127.4 | 55.5 |
| 2.00 | 63.8 | 0.29 | 879.3 | 125.6 | 57 |
| 3.00 | 63.8 | 0.40 | 883.6 | 127.8 | 52.1 |

## 3.5      Conclusions

In this study, seven laminates of CFRP were manufactured by hand lay-up assisted with vacuum bagging and hydraulic press, these laminates contain different GnPs percentage ranged from 0 wt. % to 3 wt. %. The methodology process was described and has been approved as repeatable with a low porosity and $V_f$ variation. The manufactured laminates possess a consistent fiber volume fraction with an average value of 64%. The micrographic porosity test

revealed an acceptable void content with a mean of 0.61%. Hence, the fiber volume fraction and the porosity level have a little influence on the mechanical properties. Ten flexural samples and ten short beam samples were cut from each laminate, this was done according to the ASTM standards. The outcomes presented in this study lead to the following conclusion:

- The best graphene percentage was 0.25wt. %; samples with this filler content induced 5% improvement of the ILSS.
- It appears that 0.5wt. % presents a threshold of the graphene filler, more than this value, the particles will coalesce which in turn results in a poor graphene dispersion and therefore the mechanical properties will be negatively affected.
- The same trend was observed regarding the flexural test. Samples with 0.25wt. % filler showed a maximum improvement of 5%. It was expected that the chord modulus of elasticity would reveal the same trend as the flexural strength. However, it seems that the stiffness is more prone to the fiber volume fraction content. Pearson correlation test showed that the stiffness and the $V_f$ variation using this filler concentration are linearly proportional. Hence, it is difficult to conclude regarding this aspect.

For future studies, we should test other graphene percentages between 0 wt. % and 0.25 wt. %. Additionally, further tests should be carried on with 90° fiber orientation which might be more effective to evaluate the adhesion quality of the filled epoxy.

**Conflicts of Interest:** The authors declare no conflict of interest.

# CONCLUSION

The objective of the presented study is to evaluate the impact of graphene filler on the mechanical/thermal properties of the CFRP composite material. At the inception of the study, several manufacturing methods were tested like the VARTM, infusion, and hand lay-up. All of these manufacturing methods induced either a bad graphene dispersion or a high variation of the fiber volume fraction (Vf). Therefore, we have developed another method that involves the hand lay-up, vacuum bagging, and hydraulic press. This approach yields a consistent fiber volume fraction with an average variation of $\pm0.42\%$ and less than 1% of porosity level with an average variation of $\pm0.06\%$. A Consistent Vf and a minimum porosity level are vital points to drive a clear conclusion about the impact of graphene concentration. In this context, seven graphene concentrations, ranged from 0 wt. % to 3 wt. %, were mixed through three-roll milling and high shear mixing. These modified graphene-based epoxies were then used to manufacture the CFRP laminates. According to the ASTM standards, flexural and short beam samples were cut from these laminates. In terms of the resuls, the best graphene concentration was 0.25 wt. % which induced 5% of enhancement in both flexural strength and interlaminar shear strength (ILSS). More than 0.5 wt. % of graphene load seems to deteriorate the mechanical properties, this fact was corroborated with previous studies. Beyond the threshold of 0.5 wt. %, graphene particles tend to agglomerate and therefore affecting the dispersion across the surface and the thickness of the laminate.

The electrical and thermal properties of the graphene-based epoxy were assessed. Broadband spectroscopy (BDS) was employed to evaluate the volumetric electrical properties. This test was conducted under the interfacial polarization frequency ($10^{-2}$ Hz to $10^{5}$ Hz). The graphene concentrations were relatively higher than those of the mechanical properties, ranging from 0 wt. % to 10 wt. %. The overall electrical conductivity was improved by four-folds, going from ~3.1 $10^{-15}$ S/cm up to ~1.9 $10^{-11}$ S/cm with pristine and 10 wt. % loaded epoxies, respectively. The percolation threshold was found with only 7 wt. % of graphene filler. At lower frequency, the electrical conductivity of samples with 10 wt. % showed a consistent plateau which implies a well-established electric pathway. The differential scanning calorimetry test (DSC) was done

on the samples of the BDS. The DSC test leads to a quantitative evaluation of the specific heat capacity (Cp). As the specific heat capacity goes up, the thermal conductivity goes down and vice versa. Therefore, we can qualitatively conclude whether the thermal conductivity improved or not. Samples with 10 wt. % of graphene filler reduces the specific heat capacity by about 16%. This reduction implies a certain enhancement of the thermal conductivity.

# RECOMMENDATION

During the course of this project, we have encountered several hurdles that prevent us from pushing the project even further. In this section, we highly recommend pursuing the following points in order to exploit the full capacity of the graphene particles.

- we should use 3RM machine equipped with a digital screen and sensors that allow us to precisely specify the distance between the apron roll and the feed roll. Thus, we can adjust the dispersion accordingly.

- The mechanical tests like the flexural, short beam, and tensile tests should be conducted at 90° of the fiber orientations. It is easier to evaluate the impact of the modified epoxy at 90° fiber orientations than at 0°.

- We should find an alternative to prepare bone shape samples from the graphene-based epoxy without air bubbles so we can assess the mechanical properties of the modified epoxy before assessing the CFRP mechanical properties.

- It would be more interesting if we can quantitively evaluate the impact of the graphene on the thermal properties of the epoxy. The thermal conductivity can be readily calculated through multiplying the thermal diffusivity, the specific heat capacity, and the density of the sample. We already have the specific heat capacity of the modified samples. Therefore, we merely need to evaluate the diffusivity of the same samples.

# ANNEX I

## MICROGRAPHIC POROSITY PROCESSING

This approach composes of two main sections, the first one is about polishing the samples and take sufficient microscopic pictures that covers the entire surface of the sample. The second part is to introduce this micrographic picture into the software Image J and calculating the void percentage. Therefore, we will explain the methodology of these sections separately.

- **Sample preparation**

Samples were taken randomly from each laminate, the sample size is not important, we have taken a rectangular shape with a size of around 1x3cm. To facilitate the polishing process, we have put the sample inside a cylindrical plastic mold, and we filled the mold with epoxy (Figure-A I-1). Thus, the sample is part of a cylindrical structure that can be readily mounted onto the polisher machine.
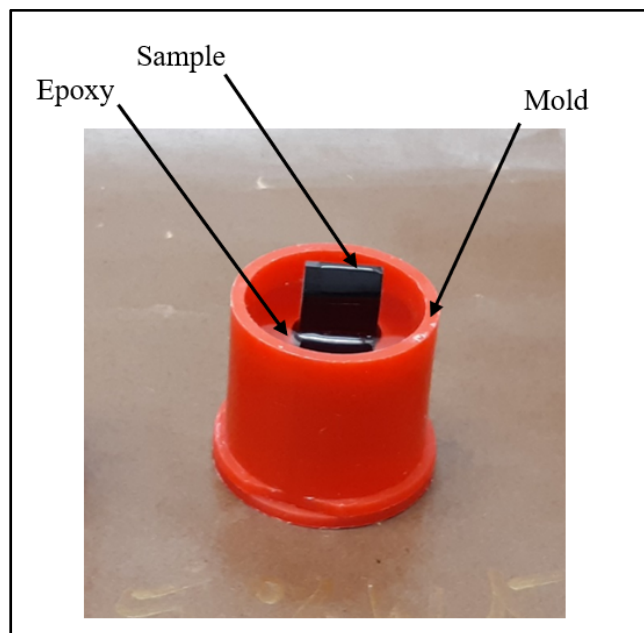


Figure-A I-1 Molding the porosity sample

The polishing processing is a vital key point, low polishing quality leaves multiple scratches on the sample surface which makes it even harder for the software to differentiate scratches from the void. After a sheer number of trials, we have found a great polishing sequence that we highly recommend for the future studies. Table-A I-1 presents the polishing sequence. It is important to mention that we change the sandpaper at the end of each segment even if we are not moving to the next grain size. For example, for the grain size 250, we should use one sandpaper for 2 minutes, and then change another one for the next two minutes. There is a general trend in this sequence. For the same grain size, the duration of the first segment is relatively longer than the ones at the end. Take for instance the 800 sandpaper, the first segment lasts one minute whereas the last segment lasts only 20 seconds. The purpose of the first segment is to erase the scratches induced by the previous sandpaper. However, polishing with the same sandpaper for a longer period takes off some grains from the sandpaper which leaves thinner scratches. Thus, to evert this problem, we deliberately reduce the time of the last segments.

Table-A I-1 Polishing sequence

| Sandpaper grains size | Number of steps | Duration |
|---|---|---|
| 250 | 3 | 2 minutes |
| 320 | 2 | 1 minutes |
| 320 | 4 | 40 seconds |
| 400 | 3 | 1 minutes |
| 400 | 4 | 40 seconds |
| 600 | 2 | 1 minutes |
| 600 | 4 | 40 seconds |
| 600 | 4 | 20 seconds |
| 800 | 1 | 1 minutes |
| 800 | 4 | 40 seconds |
| 800 | 4 | 20 seconds |
| 1200 | 1 | 1 minutes |
| 1200 | 5 | 40 seconds |
| 1200 | 5 | 20 seconds |
| 1200 | 3 | 10 seconds |

As for the polisher machine, we have chosen the following parameters:

- o Spindle force: 20N
- o Sandpaper rotational speed: 250 RPM with opposite direction of the spindle.

- **Micrographic processing**

After polishing the sample, we have taken micrographic pictures with 50X magnification. Usually, it takes around 35 pictures to cover the entire sample surface. To Rebuild the original image of the sample, we have used the "auto-align" feature in photoshop. The required steps are described as the following:

- New document (Ctrl + N)
    - o Resolution 120 pixels/inch
    - o Color mode: Grayscale; 8 bits
- Drag and drop all the pictures into the new file
- Select all the layers (left click on the first layer, hold on MAJ, and left click on the last layer)
- Right click → Rasterized layers
- Align the layers
    - o Edition → Auto-algin layers → Projection: reposition
- Select all the layers as previously → right click→ merge layers
- It is recommended to reduce the image size by 50% (Alt + Ctrl + I)
- Select the composite area using rectangular marquee tool as shown in figure
- Right click → Layer via copy
- Select the new layer → Image → Trim → Top left pixel color → ok
- Save image under the extension JPEG with high quality.
    - o It is recommended to not surpass a picture size of 2.5 MB, otherwise it would take longer processing time.

After recreating the original micrographic image of the sample, we can move forward to compute the void percentage. Even though there are several approaches to reach the same goal, we find this method as the best one for our application.

- Drag and drop the auto-aligned picture onto Image J software

- Select Plugins → segmentation→ Trainable Weka Segmentation

- Under the new panel select setting → for the training feature select

    o Gaussian blur, Mean, and difference of gaussians

    o Name the class one as composite and class two as void

- Use the sketch tools in the main panel to highlight the shape and size of the void as well as of the composite.

- Click on train classifier

- Repeat the latter step until the software recognizes the different areas of the picture (void from composite)

- Save classifier→ file→ Save as→ 'file title.model'

- Save data→ file → Save as →'file title.tarff'

For other pictures, we can use the saved classifier and data:

    o Drag new picture into the main panel of the software

    o Plugins→ Segmentation → Trainable Weka Segmentation

    o Load Classifier (here you should introduce the saved file under the extension. model)

    o Load data

    o Train classifier

- Now the software is ready to analyze the picture pixels:

    o Click on create results

    o Image → type: 8-bits

    o Image → adjust→ threshold→ apply

    o Analyze→ analyze particles

# LIST OF BIBLIOGRAPHICAL REFERENCES

Abbasi, S., Carreau, P. J., & Derdouri, A. (2010). Flow induced orientation of multiwalled carbon nanotubes in polycarbonate nanocomposites: Rheology, conductivity and mechanical properties. *Polymer*, *51*(4), 922-935. https://doi.org/10.1016/j.polymer.2009.12.041

Al Imran, K. (2016). *Enhancement of Electrical Conductivity of Carbon/Epoxy Composites by Graphene and Assessment of Thermal and Mechanical Properties*. North Carolina A&T State University, North Carolina USA.

Al-Shurman, K. M., & Naseem, H. (2014). CVD Graphene Growth Mechanism on Nickel Thin Films, 7.

Ameli, A., Jung, P. U., & Park, C. B. (2013). Electrical properties and electromagnetic interference shielding effectiveness of polypropylene/carbon fiber composite foams. *Carbon*, *60*, 379-391. https://doi.org/10.1016/j.carbon.2013.04.050

Ameli, A., Nofar, M., Park, C. B., Pötschke, P., & Rizvi, G. (2014). Polypropylene/carbon nanotube nano/microcellular structures with high dielectric permittivity, low dielectric loss, and low percolation threshold. *Carbon*, *71*, 206-217. https://doi.org/10.1016/j.carbon.2014.01.031

Ameli, Aboutaleb, Nofar, M., Wang, S., & Park, C. B. (2014) Lightweight Polypropylene/Stainless-Steel Fiber Composite Foams with Low Percolation for Efficient Electromagnetic Interference Shielding. *ACS Applied Materials & Interfaces*, *6*(14), 11091-11100. https://doi.org/10.1021/am500445g

Balandin, A. A. (2011). Thermal properties of graphene and nanostructured carbon materials. *Nature Materials*, *10*(8), 569-581. https://doi.org/10.1038/nmat3064

Balandin, A. A., Ghosh, S., Bao, W., Calizo, I., Teweldebrhan, D., Miao, F., & Lau, C. N. (2008). Superior Thermal Conductivity of Single-Layer Graphene. *Nano Letters*, *8*(3), 902-907. https://doi.org/10.1021/nl0731872

Behabtu, N., Lomeda, J. R., Green, M. J., Higginbotham, A. L., Sinitskii, A., Kosynkin, D. V., Pasquali, M. (2010). Spontaneous high-concentration dispersions and liquid crystals of graphene. *Nature Nanotechnology*, *5*(6), 406-411. https://doi.org/10.1038/nnano.2010.86

Bibi, S., Bremner, D. H., Macdougall-Heasman, M., Reid, R., Simpson, K., Tough, A. Matthews, K. H. (2015). A preliminary investigation to group disparate batches of licit

and illicit diazepam tablets using differential scanning calorimetry. *Analytical Methods*, *7*(20), 8597-8604. https://doi.org/10.1039/C5AY01711D

Bonaccorso, F., & Sun, Z. (2014). Solution processing of graphene, topological insulators and other 2d crystals for ultrafast photonics. *Optical Materials Express*, *4*(1), 63. https://doi.org/10.1364/OME.4.000063

Bonanni, A., & Pumera, M. (2011). Graphene Platform for Hairpin-DNA-Based Impedimetric Genosensing. *ACS Nano*, *5*(3), 2356-2361. https://doi.org/10.1021/nn200091p

Bourlinos, A. B., Georgakilas, V., Zboril, R., Steriotis, T. A., & Stubos, A. K. (2009). Liquid-Phase Exfoliation of Graphite Towards Solubilized Graphenes. *Small*, *5*(16), 1841-1845. https://doi.org/10.1002/smll.200900242

Bouvet, C. (2017). *Mechanics of aeronautical composite materials*. Hoboken, NJ : ISTE Ltd/John Wiley and Sons Inc. Repéré à https://books.google.ca/books?hl=fr&lr=&id=ykozDwAAQBAJ&oi=fnd&pg=PP2&dq=Bouvet,+C.+Mechanics+of+Aeronautical+Composite+Materials%3B+Wiley:+Hoboken,+NJ,+USA,+2017.&ots=Bg_mN_im2h&sig=elJ1I4y6eylYwHM0Ajrf5J_X7MQ#v=onepage&q&f=true

Bracamonte, M. V., Lacconi, G. I., Urreta, S. E., & Foa Torres, L. E. F. (2014). On the Nature of Defects in Liquid-Phase Exfoliated Graphene. *The Journal of Physical Chemistry C*, *118*(28), 15455-15459. https://doi.org/10.1021/jp501930a

Breuer, U. P. (2016). *Commercial Aircraft Composite Technology*. Cham : Springer International Publishing. https://doi.org/10.1007/978-3-319-31918-6

Budynas, R. G., & Nisbett, J. K. (2011). *Shigley's mechanical engineering design* (9th ed). New York : McGraw-Hill.

Campbell, F. C. (2010a). *Structural composite materials*. Materials Park, Ohio : ASM International. Repéré à https://books.google.ca/books?hl=en&lr=&id=D3Wta8e07t0C&oi=fnd&pg=PR1&dq=campbell+Structural+composite+materials.+Materials+Park,+Ohio:+ASM+International&ots=T-1ecwX6x8&sig=f5nF-ollEn5SDau4J3fKqBq8qAQ#v=onepage&q&f=true

Campbell, F. C. (2010b). *Structural composite materials*. Materials Park, Ohio : ASM International.

Campbell, F. C. (Éd.). (2012). *Lightweight materials: understanding the basics*. Materials Park, Ohio : ASM International. Repéré à https://books.google.ca/books?id=WgplzgxfhCIC&printsec=frontcover&dq=campbell+Structural+composite+materials.+Materials+Park,+Ohio:+ASM+International+chapter+5&hl=en&sa=X&ved=0ahUKEwid1Oyc993oAhXhQ98KHUdXC88Q6AEIMDAB#v=onepage&q&f=true

Chandrasekaran, S., Seidel, C., & Schulte, K. (2013). Preparation and characterization of graphite nano-platelet (GNP)/epoxy nano-composite: Mechanical, electrical and thermal properties. *European Polymer Journal*, *49*(12), 3878-3888. https://doi.org/10.1016/j.eurpolymj.2013.10.008

Chen, G.-H., Wu, D.-J., Weng, W.-G., & Yan, W.-L. (2001). Preparation of polymer/graphite conducting nanocomposite by intercalation polymerization. *Journal of Applied Polymer Science*, *82*(10), 2506-2513. https://doi.org/10.1002/app.2101

Choi, W., Lahiri, I., Seelaboyina, R., & Kang, Y. S. (2010). Synthesis of Graphene and Its Applications: A Review. *Critical Reviews in Solid State and Materials Sciences*, *35*(1), 52-71. https://doi.org/10.1080/10408430903505036

Chowdhury, F. H., Hosur, M. V., & Jeelani, S. (2006). Studies on the flexural and thermomechanical properties of woven carbon/nanoclay-epoxy laminates. *Materials Science and Engineering: A*, *421*(1-2), 298-306. https://doi.org/10.1016/j.msea.2006.01.074

Chu, K., Li, W., & Dong, H. (2013). Role of graphene waviness on the thermal conductivity of graphene composites. *Applied Physics A*, *111*(1), 221-225. https://doi.org/10.1007/s00339-012-7497-y

Costa, M. L., Almeida, S. F. M. de, & Rezende, M. C. (2001). The influence of porosity on the interlaminar shear strength of carbon/epoxy and carbon/bismaleimide fabric laminates. *Composites Science and Technology*, *61*(14), 2101-2108. https://doi.org/10.1016/S0266-3538(01)00157-9

Cui, W., Du, F., Zhao, J., Zhang, W., Yang, Y., Xie, X., & Mai, Y.-W. (2011). Improving thermal conductivity while retaining high electrical resistivity of epoxy composites by incorporating silica-coated multi-walled carbon nanotubes. *Carbon*, *49*(2), 495-500. https://doi.org/10.1016/j.carbon.2010.09.047

Daniel, I. M., Wooh, S. C., & Komsky, I. (1992). Quantitative porosity characterization of composite materials by means of ultrasonic attenuation measurements. *Journal of Nondestructive Evaluation*, *11*(1), 1-8. https://doi.org/10.1007/BF00566012

Dean, S., McDonough, W., Dunkers, J., Flynn, K., & Hunston, D. (2004). A Test Method to Determine the Fiber and Void Contents of Carbon/Glass Hybrid Composites. *Journal of ASTM International*, *1*(3), 12076. https://doi.org/10.1520/JAI12076

Di, C., Wei, D., Yu, G., Liu, Y., Guo, Y., & Zhu, D. (2008). Patterned Graphene as Source/Drain Electrodes for Bottom-Contact Organic Field-Effect Transistors. *Advanced Materials*, *20*(17), 3289-3293. https://doi.org/10.1002/adma.200800150

E37 Committee. (2018). *Test Method for Determining Specific Heat Capacity by Differential Scanning Calorimetry*. ASTM International. https://doi.org/10.1520/E1269-11R18

El-Ghaoui, Chatelain, Ouellet-Plamondon, & Mathieu. (2019). Effects of Nano Organoclay and Wax on the Machining Temperature and Mechanical Properties of Carbon Fiber Reinforced Plastics (CFRP). *Journal of Composites Science*, *3*(3), 85. https://doi.org/10.3390/jcs3030085

El-Hofy, M. H., Soo, S. L., Aspinwall, D. K., Sim, W. M., Pearson, D., & Harden, P. (2011). Factors Affecting Workpiece Surface Integrity in Slotting of CFRP. *Procedia Engineering*, *19*, 94-99. https://doi.org/10.1016/j.proeng.2011.11.085

Elmar, W., Thomas, K., & Michael, K. (2014). *Composite market report 2014*. (S.l.) : (s.n.).

Fredin, L. A., Li, Z., Lanagan, M. T., Ratner, M. A., & Marks, T. J. (2013). Sustainable High Capacitance at High Frequencies: Metallic Aluminum–Polypropylene Nanocomposites. *ACS Nano*, *7*(1), 396-407. https://doi.org/10.1021/nn3044148

Furukawa, T., Yasuda, K., & Takahashi, Y. (2004). Dielectric and conductive spectra of the composite of barium titanate and LiClO/sub 4/ -doped polyethylene oxide. *IEEE Transactions on Dielectrics and Electrical Insulation*, *11*(1), 65-71. https://doi.org/10.1109/TDEI.2004.1266318

Giannelis, E. P. (1996). Polymer Layered Silicate Nanocomposites. *Advanced Materials*, *8*(1), 29-35. https://doi.org/10.1002/adma.19960080104

Gojny, F. H., Wichmann, M. H. G., Köpke, U., Fiedler, B., & Schulte, K. (2004). Carbon nanotube-reinforced epoxy-composites: enhanced stiffness and fracture toughness at low nanotube content. *Composites Science and Technology*, *64*(15), 2363-2371. https://doi.org/10.1016/j.compscitech.2004.04.002

Hakim, I. A., Donaldson, S. L., Meyendorf, N. G., & Browning, C. E. (2017). Porosity Effects on Interlaminar Fracture Behavior in Carbon Fiber-Reinforced Polymer Composites. *Materials Sciences and Applications*, *08*(02), 170-187. https://doi.org/10.4236/msa.2017.82011

Hamidinejad, M., Zhao, B., Chu, R. K. M., Moghimian, N., Naguib, H. E., Filleter, T., & Park, C. B. (2018). Ultralight Microcellular Polymer–Graphene Nanoplatelet Foams with Enhanced Dielectric Performance. *ACS Applied Materials & Interfaces*, *10*(23), 19987-19998. https://doi.org/10.1021/acsami.8b03777

Hamidinejad, M., Zhao, B., Zandieh, A., Moghimian, N., Filleter, T., & Park, C. B. (2018). Enhanced Electrical and Electromagnetic Interference Shielding Properties of Polymer–Graphene Nanoplatelet Composites Fabricated via Supercritical-Fluid

Treatment and Physical Foaming. *ACS Applied Materials & Interfaces*, *10*(36), 30752-30761. https://doi.org/10.1021/acsami.8b10745

Hamidinejad, S. (2019). *Thermal and Electrical Properties of Graphene-Based Polymer Nanocomposite Foams*. University of Toronto, Toronto Canada.

Han, X., Zhao, Y., Sun, J., Li, Y., Zhang, J., & Hao, Y. (2017). Effect of graphene oxide addition on the interlaminar shear property of carbon fiber-reinforced epoxy composites. *New Carbon Materials*, *32*(1), 48-55. https://doi.org/10.1016/S1872-5805(17)60107-0

Heid, T. (2015). *Innovative nanostructured epoxy composites for enhanced high voltage insulation systems*. UNIVERSITÉ DU QUÉBEC, ÉCOLE DE TECHNOLOGIE SUPÉRIEURE. Repéré à https://espace.etsmtl.ca/id/eprint/1553/

Hernandez, Y., Nicolosi, V., Lotya, M., Blighe, F. M., Sun, Z., De, S., Coleman, J. N. (2008). High-yield production of graphene by liquid-phase exfoliation of graphite. *Nature Nanotechnology*, *3*(9), 563-568. https://doi.org/10.1038/nnano.2008.215

Holmes, M. (2014). Global carbon fibre market remains on upward trend. *Reinforced Plastics*, *58*(6), 38-45. https://doi.org/10.1016/S0034-3617(14)70251-6

Hossain, M. K., Chowdhury, Md. M. R., Imran, K. A., Salam, M. B., Tauhid, A., Hosur, M., & Jeelani, S. (2014). Effect of low velocity impact responses on durability of conventional and nanophased CFRP composites exposed to seawater. *Polymer Degradation and Stability*, *99*, 180-189. https://doi.org/10.1016/j.polymdegradstab.2013.11.008

Hsu, D. K., & Uhl, K. M. (1987). A Morphological Study of Porosity Defects in Graphite-Epoxy Composites. Dans D. O. Thompson & D. E. Chimenti (Éds), *Review of Progress in Quantitative Nondestructive Evaluation* (pp. 1175-1184). Boston, MA : Springer US. https://doi.org/10.1007/978-1-4613-1893-4_134

Huang, X., Iizuka, T., Jiang, P., Ohki, Y., & Tanaka, T. (2012). Role of Interface on the Thermal Conductivity of Highly Filled Dielectric Epoxy/AlN Composites. *The Journal of Physical Chemistry C*, *116*(25), 13629-13639. https://doi.org/10.1021/jp3026545

Hung, P., Lau, K., Qiao, K., Fox, B., & Hameed, N. (2019). Property enhancement of CFRP composites with different graphene oxide employment methods at a cryogenic temperature. *Composites Part A: Applied Science and Manufacturing*, *120*, 56-63. https://doi.org/10.1016/j.compositesa.2019.02.012

Hyun, W. J., Park, O. O., & Chin, B. D. (2013). Foldable Graphene Electronic Circuits Based on Paper Substrates. *Advanced Materials*, *25*(34), 4729-4734. https://doi.org/10.1002/adma.201302063

J. Shesan, O., C. Stephen, A., G. Chioma, A., Neerish, R., & E. Rotimi, S. (2019). Fiber-Matrix Relationship for Composites Preparation. Dans A. B. Pereira & F. A. O. Fernandes (Éds), *Renewable and Sustainable Composites*. (S.l.) : IntechOpen. https://doi.org/10.5772/intechopen.84753

James, A. R., Priya, S., Uchino, K., & Srinivas, K. (2001). Dielectric spectroscopy of Pb(Mg1/3Nb2/3)O3-PbTiO3 single crystals. *Journal of Applied Physics*, *90*(7), 3504-3508. https://doi.org/10.1063/1.1401802

Jara, A. D., Betemariam, A., Woldetinsae, G., & Kim, J. Y. (2019). Purification, application and current market trend of natural graphite: A review. *International Journal of Mining Science and Technology*, *29*(5), 671-689. https://doi.org/10.1016/j.ijmst.2019.04.003

Jin, Y., Xia, N., & Gerhardt, R. A. (2016). Enhanced dielectric properties of polymer matrix composites with BaTiO3 and MWCNT hybrid fillers using simple phase separation. *Nano Energy*, *30*, 407-416. https://doi.org/10.1016/j.nanoen.2016.10.033

Kamar, N. T., Hossain, M. M., Khomenko, A., Haq, M., Drzal, L. T., & Loos, A. (2015). Interlaminar reinforcement of glass fiber/epoxy composites with graphene nanoplatelets. *Composites Part A: Applied Science and Manufacturing*, *70*, 82-92. https://doi.org/10.1016/j.compositesa.2014.12.010

Kastner, J., Plank, B., Salaberger, D., & Sekelja, J. (2010). Defect and Porosity Determination of Fibre Reinforced Polymers by X-ray Computed Tomography, 12.

Kim, H., Abdala, A. A., & Macosko, C. W. (2010a). Graphene/Polymer Nanocomposites. *Macromolecules*, *43*(16), 6515-6530. https://doi.org/10.1021/ma100572e

Kim, H., Abdala, A. A., & Macosko, C. W. (2010b). Graphene/Polymer Nanocomposites. *Macromolecules*, *43*(16), 6515-6530. https://doi.org/10.1021/ma100572e

King, J. A., Klimek, D. R., Miskioglu, I., & Odegard, G. M. (2013). Mechanical properties of graphene nanoplatelet/epoxy composites. *Journal of Applied Polymer Science*, *128*(6), 4217-4223. https://doi.org/10.1002/app.38645

Kite, A. H., Hsu, D. K., Barnard, D. J., Thompson, D. O., & Chimenti, D. E. (2008). Determination of porosity content in composites by micrograph image processing. Dans *AIP Conference Proceedings* (Vol. 975, pp. 942-949). Golden (Colorado) : AIP. https://doi.org/10.1063/1.2902767

Knieke, C., Berger, A., Voigt, M., Taylor, R. N. K., Röhrl, J., & Peukert, W. (2010). Scalable production of graphene sheets by mechanical delamination. *Carbon*, *48*(11), 3196-3204. https://doi.org/10.1016/j.carbon.2010.05.003

Kosynkin, D. V., Higginbotham, A. L., Sinitskii, A., Lomeda, J. R., Dimiev, A., Price, B. K., & Tour, J. M. (2009). Longitudinal unzipping of carbon nanotubes to form graphene nanoribbons. *Nature*, *458*(7240), 872-876. https://doi.org/10.1038/nature07872

Krane, N. (2011). Preparation of graphene. Selected Topics in Physics: Physics of Nanoscale Carbon, 5. Repéré à https://pdfs.semanticscholar.org/f6cf/89b0574f133423b7bfbda1e8a907fa46f6dd.pdf

Lee, C., Wei, X., Kysar, J. W., & Hone, J. (2008). Measurement of the Elastic Properties and Intrinsic Strength of Monolayer Graphene. *Science*, *321*(5887), 385-388. https://doi.org/10.1126/science.1157996

Lentzakis, H., Moghimian, N., Saeidlou, S., Song, N., Kaydanova, T., Poulin, J., & David, É. (2017). Mechanical, Thermal and Electrical Property Enhancement of Graphene-Polymer Nanocomposites, 5.

Li, C., Thostenson, E. T., & Chou, T.-W. (2007). Dominant role of tunneling resistance in the electrical conductivity of carbon nanotube–based composites. *Applied Physics Letters*, *91*(22), 223114. https://doi.org/10.1063/1.2819690

Li, N., Wang, Z., Zhao, K., Shi, Z., Gu, Z., & Xu, S. (2010). Large scale synthesis of N-doped multi-layered graphene sheets by simple arc-discharge method. *Carbon*, *48*(1), 255-259. https://doi.org/10.1016/j.carbon.2009.09.013

Li, X., Cai, W., An, J., Kim, S., Nah, J., Yang, D. Ruoff, R. S. (2009). Large-Area Synthesis of High-Quality and Uniform Graphene Films on Copper Foils. *Science*, *324*(5932), 1312-1314. https://doi.org/10.1126/science.1171245

Liu, L., Shen, Z., Yi, M., Zhang, X., & Ma, S. (2014). A green, rapid and size-controlled production of high-quality graphene sheets by hydrodynamic forces. *RSC Adv.*, *4*(69), 36464-36470. https://doi.org/10.1039/C4RA05635C

Liu, N., Luo, F., Wu, H., Liu, Y., Zhang, C., & Chen, J. (2008). One-Step Ionic-Liquid-Assisted Electrochemical Synthesis of Ionic-Liquid-Functionalized Graphene Sheets Directly from Graphite: Ionic-Liquid-Assisted Electrochemical Synthesis of Graphene. *Advanced Functional Materials*, *18*(10), 1518-1525. https://doi.org/10.1002/adfm.200700797

Liu, X., & Chen, F. (2016). A Review of Void Formation and its Effects on the Mechanical Performance of Carbon Fiber Reinforced Plastic, 19.

Lohar, D. V. (2017). Literature Review of Graphene Composites. *M. S*, *6*(1), 4.

94

Lomeda, J. R., Doyle, C. D., Kosynkin, D. V., Hwang, W.-F., & Tour, J. M. (2008). Diazonium Functionalization of Surfactant-Wrapped Chemically Converted Graphene Sheets. *Journal of the American Chemical Society*, *130*(48), 16201-16206. https://doi.org/10.1021/ja806499w

Lotya, M., King, P. J., Khan, U., De, S., & Coleman, J. N. (2010). High-Concentration, Surfactant-Stabilized Graphene Dispersions. *ACS Nano*, *4*(6), 3155-3162. https://doi.org/10.1021/nn1005304

Lux, F. (1993). Models proposed to explain the electrical conductivity of mixtures made of conductive and insulating materials. *Journal of Materials Science*, *28*(2), 285-301. https://doi.org/10.1007/BF00357799

Mattevi, C., Kim, H., & Chhowalla, M. (2011). A review of chemical vapour deposition of graphene on copper. *J. Mater. Chem.*, *21*(10), 3324-3334. https://doi.org/10.1039/C0JM02126A

Mayr, G., Plank, B., Sekelja, J., & Hendorfer, G. (2011). Active thermography as a quantitative method for non-destructive evaluation of porous carbon fiber reinforced polymers. *NDT & E International*, *44*(7), 537-543. https://doi.org/10.1016/j.ndteint.2011.05.012

McAllister, M. J., Li, J.-L., Adamson, D. H., Schniepp, H. C., Abdala, A. A., Liu, J., Aksay, I. A. (2007). Single Sheet Functionalized Graphene by Oxidation and Thermal Expansion of Graphite. *Chemistry of Materials*, *19*(18), 4396-4404. https://doi.org/10.1021/cm0630800

Mclaughlin, A. M. (2013). *The effect of exfpmoated graphite on carbon fiber reinforced composites for cryogenic applications*. University of Massachusetts Lowell, 789 East Eisenhower Parkway P.O. Box 1346 Ann Arbor, Ml 48106-1346.

Mebarki, F. (2017). *ÉCOLE DE TECHNOLOGIE SUPÉRIEURE UNIVERSITÉ DU QUÉBEC*. UNIVERSITÉ DU QUÉBEC, ÉCOLE DE TECHNOLOGIE SUPÉRIEURE. Repéré à https://espace.etsmtl.ca/id/eprint/1955/

Mehdikhani, M., Gorbatikh, L., Verpoest, I., & Lomov, S. V. (2019). Voids in fiber-reinforced polymer composites: A review on their formation, characteristics, and effects on mechanical performance. *Journal of Composite Materials*, *53*(12), 1579-1669. https://doi.org/10.1177/0021998318772152

Monti, M., Rallini, M., Puglia, D., Peponi, L., Torre, L., & Kenny, J. M. (2013). Morphology and electrical properties of graphene–epoxy nanocomposites obtained by different solvent assisted processing methods. *Composites Part A: Applied Science and Manufacturing*, *46*, 166-172. https://doi.org/10.1016/j.compositesa.2012.11.005

National Research Council (U.S.) (Éd.). (1995). *Prudent practices in the laboratory: handling and disposal of chemicals*. Washington, D.C : National Academy Press.

Nazarpour, S., & Waite, S. R. (Éds). (2016). *Graphene technology: from laboratory to fabrication*. Weinheim : Wiley-VCH Verlag GmbH & Co. KGaA. Repéré à https://books.google.ca/books?hl=fr&lr=&id=wGmEDAAAQBAJ&oi=fnd&pg=PP2&dq=Nazarpour,+S.+and+Walte.+R.S.,+2016,+Graphene+Technology+from+Laboratory+to+Fabrication.+WileyVCH,&ots=d8scZVjEGG&sig=BGxdtfgF6l3TO0di2SNad6oPbUE#v=onepage&q&f=true

Nethravathi, C., & Rajamathi, M. (2008). Chemically modified graphene sheets produced by the solvothermal reduction of colloidal dispersions of graphite oxide. *Carbon*, *46*(14), 1994-1998. https://doi.org/10.1016/j.carbon.2008.08.013

Novoselov, K. S. (2004). Electric Field Effect in Atomically Thin Carbon Films. *Science*, *306*(5696), 666-669. https://doi.org/10.1126/science.1102896

Novoselov, K. S., & Castro Neto, A. H. (2012). Two-dimensional crystals-based heterostructures: materials with tailored properties. *Physica Scripta*, *T146*, 014006. https://doi.org/10.1088/0031-8949/2012/T146/014006

Oskouyi, A., Sundararaj, U., & Mertiny, P. (2014). Tunneling Conductivity and Piezoresistivity of Composites Containing Randomly Dispersed Conductive Nano-Platelets. *Materials*, *7*(4), 2501-2521. https://doi.org/10.3390/ma7042501

Othman, R., Ismail, N. I., Basri, H. M., Sharudin, H., & Hemdi, A. R. (2018). Application of carbon fiber reinforced plastics in automotive industry: a review, *1*, 12.

Panteny, S., Stevens, R., & Bowen, C. R. (2005). The Frequency Dependent Permittivity and AC Conductivity of Random Electrical Networks. *Ferroelectrics*, *319*(1), 199-208. https://doi.org/10.1080/00150190590965884

Pathak, A. K., Borah, M., Gupta, A., Yokozeki, T., & Dhakate, S. R. (2016). Improved mechanical properties of carbon fiber/graphene oxide-epoxy hybrid composites. *Composites Science and Technology*, *135*, 28-38. https://doi.org/10.1016/j.compscitech.2016.09.007

Paul, D. R., & Robeson, L. M. (2008). Polymer nanotechnology: Nanocomposites. *Polymer*, *49*(15), 3187-3204. https://doi.org/10.1016/j.polymer.2008.04.017

Pierson, H. O. (1993). Graphite Structure and Properties. Dans *Handbook of Carbon, Graphite, Diamonds and Fullerenes* (pp. 43-69). (S.l.) : Elsevier. https://doi.org/10.1016/B978-0-8155-1339-1.50008-6

Prasai, D., Tuberquia, J. C., Harl, R. R., Jennings, G. K., & Bolotin, K. I. (2012). Graphene: Corrosion-Inhibiting Coating. *ACS Nano*, *6*(2), 1102-1108. https://doi.org/10.1021/nn 203507y

Psarras, G. C. (2018). Fundamentals of Dielectric Theories. Dans *Dielectric Polymer Materials for High-Density Energy Storage* (pp. 11-57). (S.l.) : Elsevier. https://doi.org/10.1016/ B978-0-12-813215-9.00002-6

Qin, W., Vautard, F., Drzal, L. T., & Yu, J. (2015). Mechanical and electrical properties of carbon fiber composites with incorporation of graphene nanoplatelets at the fiber–matrix interphase. *Composites Part B: Engineering*, *69*, 335-341. https://doi.org/10.10 16/j.compositesb.2014.10.014

Radivojevic, Z., Beecher, P., Bower, C., Haque, S., Andrew, P., Hasan, T., Henson, B. (2012). Electrotactile touch surface by using transparent graphene. Dans *Proceedings of the 2012 Virtual Reality International Conference on - VRIC '12* (p. 1). Laval, France : ACM Press. https://doi.org/10.1145/2331714.2331733

Rafiee, M. A., Rafiee, J., Wang, Z., Song, H., Yu, Z.-Z., & Koratkar, N. (2009). Enhanced Mechanical Properties of Nanocomposites at Low Graphene Content. *ACS Nano*, *3*(12), 3884-3890. https://doi.org/10.1021/nn9010472

Randviir, E. P., Brownson, D. A. C., & Banks, C. E. (2014). A decade of graphene research: production, applications and outlook. *Materials Today*, *17*(9), 426-432. https://doi.org /10.1016/j.mattod.2014.06.001

Raza, M. A., Westwood, A. V. K., & Stirling, C. (2012). Effect of processing technique on the transport and mechanical properties of graphite nanoplatelet/rubbery epoxy composites for thermal interface applications. *Materials Chemistry and Physics*, *132*(1), 63-73. https://doi.org/10.1016/j.matchemphys.2011.10.052

Roldughin, V. I., & Vysotskii, V. V. (2000). Percolation properties of metal-filled polymer films, structure and mechanisms of conductivity. *Progress in Organic Coatings*, *39*(2-4), 81-100. https://doi.org/10.1016/S0300-9440(00)00140-5

Sandler, J. K. W., Pegel, S., Cadek, M., Gojny, F., van Es, M., Lohmar, J., Shaffer, M. S. P. (2004). A comparative study of melt spun polyamide-12 fibres reinforced with carbon nanotubes and nanofibres. *Polymer*, *45*(6), 2001-2015. https://doi.org/10.1016/j.polym er.2004.01.023

Schniepp, H. C., Li, J.-L., McAllister, M. J., Sai, H., Herrera-Alonso, M., Adamson, D. H., Aksay, I. A. (2006). Functionalized Single Graphene Sheets Derived from Splitting Graphite Oxide. *The Journal of Physical Chemistry B*, *110*(17), 8535-8539. https://doi.org/10.1021/jp060936f

Sengupta, R., Bhattacharya, M., Bandyopadhyay, S., & Bhowmick, A. K. (2011). A review on the mechanical and electrical properties of graphite and modified graphite reinforced polymer composites. *Progress in Polymer Science*, *36*(5), 638-670. https://doi.org/10.1016/j.progpolymsci.2010.11.003

Seol, J. H., Jo, I., Moore, A. L., Lindsay, L., Aitken, Z. H., Pettes, M. T., Shi, L. (2010). Two-Dimensional Phonon Transport in Supported Graphene. *Science*, *328*(5975), 213-216. https://doi.org/10.1126/science.1184014

Serenari, F. (2019). *Development of a new reinforced Polyester/Graphene nanocomposite showing tailored surface electrical conductivity and electrostatic charge dissipation ability*. ETS – ÉCOLE DE TECHNOLOGIE SUPÉRIEURE.

Shen, Z., Li, J., Yi, M., Zhang, X., & Ma, S. (2011). Preparation of graphene by jet cavitation. *Nanotechnology*, *22*(36), 365306. https://doi.org/10.1088/0957-4484/22/36/365306

Simmons, J. G. (1963). Generalized Formula for the Electric Tunnel Effect between Similar Electrodes Separated by a Thin Insulating Film. *Journal of Applied Physics*, *34*(6), 1793-1803. https://doi.org/10.1063/1.1702682

Spierings, Th. A. M., Bosman, F., Peters, M. C. R. B., & Plasschaert, A. J. M. (1988). The thermal diffusivity of two replica resins. *Dental Materials*, *4*(2), 51-54. https://doi.org/10.1016/S0109-5641(88)80089-7

Stankovich, S., Dikin, D. A., Dommett, G. H. B., Kohlhaas, K. M., Zimney, E. J., Stach, E. A., Ruoff, R. S. (2006a). Graphene-based composite materials. *Nature*, *442*(7100), 282-286. https://doi.org/10.1038/nature04969

Stankovich, S., Dikin, D. A., Dommett, G. H. B., Kohlhaas, K. M., Zimney, E. J., Stach, E. A., Ruoff, R. S. (2006b). Graphene-based composite materials. *Nature*, *442*(7100), 282-286. https://doi.org/10.1038/nature04969

Stankovich, S., Dikin, D. A., Piner, R. D., Kohlhaas, K. A., Kleinhammes, A., Jia, Y.,Ruoff, R. S. (2007). Synthesis of graphene-based nanosheets via chemical reduction of exfoliated graphite oxide. *Carbon*, *45*(7), 1558-1565. https://doi.org/10.1016/j.carbon.2007.02.034

Stankovich, S., Piner, R. D., Chen, X., Wu, N., Nguyen, S. T., & Ruoff, R. S. (2006). Stable aqueous dispersions of graphitic nanoplatelets via the reduction of exfoliated graphite oxide in the presence of poly(sodium 4-styrenesulfonate). *J. Mater. Chem.*, *16*(2), 155-158. https://doi.org/10.1039/B512799H

Stoller, M. D., Park, S., Zhu, Y., An, J., & Ruoff, R. S. (2008). Graphene-Based Ultracapacitors. *Nano Letters*, *8*(10), 3498-3502. https://doi.org/10.1021/nl802558y

Su, C.-Y., Lu, A.-Y., Xu, Y., Chen, F.-R., Khlobystov, A. N., & Li, L.-J. (2011). High-Quality Thin Graphene Films from Fast Electrochemical Exfoliation. *ACS Nano*, *5*(3), 2332-2339. https://doi.org/10.1021/nn200025p

Sutter, P. W., Flege, J.-I., & Sutter, E. A. (2008). Epitaxial graphene on ruthenium. *Nature Materials*, *7*(5), 406-411. https://doi.org/10.1038/nmat2166

Takezawa, Y., Akatsuka, M., & Farren, C. (2003). High thermal conductive epoxy resins with controlled high order structure. Dans *Proceedings of the 7th International Conference on Properties and Applications of Dielectric Materials (Cat. No.03CH37417)* (Vol. 3, pp. 1146-1149). Nagoya, Japan : IEEE. https://doi.org/10.1109/ICPADM.2003.1218626

Tang, B., Hu, G., Gao, H., & Hai, L. (2015). Application of graphene as filler to improve thermal transport property of epoxy resin for thermal interface materials. *International Journal of Heat and Mass Transfer*, *85*, 420-429. https://doi.org/10.1016/j.ijheatmasstransfer.2015.01.141

Tang, L.-C., Wan, Y.-J., Yan, D., Pei, Y.-B., Zhao, L., Li, Y.-B., Lai, G.-Q. (2013). The effect of graphene dispersion on the mechanical properties of graphene/epoxy composites. *Carbon*, *60*, 16-27. https://doi.org/10.1016/j.carbon.2013.03.050

Technomic Publishing Company (Éd.). (1999). *The composite materials handbook: MIL 17. Vol. 3: Materials, usage, design, and analysis*. Lancaster : Technomic Publ.

Teng, C.-C., Ma, C.-C. M., Lu, C.-H., Yang, S.-Y., Lee, S.-H., Hsiao, M.-C., Lee, T.-M. (2011). Thermal conductivity and structure of non-covalent functionalized graphene/epoxy composites. *Carbon*, *49*(15), 5107-5116. https://doi.org/10.1016/j.carbon.2011.06.095

Teti, R. (2002). Machining of Composite Materials. *CIRP Annals*, *51*(2), 611-634. https://doi.org/10.1016/S0007-8506(07)61703-X

Thostenson, E. T., & Chou, T.-W. (2006). Processing-structure-multi-functional property relationship in carbon nanotube/epoxy composites. *Carbon*, *44*(14), 3022-3029. https://doi.org/10.1016/j.carbon.2006.05.014

Utomo, A., Baker, M., & Pacek, A. W. (2009). The effect of stator geometry on the flow pattern and energy dissipation rate in a rotor–stator mixer. *Chemical Engineering Research and Design*, *87*(4), 533-542. https://doi.org/10.1016/j.cherd.2008.12.011

Vasilyeva, M. A., Lounev, I. V., & Gusev, Yu. A. (2013). The Methodology of the Experiment on the Dielectric Spectrometer Novocontrol BDS Concept 80, 65. Repéré à https://docplayer.net/90488811-The-methodology-of-the-experiment-on-the-dielectric-spectrometer-novocontrol-bds-concept-80.html

Wajid, A. S., Ahmed, H. S. T., Das, S., Irin, F., Jankowski, A. F., & Green, M. J. (2013). High-Performance Pristine Graphene/Epoxy Composites With Enhanced Mechanical and Electrical Properties: High-Performance Pristine Graphene/Epoxy Composites With Enhanced Mechanical *Macromolecular Materials and Engineering*, *298*(3), 339-347. https://doi.org/10.1002/mame.201200043

Wang, F., Drzal, L. T., Qin, Y., & Huang, Z. (2015). Mechanical properties and thermal conductivity of graphene nanoplatelet/epoxy composites. *Journal of Materials Science*, *50*(3), 1082-1093. https://doi.org/10.1007/s10853-014-8665-6

Wang, Hailiang, Robinson, J. T., Li, X., & Dai, H. (2009). Solvothermal Reduction of Chemically Exfoliated Graphene Sheets. *Journal of the American Chemical Society*, *131*(29), 9910-9911. https://doi.org/10.1021/ja904251p

Wang, Hui, Sun, K., Tao, F., Stacchiola, D. J., & Hu, Y. H. (2013). 3D Honeycomb-Like Structured Graphene and Its High Efficiency as a Counter-Electrode Catalyst for Dye-Sensitized Solar Cells. *Angewandte Chemie International Edition*, *52*(35), 9210-9214. https://doi.org/10.1002/anie.201303497

Wang, X.-Y., Narita, A., & Müllen, K. (2018). Precision synthesis versus bulk-scale fabrication of graphenes. *Nature Reviews Chemistry*, *2*(1), 0100. https://doi.org/10.1038/s41570-017-0100

Weber, M., & Kamal, M. R. (1997). Estimation of the volume resistivity of electrically conductive composites. *Polymer Composites*, *18*(6), 711-725. https://doi.org/10.1002/pc.10324

Wu, C.-S. (1992). Influence of post-curing and temperature effects on bulk density, glass transition and stress-strain behaviour of imidazole-cured epoxy network. *Journal of Materials Science*, *27*(11), 2952-2959. https://doi.org/10.1007/BF01154105

Xiang, J., & Drzal, L. T. (2011). Thermal conductivity of exfoliated graphite nanoplatelet paper. *Carbon*, *49*(3), 773-778. https://doi.org/10.1016/j.carbon.2010.10.003

Yang, K., Huang, X., Huang, Y., Xie, L., & Jiang, P. (2013). Fluoro-Polymer@BaTiO$_3$ Hybrid Nanoparticles Prepared via RAFT Polymerization: Toward Ferroelectric Polymer Nanocomposites with High Dielectric Constant and Low Dielectric Loss for Energy Storage Application. *Chemistry of Materials*, *25*(11), 2327-2338. https://doi.org/10.1021/cm4010486

Yang, S.-Y., Ma, C.-C. M., Teng, C.-C., Huang, Y.-W., Liao, S.-H., Huang, Y.-L., Chiou, K.-C. (2010). Effect of functionalized carbon nanotubes on the thermal conductivity of epoxy composites. *Carbon*, *48*(3), 592-603. https://doi.org/10.1016/j.carbon.2009.08.047

Yang, W., Zhao, Q., Xin, L., Qiao, J., Zou, J., Shao, P., Wu, G. (2018). Microstructure and mechanical properties of graphene nanoplates reinforced pure Al matrix composites prepared by pressure infiltration method. *Journal of Alloys and Compounds*, *732*, 748-758. https://doi.org/10.1016/j.jallcom.2017.10.283

Yang, X., Dou, X., Rouhanipour, A., Zhi, L., Räder, H. J., & Müllen, K. (2008). Two-Dimensional Graphene Nanoribbons. *Journal of the American Chemical Society*, *130*(13), 4216-4217. https://doi.org/10.1021/ja710234t

Yasmin, A., & Daniel, I. M. (2004). Mechanical and thermal properties of graphite platelet/epoxy composites. *Polymer*, *45*(24), 8211-8219. https://doi.org/10.1016/j.polymer.2004.09.054

Yi, M., & Shen, Z. (2015). A review on mechanical exfoliation for the scalable production of graphene. *Journal of Materials Chemistry A*, *3*(22), 11700-11715. https://doi.org/10.1039/C5TA00252D

Yu, Q., Lian, J., Siriponglert, S., Li, H., Chen, Y. P., & Pei, S.-S. (2008). Graphene segregated on Ni surfaces and transferred to insulators. *Applied Physics Letters*, *93*(11), 113103. https://doi.org/10.1063/1.2982585

Zhang, J. Z. (2013). Study on Carbon Fiber Composite Materials in Sports Equipment. *Applied Mechanics and Materials*, *329*, 105-108. https://doi.org/10.4028/www.scientific.net/AMM.329.105

Zhang, W., Cui, J., Tao, C., Wu, Y., Li, Z., Ma, L., Li, G. (2009). A Strategy for Producing Pure Single-Layer Graphene Sheets Based on a Confined Self-Assembly Approach. *Angewandte Chemie International Edition*, *48*(32), 5864-5868. https://doi.org/10.1002/anie.200902365

Zhang, Y., Zhang, L., & Zhou, C. (2013). Review of Chemical Vapor Deposition of Graphene and Related Applications. *Accounts of Chemical Research*, *46*(10), 2329-2339. https://doi.org/10.1021/ar300203n

Zhao, X., Hayner, C. M., Kung, M. C., & Kung, H. H. (2011). In-Plane Vacancy-Enabled High-Power Si-Graphene Composite Electrode for Lithium-Ion Batteries. *Advanced Energy Materials*, *1*(6), 1079-1084. https://doi.org/10.1002/aenm.201100426

Zhou, Yong, Bao, Q., Tang, L. A. L., Zhong, Y., & Loh, K. P. (2009). Hydrothermal Dehydration for the "Green" Reduction of Exfoliated Graphene Oxide to Graphene and Demonstration of Tunable Optical Limiting Properties. *Chemistry of Materials*, *21*(13), 2950-2956. https://doi.org/10.1021/cm9006603

Zhou, Yongcun, Liu, F., & Wang, H. (2017). Novel organic-inorganic composites with high thermal conductivity for electronic packaging applications: A key issue review. *Polymer Composites*, *38*(4), 803-813. https://doi.org/10.1002/pc.23641

Zou, W. (2016). *A study on mechanical, electrical, and thermal properties of graphene nanoplatelets reinforced epoxy composites*. University of Manchester. Repéré à https://search.proquest.com/pqdtglobal/docview/2154400754/3210587735D941A9PQ/6?accountid=27231

Zuo, X., Chang, K., Zhao, J., Xie, Z., Tang, H., Li, B., & Chang, Z. (2016). Bubble-template-assisted synthesis of hollow fullerene-like MoS$_2$ nanocages as a lithium ion battery anode material. *Journal of Materials Chemistry A*, *4*(1), 51-58. https://doi.org/10.1039/C5TA06869J